THE OHIO STATE UNIVERSITY

A STUDY OF THE TCAS II COLLISION AVOIDANCE SYSTEM MOUNTED ON A BOEING 737 AIRCRAFT

B. Grandchamp
W.D. Burnside
R.G. Rojas

The Ohio State University
ElectroScience Laboratory
Department of Electrical Engineering
Columbus, Ohio 43212

Technical Report 716199-10
Grant NSG 1498
December 1987

National Aeronautics and Space Administration
Langley Research Center
Hampton, Virginia 23665

NOTICES

When Government drawings, specifications, or other data are used for any purpose other than in connection with a definitely related Government procurement operation, the United States Government thereby incurs no responsibility nor any obligation whatsoever, and the fact that the Government may have formulated, furnished, or in any way supplied the said drawings, specifications, or other data, is not to be regarded by implication or otherwise as in any manner licensing the holder or any other person or corporation, or conveying any rights or permission to manufacture, use, or sell any patented invention that may in any way be related thereto.

50272-101

REPORT DOCUMENTATION PAGE	1. REPORT NO.	2.	3. Recipient's Accession No.

4. Title and Subtitle

A Study of the TCAS II Collision Avoidance System Mounted on a Boeing 737 Aircraft

5. Report Date December 1987

6.

7. Author(s)

B. Grandchamp, W.D. Burnside, R.G. Rojas

8. Performing Organization Rept. No. 716199-10

9. Performing Organization Name and Address

The Ohio State University ElectroScience Laboratory
1320 Kinnear Road
Columbus, Ohio 43212

10. Project/Task/Work Unit No.

11. Contract(C) or Grant(G) No.

(C)

(G) NSG 1498

12. Sponsoring Organization Name and Address

National Aeronautics and Space Administration
Langley Research Center
Hampton, Virginia 23665

13. Type of Report & Period Covered Technical

14.

15. Supplementary Notes

16. Abstract (Limit: 200 words)

The purpose of this report is to determine the effects of scattering from major aircraft structures on the TCAS II collision avoidance system mounted on a Boeing 737.

It is found that the major source of scattering for angles of observation above the horizon is the vertical stabilizer and that its effect may be greatly reduced by mounting the TCAS II array close to the nose of the aircraft. In addition, by mounting the array close to the nose, the effects of fuselage blockage on the array patterns at elevation angles below the horizon may be greatly reduced in the forward direction.

17. Document Analysis a. Descriptors

b. Identifiers/Open-Ended Terms

c. COSATI Field/Group

18. Availability Statement	19. Security Class (This Report) Unclassified	21. No. of Pages 175
	20. Security Class (This Page) Unclassified	22. Price

(See ANSI-Z39.18) See Instructions on Reverse

OPTIONAL FORM 272 (4-77)
(Formerly NTIS-35)
Department of Commerce

TABLE OF CONTENTS

LIST OF TABLES

LIST OF FIGURES

I. INTRODUCTION

The TCAS II is an airborne collision avoidance system which combines information about the elevation, slant range and azimuth bearing of nearby aircraft in order to alert the pilot to impending mid-air collisions.

The operation of the TCAS II relies on the field patterns of its circular antenna array, which is mounted on top of the aircraft fuselage, to determine the azimuth bearing of nearby aircraft. Because of this, the system is susceptible to influence by the effects of scattering from the aircraft on which the system is installed.

The projected system performance was based on measurements done with the array mounted on a circular curved ground plane. This not only neglected scattering from the major aircraft structures, such as wings and tail but also added unwanted effects from the junction of the curved ground plane and the ground.

The problem, then, was to use the Ohio State University Aircraft Code to simulate the TCAS II mounted on a Boeing 737 aircraft and determine the effects of scattering on the field patterns of the circular array.

It has been determined that reflection and diffraction from the wings causes distorting ripple in the array patterns in the region $\pm 120°$ from the nose of the Boeing 737 and that reflection in this case is the major source of the ripple.

The most severely affected region in the array patterns is in the direction of the tail. The large distortions in the patterns here are caused by scattering from the vertical stabilzer with diffraction being by far the dominant mechanism. This scattering effect is strongly dependent on the elevation angle of the pattern cut in that once the elevation angle has cleared the top of the vertical stabilizer its effect on the field pattern is greatly reduced.

Finally it is shown that the negative effects of the major source of scattering, the vertical stabilizer, may be reduced by mounting the circular array as far away from it as possible and that this will also reduce the effects of fuselage blockage in the forward direction for elevation angles below the horizon.

II. AIRCRAFT CODE SIMULATION

The Ohio State University aircraft code is a Fortran 77 program based on the Uniform Theory of Diffraction (UTD) [1] that is capable of calculating both near and far field patterns of fuselage mounted aircraft antenna. The fuselage of the aircraft is modeled by a composite ellipsoid while the wings, vertical stabilizer and other scattering structures are modeled by flat plates.

UTD is a high frequency technique which can be used to calculate aircraft antenna patterns provided that the source and scatterers are separated by a distance of at least one wavelength and that the smallest dimensions of all scatterers and the fuselage are at least one wavelength in extent. Good engineering results will still be obtained if this restriction is relaxed to one quarter wavelength [1].

The composite ellipsoid semi-major and semi-minor axes are defined by AX, BX, CX and DX as shown in Figure 1. It is constructed from two ellipsoid sections positioned back to back and connected together such that its surface is continuous and smooth at the cross section of the source location [2].

The case in which the source is positioned to the right of the coordinate system origin is shown in Figure 2a. The right side ellipsoid semi-major and semi-minor axes, a_f, b_f and c_f are given by [2]

$$a_f = AX$$

$$b_f = BX$$

$$c_f = CX$$

The parameters for the left side ellipsoid, a_f', b_f' and c_f' are then given as follows [2]:

$$a_f' = \frac{AX \cos V_{es}}{\cos V_{es}'}$$

$$b_f' = \frac{BX \cos V_{es}}{\cos V_{es}'}$$

and

$$c_f' = DX + Z_{sh}$$

where

$$V_{es} = \sin^{-1} \frac{Z_s}{CX}$$

$$V_{es}' = \sin^{-1} \left[\left[\frac{- CX \cos V_{es}}{\tan V_{es}(DX+Z_s)} + 1 \right]^{-1} \right]$$

and

$$Z_{sh} = \frac{Z_s - DX \sin V_{es}'}{1 + \sin V_{es}'} \quad .$$

Note that Z_s is the position of the source along the z axis and Z_{sh} is the distance between the right and left ellipsoid coordinate origins.

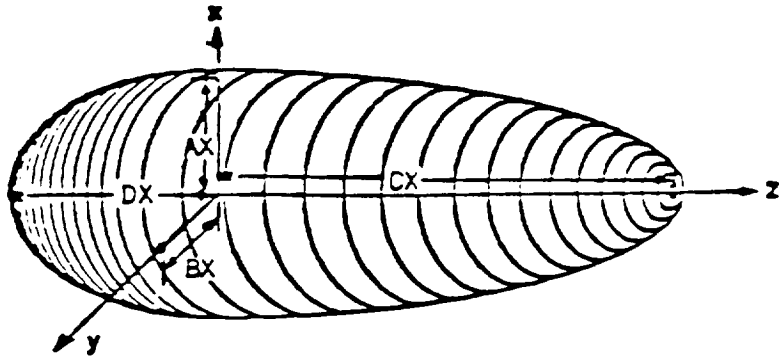

Figure 1. Definition of composite ellipsoid axes.

The case in which the source is located to the left of the coordinate system origin is shown in Figure 2b. The left side ellipsoid semi-major and semi-minor axes are given by [2]

$$a_f' = AX$$

$$b_f' = BX$$

$$c_f' = CX$$

The parameters for the right side ellipsoid are then given as follows [2]:

$$a_f = \frac{AX \cos V_{es}}{\cos V'_{es}}$$

$$b_f = \frac{BX \cos V_{es}}{\cos V'_{es}}$$

and

$$c_f = CX + Z_{sh}$$

where

$$V_{es} = \sin^{-1} \frac{Z_s}{DX}$$

$$V'_{es} = \sin^{-1} \left[\left[\frac{DX \cos V_{es}}{\tan V_{es}(CX+Z_s)} - 1 \right]^{-1} \right]$$

and

$$Z_{sh} = \frac{Z_s - CX \sin V'_{es}}{1 - \sin V'_{es}} \quad .$$

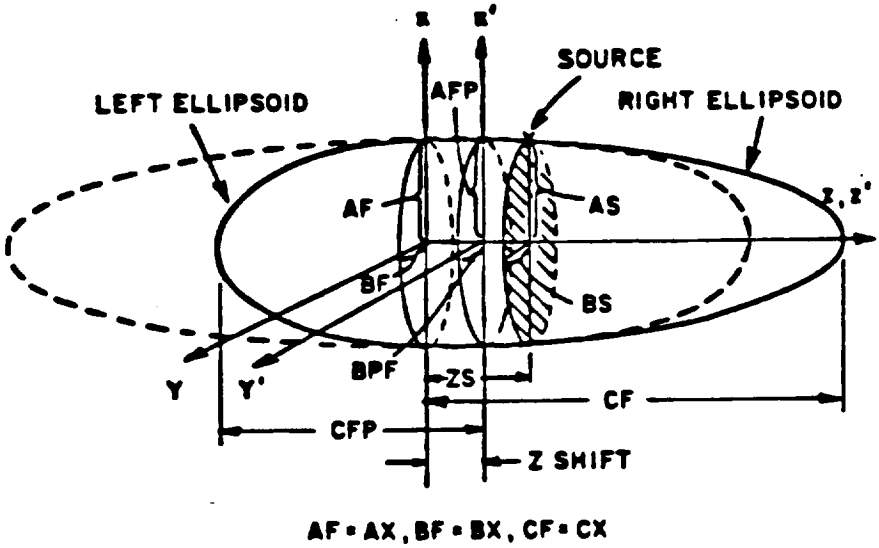

(a) when $Z_S > 0$

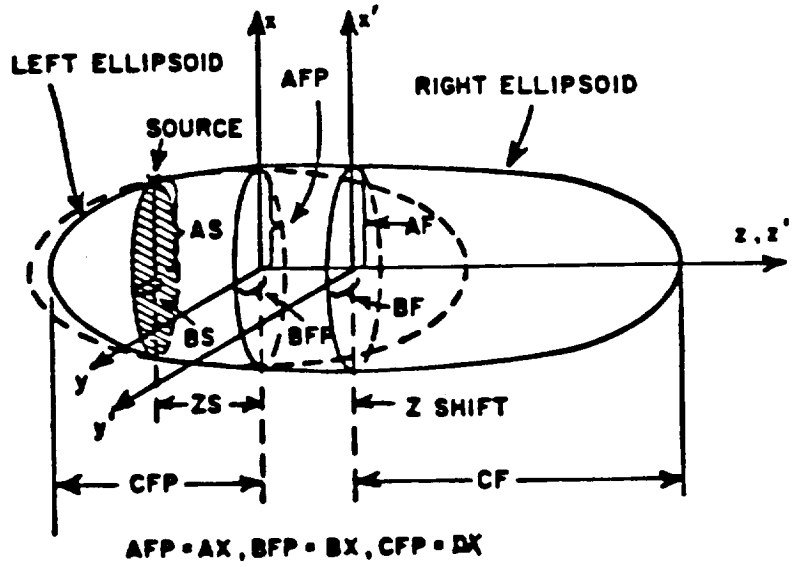

(b) when $Z_S < 0$

Figure 2. Composite ellipsoid geometry simulating the aircraft fuselage.

Up to 25 flat plates may be included in the computer model of the aircraft to simulate wings, stabilizers and other structures. The plates are defined by the positions of their corners and each plate may have up to six corners. Any plate may be defined as being attached to the fuselage. In this case the first and the last corner defined determine the edge of the plate which will be attached. The first and last corners need not exactly attach to the fuselage because the code will extend the edges of the plate and reset the first and final corner points on the fuselage as shown in Figure 3. Plates may be attached to each other in two ways. In the first case the two plates to be attached are defined with a common edge. In other words the plates have two identical corners. The code will recognize this and treat the plates accordingly. In the second case one plate is defined so that it extends a small amount through the plate to which it will be attached as shown in Figure 4. The edges of the intersecting plates should be separated by a distance of at least one quarter wavelength from the junction edge.

When two or more plates are attached to each other in order to model a closed structure it is possible that only one side of a plate is illuminated by the antenna. In this case the plate input data is formatted in such a way that the code can infer which side of the plate is illuminated. This is done by defining the plate corners according to the right hand rule. As the fingers of one's right hand are curled to follow the edges of the plate in the order of their definition, the thumb should point to the illuminated region above the plate as illustrated in Figure 5.

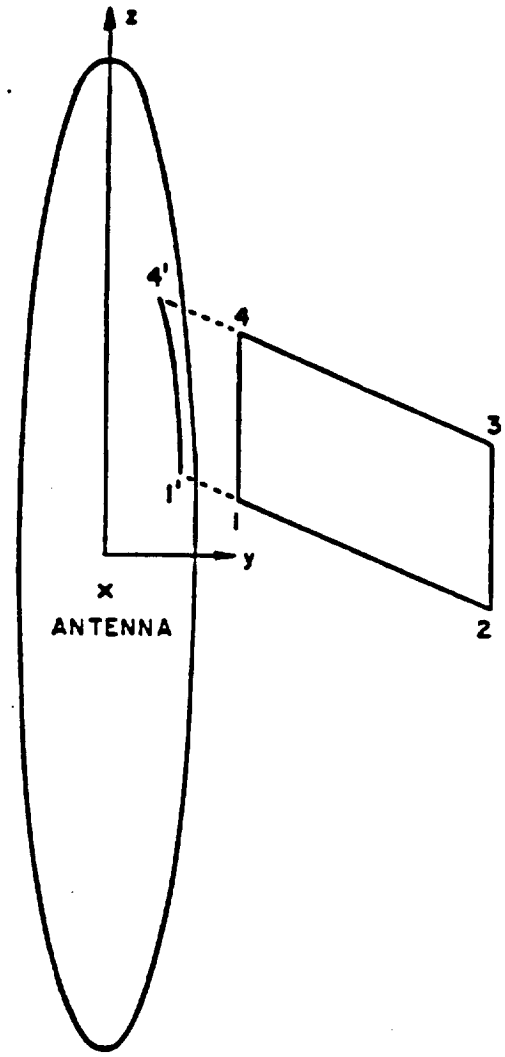

Figure 3. Data format used to define a flat plate attaching to a fuselage.

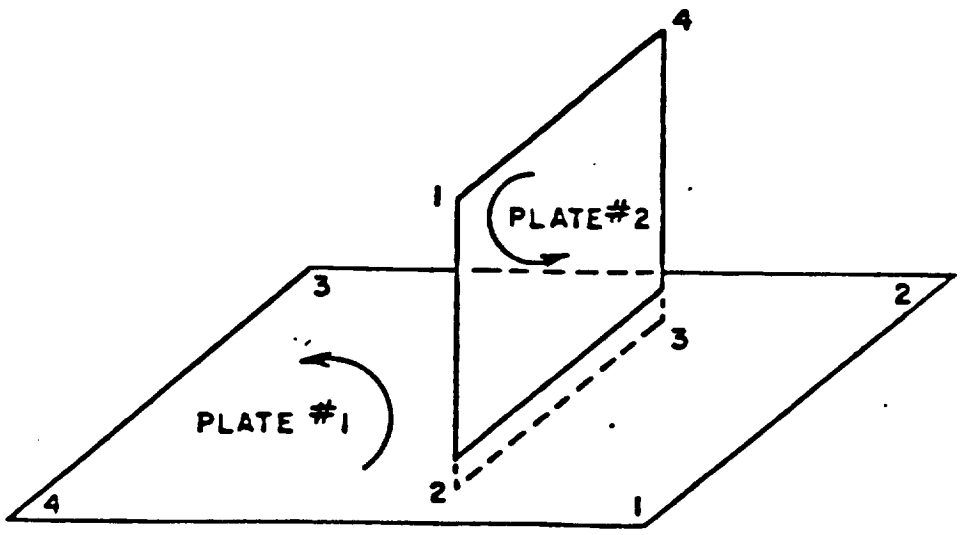

Figure 4. Data format used to define a flat plate intersecting another flat plate.

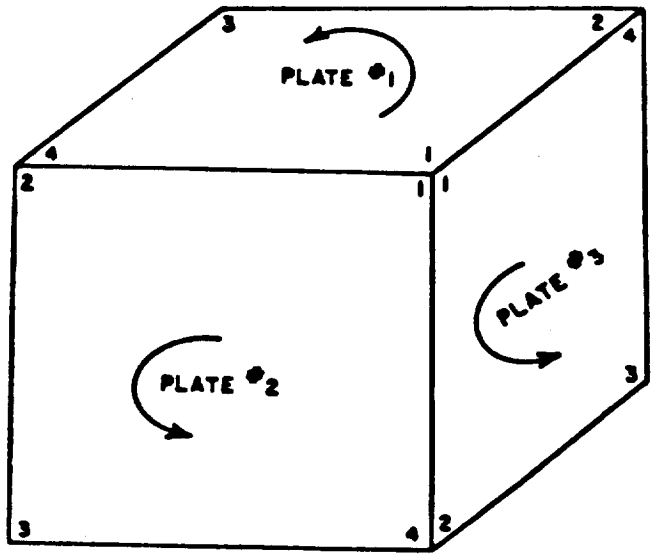

Figure 5. Data format used to define a closed structure.

Up to 10 antennas of the slot or monopole type may be modeled on the composite ellipsoid at one time. The slot antenna can be of any dimension but the monopole is limited to one quarter wavelength.

All antennas are defined in relation to a phase reference point. The location of the phase reference point is determined by its position along the axis of the aircraft Z_S and the angle ϕ_S which the phase reference point makes with the vertical as shown in Figure 6. The location of each antenna is then determined by the angle ϕ_A and the distance ρ_A from the phase reference point as shown in Figure 7. The code treats each antenna as though it is mounted on a plane tangential to the composite ellipsoid at the phase reference point.

The field computation normally includes the source, reflected and diffracted terms. It is also possible to include higher order reflected/reflected, reflected/diffracted, diffracted/reflected and diffracted/diffracted terms. The higher order terms are not usually needed; however, the code automatically shadows all terms such that if one or more are of them are necessary it will show as a discontinuity in the final antenna pattern.

The code has been designed so that these terms may be computed individually or in any combination. It is therefore possible to gain greater insight into which mechanisms, reflections, diffractions or higher order terms, are causing the largest disturbance in the antenna pattern.

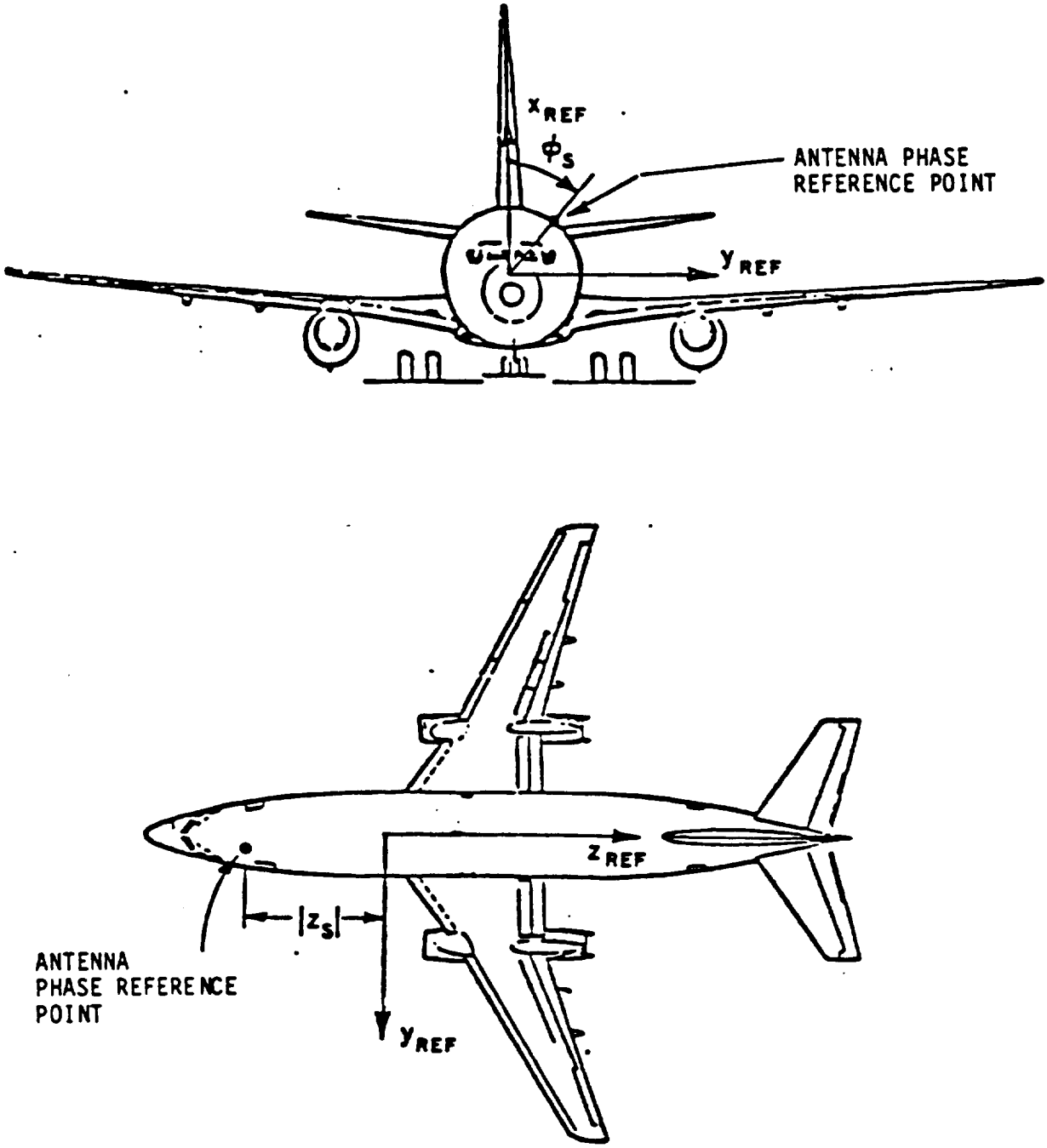

Figure 6. Definition of antenna phase reference point for computer code. Note that PHS = ϕ_S and ZS = $-|Z_S|$ in the above drawings.

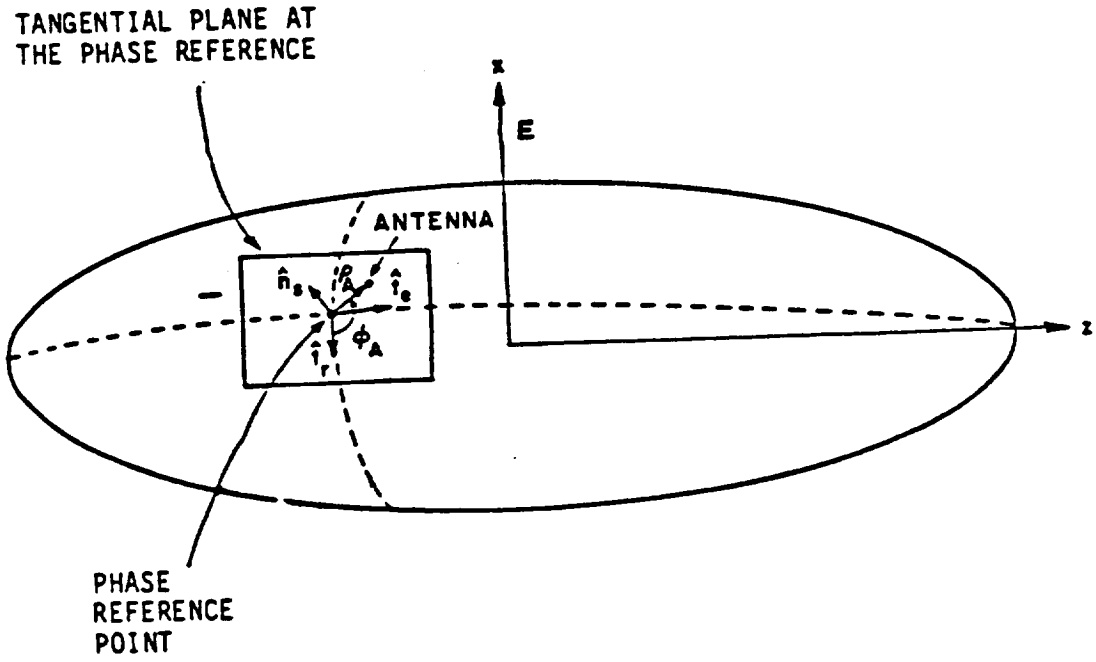

Figure 7. Source geometry.

The antenna pattern cut is determined by the range from the origin to the receiver, the axis about which the pattern is to be taken and the conical angle from the pattern axis. The pattern axis is determined by the spherical angles, THC and PHC, as shown in Figure 8. These angles actually set up a new coordinate system in relation to the reference coordinates. The new cartesian coordinates, defined by the subscript "p" are found by first rotating about the z axis the PHC angle and then about the y axis the THC angle. The pattern is then taken in the "p" coordinate system in terms of spherical angles. The conical angle of the pattern is defined by θ, and the phi angle, ϕ_p, is increased incrementally about the Z_p axis (pattern axis) as shown in Figure 8 [2].

The three primary pattern cuts involved when dealing with an aircraft are the roll, elevation and azimuth plane patterns. The definitions of these three pattern cuts are illustrated in Figure 9.

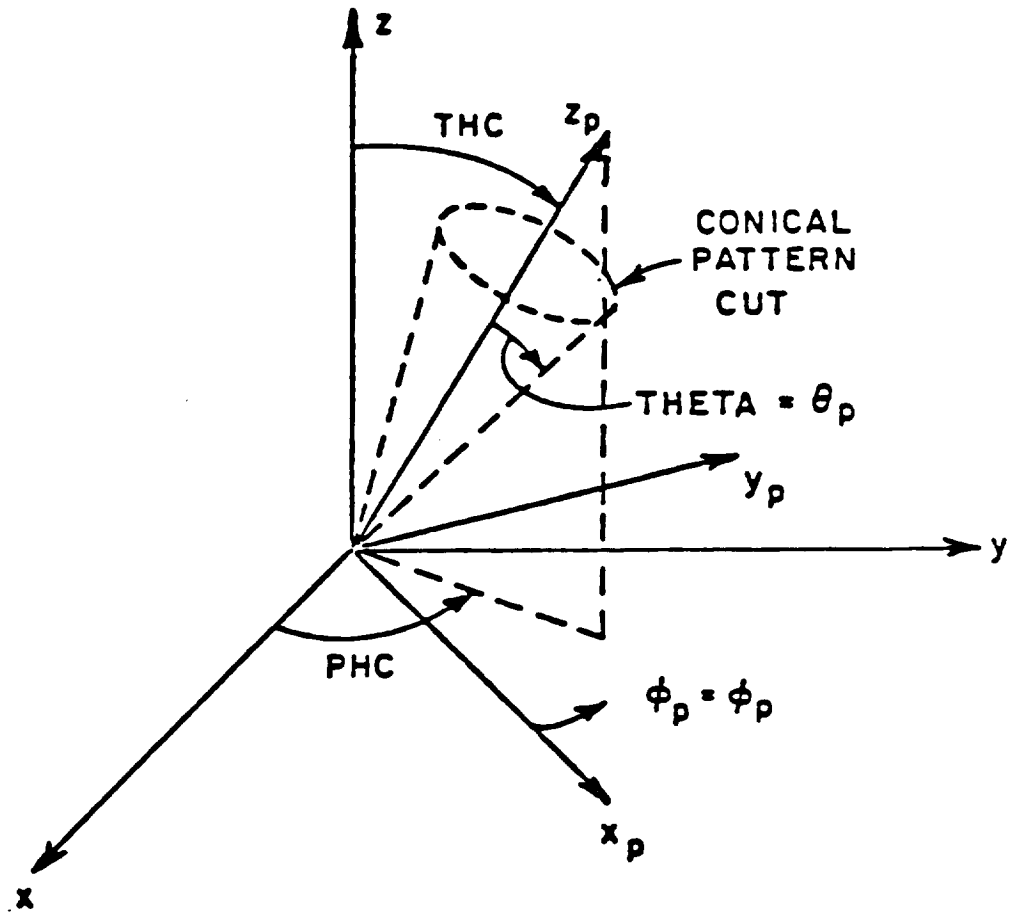

Figure 8. Definition of pattern axis.

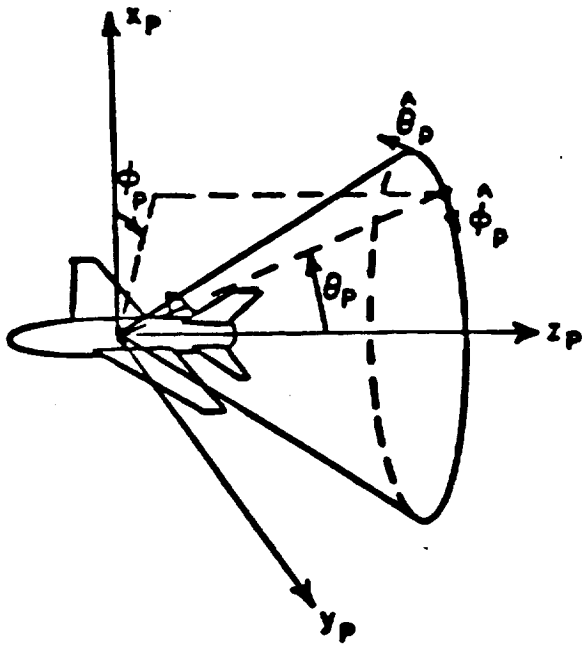

(a) Roll plane coordinates (THC = 0°, PHC = 0°)

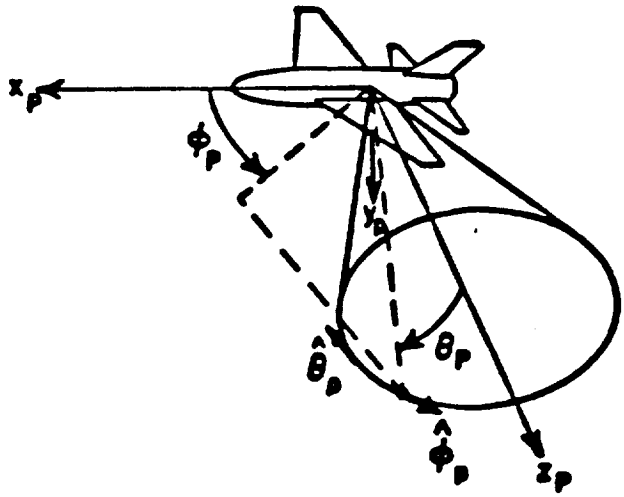

(b) Elevation plane coordinates (THC = 90°, PHC = 90°)

Figure 9. Principal aircraft antenna pattern cuts.

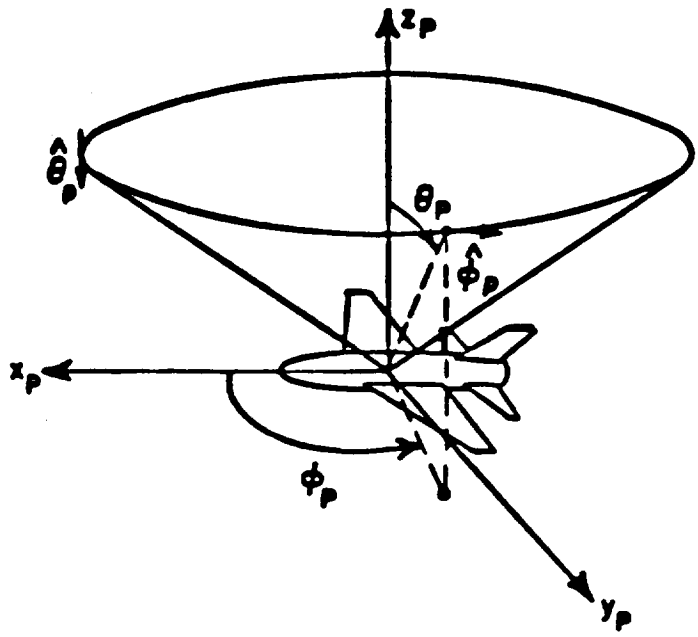

(c) Azimuth plane coordinates (THC = 90°, PHC = 0°)

Figure 9. (Continued).

III. TCAS II SYSTEM OPERATION

The TCAS II system has been designed to predict mid-air aircraft collisions based on the altitude, slant range and azimuth angle of nearby aircraft. We are interested in the determination of the azimuth angle because it is directly dependent on the antenna patterns of the system and is therefore subject to interference from scattering caused by aircraft structures.

The TCAS II system employs a 10.5 inch diameter circular array of eight top loaded monopoles. This array is mounted on top of the fuselage just over the leading edge of the wings. The array may be electronically scanned around 360 degrees in azimuth in 5.625° increments for a total of 64 separate beam positions and is designed to receive at 1090 MHz [3].

The circular array is driven by a Butler Matrix as shown in Figure 10.

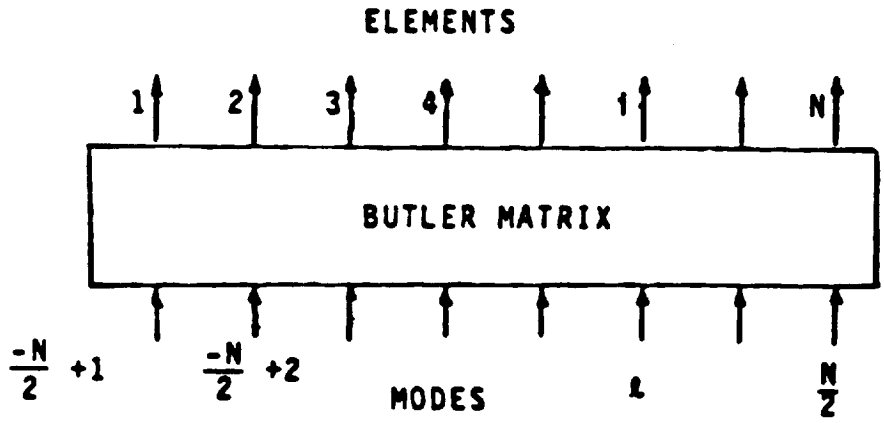

Figure 10. Butler matrix.

The Butler Matrix operates in such a manner that, given the mode inputs, the element excitations are given by [4]

$$E_i = \frac{1}{\sqrt{N}} \sum_{\ell=\frac{-N}{2}+1}^{\frac{N}{2}} MA_\ell \, e^{j[MP_\ell + \frac{2\pi i \ell}{N}]} \quad . \tag{3.1}$$

Given the element excitations, the mode inputs are given by [4]

$$M_\ell = \frac{1}{\sqrt{N}} \sum_{i=1}^{N} EA_i \, e^{j[EP_i - \frac{2\pi i \ell}{N}]} \quad . \tag{3.2}$$

Note the following:

E_i = complex excitation of the i^{th} element (volts)

M_ℓ = complex excitation of the ℓ^{th} mode (volts)

N = number of elements = number of mode inputs In this case N = 8

MA_ℓ = amplitude of the ℓ^{th} mode input

MP_ℓ = phase of the ℓ^{th} mode input (radians)

EA_i = amplitude of the ith element excitation (volts), and

EP_i = phase of the i^{th} element excitation (radians).

Once the element excitations for the desired antenna pattern are found the mode inputs are easily determined. The beam may then be

steered by applying a phase gradient across the mode inputs. To steer the beam θ radians in the clockwise direction a positive phase gradient is applied such that

$$M_{\ell} = MA_{\ell} e^{j[MP_{\ell}+\ell\theta]} \quad . \tag{3.3a}$$

To steer the beam θ radians in the counter clockwise direction a negative phase gradient is applied such that

$$M_{\ell} = MA_{\ell} e^{j[MP_{\ell}-\ell\theta]} \quad . \tag{3.3b}$$

Beam steering is performed by a computer controlled six bit phase shifter [5].

The beam forming/beam steering system combines signals from all eight array elements to simultaneously provide sum (Σ) and difference (Δ) receive beams [3]. Ideal Σ and Δ beam patterns are shown in Figure 11. The element excitations and mode inputs for both the Σ and Δ beams, at zero degrees azimuth (pointing toward the nose of the aircraft), are given in Table 1 [4].

The azimuth angle of the target aircraft is determined by combining the Σ and Δ beams according to the following [4]:

$$\text{Monopulse Characteristic} = 20 \log_{10} \frac{|\Sigma+j\Delta|}{|\Sigma-j\Delta|} \quad . \tag{3.4}$$

Because Σ and Δ are 90° out of phase this produces the monopulse characteristic curve shown in Figure 12. This curve, and therefore the receiver output, is linearly proportional to the target azimuth angle

TABLE I

(a) ELEMENT EXCITATIONS FOR Σ AND Δ BEAMS
AT ZERO DEGREES AZIMUTH (TOWARD NOSE OF AIRCRAFT)

ELEMENT EXCITATIONS: SUM BEAM

ELEMENT NO.	AMPLITUDE	PHASE (DEGREES)
1	.482	32.3742
2	.109	37.8493
3	.234	-78.1094
4	.232	-48.9456
5	.240	-78.2374
6	.105	35.5149
7	.477	32.0745
8	.592	9.1814

ELEMENT EXCITATIONS: DIFFERENCE BEAM

ELEMENT NO.	AMPLITUDE	PHASE (DEGREES)
1	.371	90.9364
2	.537	135.1673
3	.137	150.721
4	.104	4.03708
5	.259	-.270649
6	.543	-42.3221
7	.427	-88.7265
8	.021	-30.3929

TABLE I (Continued)

(b) MODE INPUTS TO BUTLER MATRIX TO PRODUCE THE Σ AND Δ BEAM ELEMENT EXCITATIONS

MODE INPUTS: SUM BEAM

MODE NO.	AMPLITUDE (VOLTS)	PHASE (DEGREES)
-3	.152	-99.9442
-2	.214	-19.8993
-1	.473	46.14
0	.644	3
1	.478	45.163
2	.214	-20.545
3	.152	-99.671
4	.00101	0

MODE INPUTS: DIFFERENCE BEAM

MODE NO.	AMPLITUDE (VOLTS)	PHASE (DEGREES)
-3	.209	76.0642
-2	.254	151.01
-1	.683	-142.86
0	.102	4
1	.537	39.163
2	.324	-24.545
3	.161	-105.67
4	.00101	0

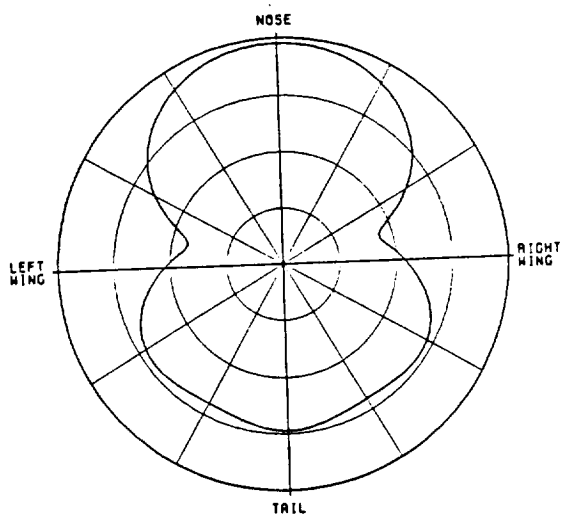

(a) Σ beam

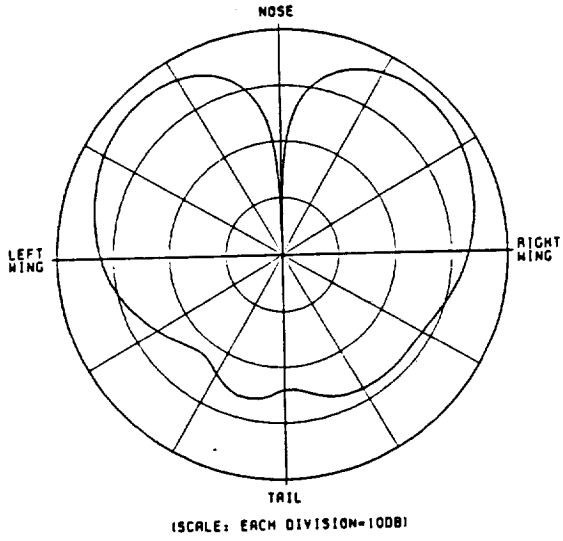

(b) Δ beam

Figure 11. Ideal TCAS II azimuth patterns.

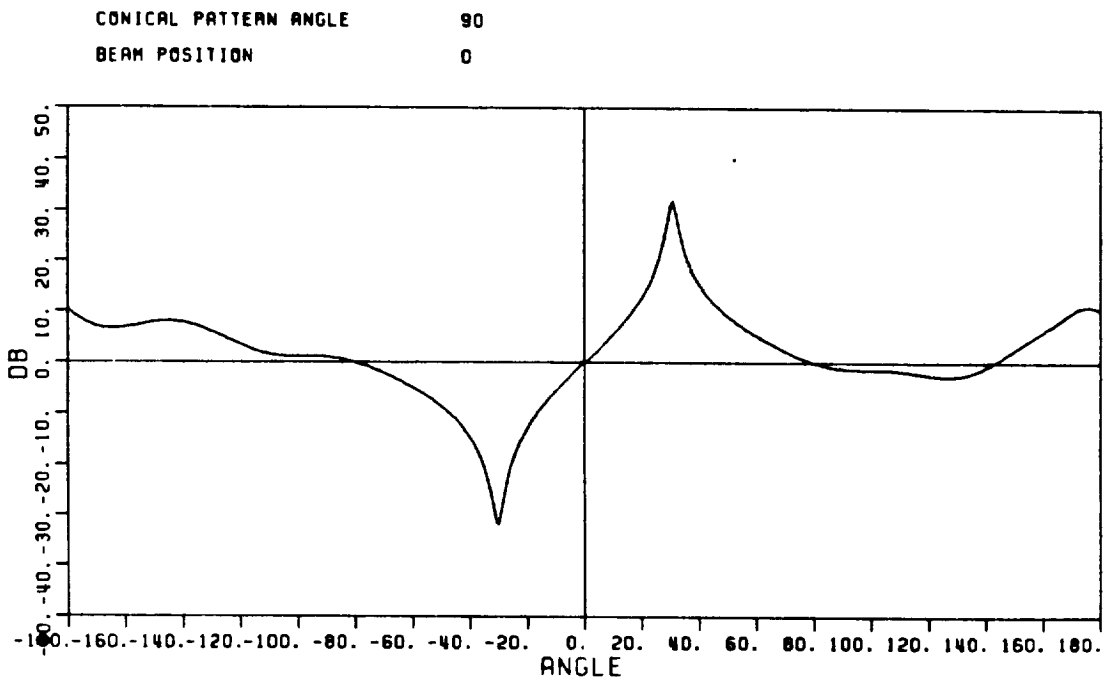

Figure 12. Ideal TCAS II monopulse characteristic.

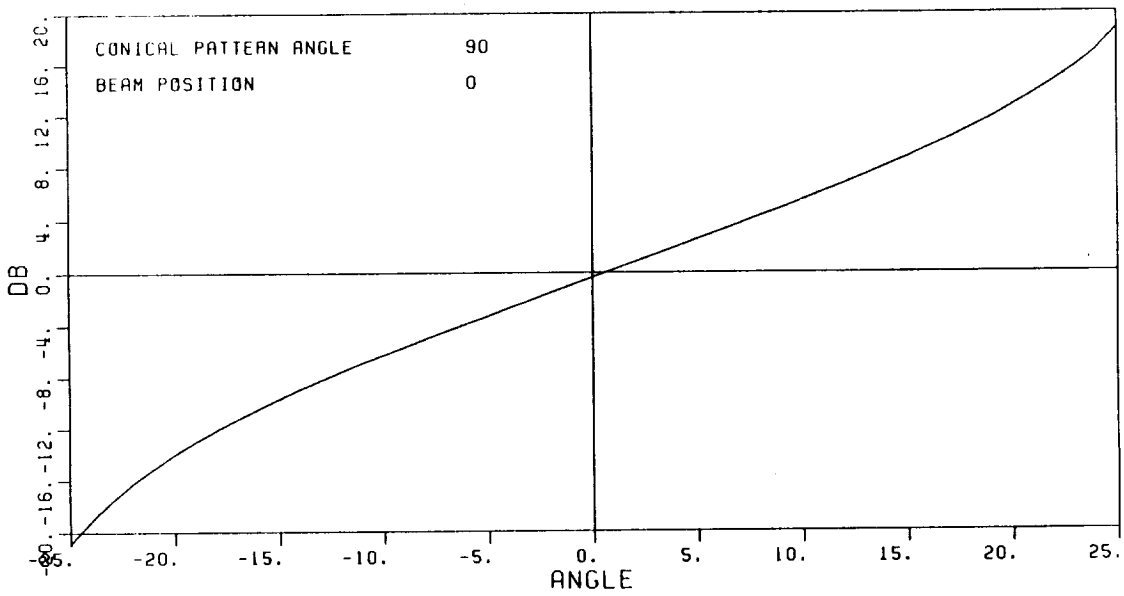

Figure 13. Expanded monopulse characteristic showing linearity around antenna boresight.

between approximately plus and minus 25 degrees off antenna boresight as illustrated in Figure 13. The receiver output is compared with values generated by a look up table in order to determine the actual azimuth angle of the target.

The circular array of top loaded monopoles is modeled by eight pairs of radially aligned one quarter wavelength monopoles as illustrated in Figure 14a. The distance between the two monopoles in each pair is one quarter wavelength and the radius of the entire array of monopoles is 6.39 inches.

A monopole pair is used to model each top loaded monopole in the array in order to facilitate the simulation of the effects of top loading and coupling between elements. These are effects which the aircraft code can not account for, and they must therefore be taken into consideration when modeling the circular array.

Both coupling and top loading are accounted for, in this case, by exciting each monopole pair such that it has a 15 dB front to back ratio. This was achieved by exciting the inner monopole of each pair with a signal of amplitude (.698) and phase (45°) and the outer element with amplitude (1.0) and phase (-45°) [4]. The azimuth pattern of the monopole pair simulating array element 8 is shown in Figure 14b. Because the number of elemental radiators exceeds the limit imposed by the aircraft code, each pattern calculation for the cicular array is done in eight separate executions of the code. Each time, only the source input data representing one of the eight monopole pairs is used. In order to simulate the curvature of the array the phase reference point is set midway between the two monopoles. The code then treats

each monopole as if it is mounted on a plane tangential to the composite ellipsoid at the phase reference point. This method results in eight data files for each pattern cut, each data file representing the contribution to the total field of one array element.

The sum of these eight data files would represent the pattern of the circular array if all eight elements were fed with the same excitation. We obtain the Σ or Δ beam pattern by first selecting the mode inputs for the desired beam, positioned at zero degrees azimuth angle (toward the aircraft nose), from Table 1. The mode inputs are then modified accoding to Equation (3.3) for the desired beam azimuth angle. The corresponding element excitations are determined by Equation (3.1). Each element pattern is weighted by multiplying the data file for that element by the proper excitation. All eight of the weighted data files are then added together to produce a single file for the steered Σ or Δ beam.

Once the Σ and Δ pattern data files have been produced, for the same beam position and elevation angle, they are combined according to Equation (3.4) thus producing the monopulse characteristic result which is used to determine the angle of the target aircraft by the TCAS II system.

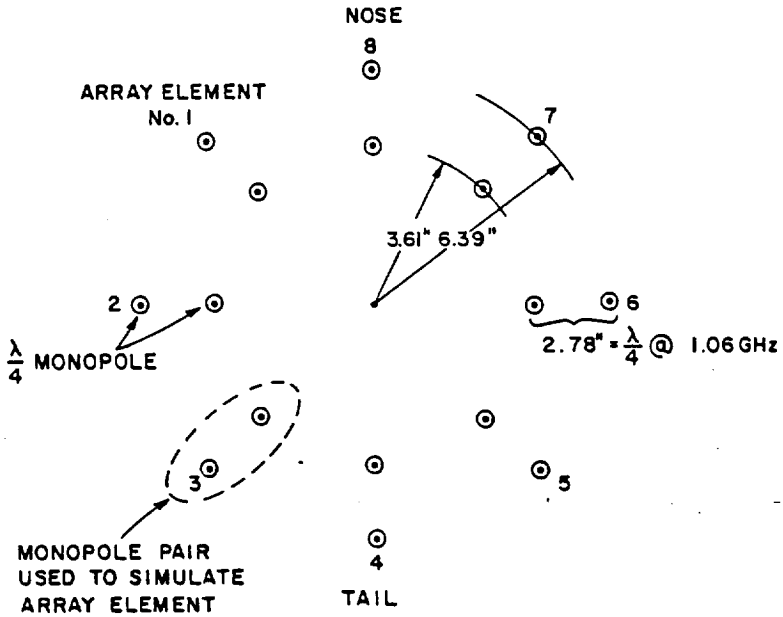

a) Top view of circular array computer model.

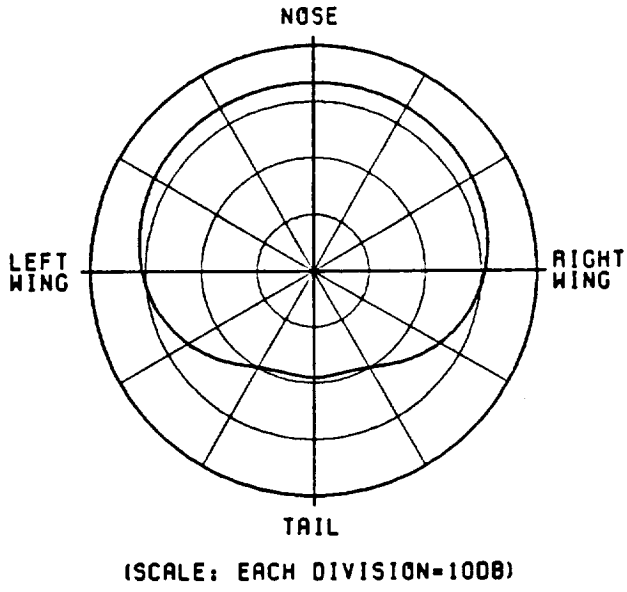

b) Azimuth pattern of the monopole pair simulating array element 8.

Figure 14. TCAS II Circular array simulation.

IV. ANALYSIS OF TCAS II SYSTEM ON 737 AIRCRAFT

The aircraft model used, in order to assess the effects of scattering on the performance of the TCAS II system, is the Boeing 737 as shown in Figure 15. The 737 was chosen because it is a widely used commercial aircraft, the model geometry is relatively simple and the accuracy of the model had already been verified [2].

The 737 computer model, as shown in Figure 16, consists of a composite ellipsoid fuselage and four flat plates. Each wing is modeled by a single, four sided, flat plate attached to the fuselage. The vertical stabilizer is composed of two flat plates attached to the fuselage. In order to simulate the thickness and wedge shape of the vertical stabilizer, the two plates are also attached to each other at the leading edge. Note that Figure 16 is merely a drawing of the input data and that the aircraft code extends the edges of the plates to attach them to the fuselage. The TCAS II antenna is mounted just over the leading edge of the wings as indicated in Figure 16.

The input data for the TCAS II antenna mounted on the 737 is given in Appendix I.

Figure 17 shows ideal Σ and Δ beam far field patterns azimuth patterns at 15 degrees elevation. These patterns were obtained by deleting the plates representing the wings and vertical stabilizer from the input data before executing the aircraft code. Figure 18 shows the same pattern cut with wings and vertical stabilizer included. The effects of scattering may be noted in the areas $\pm 120°$ from the nose of

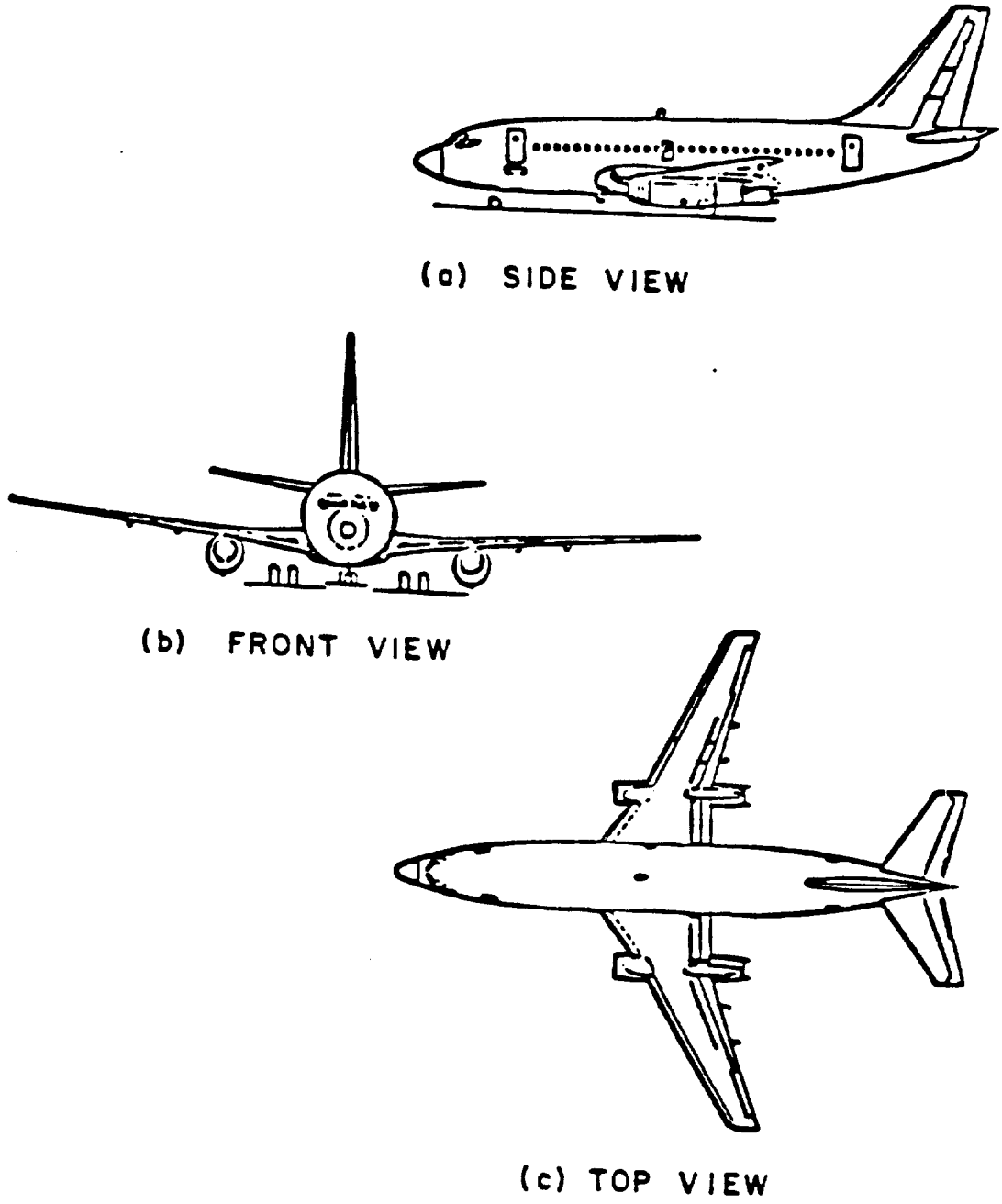

Figure 15. Boeing 737 aircraft.

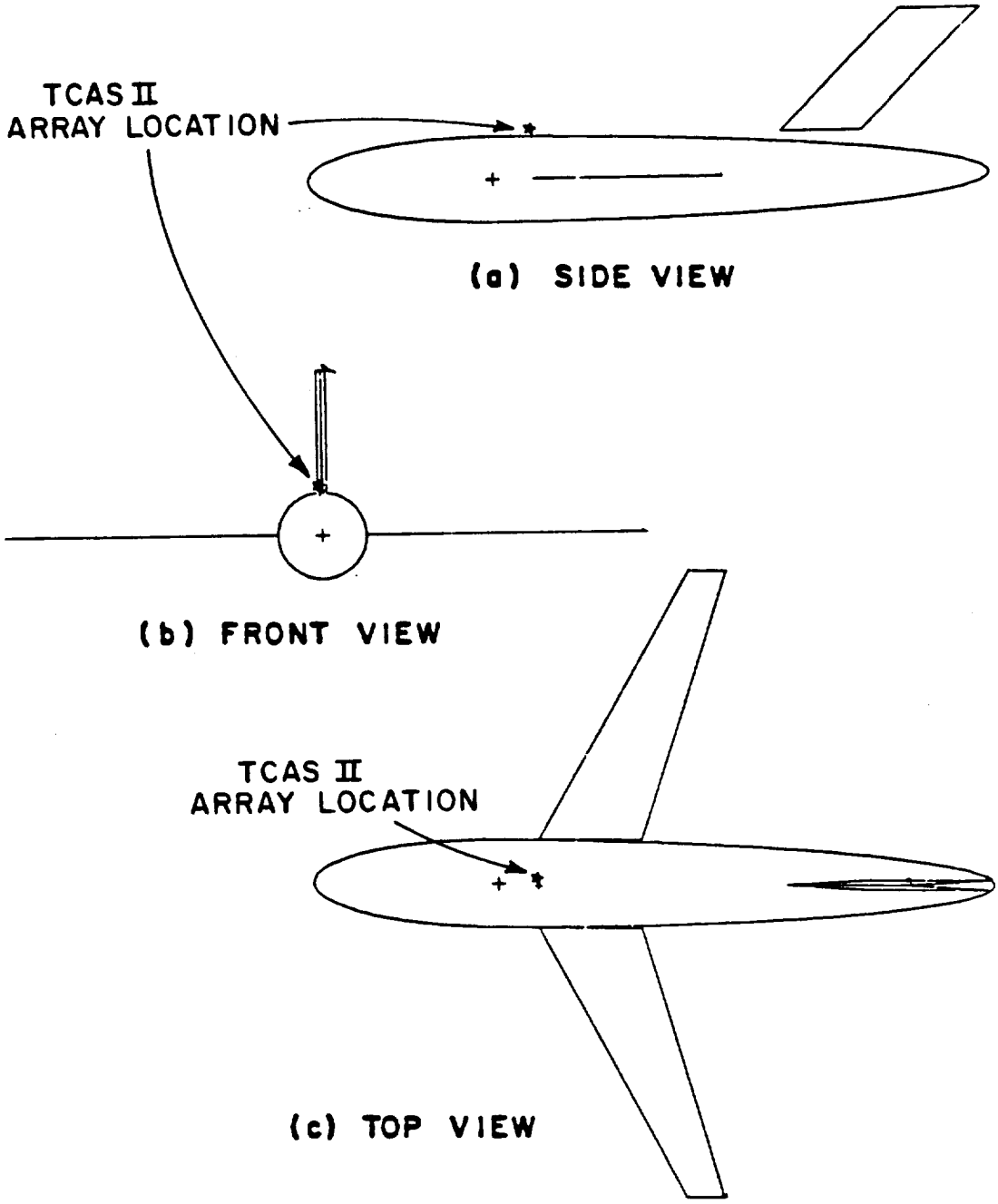

Figure 16. Computer-simulated model of the Boeing 737.

the aircraft and at 180 degrees from the nose (toward the tail). No severe discontinuities exist in the pattern indicating that no higher order terms need to be included in the field computation.

Figures 19 and 20 show the reflected and diffracted field terms from the wings only. These terms affect the total azimuth pattern only in the region of 120 degrees from the nose of the 737 with the diffracted field term being about 7 dB below the reflected field.

Figures 21 and 22 show the reflected and diffracted field terms from the vertical stabilizer only. These terms affect the azimuth pattern in the direction of the tail only, and the diffracted term is the major source of distortion.

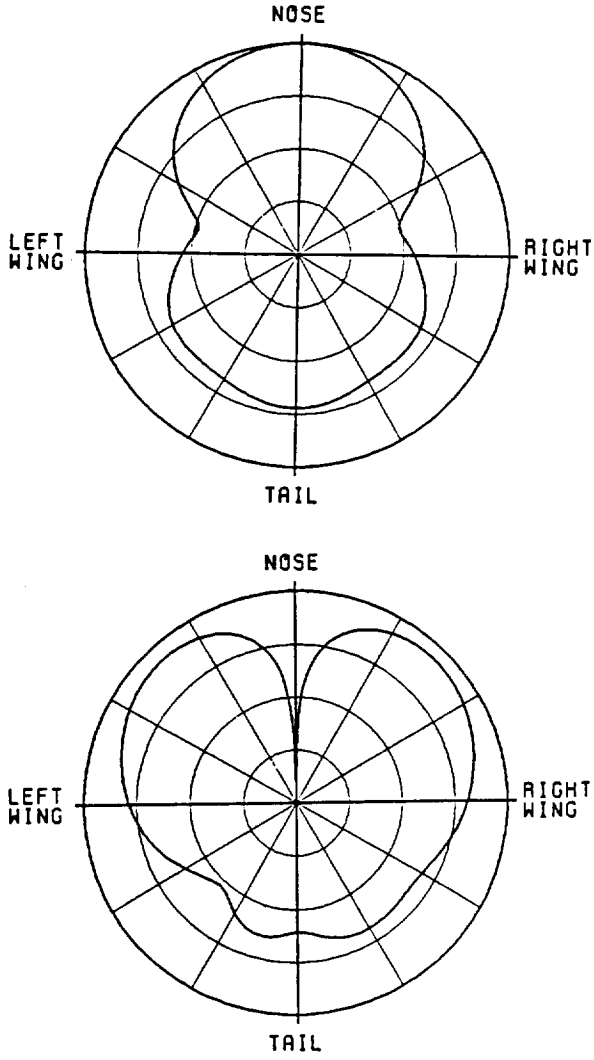

Figure 17. Ideal Σ and Δ beam patterns.
Aximuth cut at 15° elevation above horizontal.
No plates included in model.

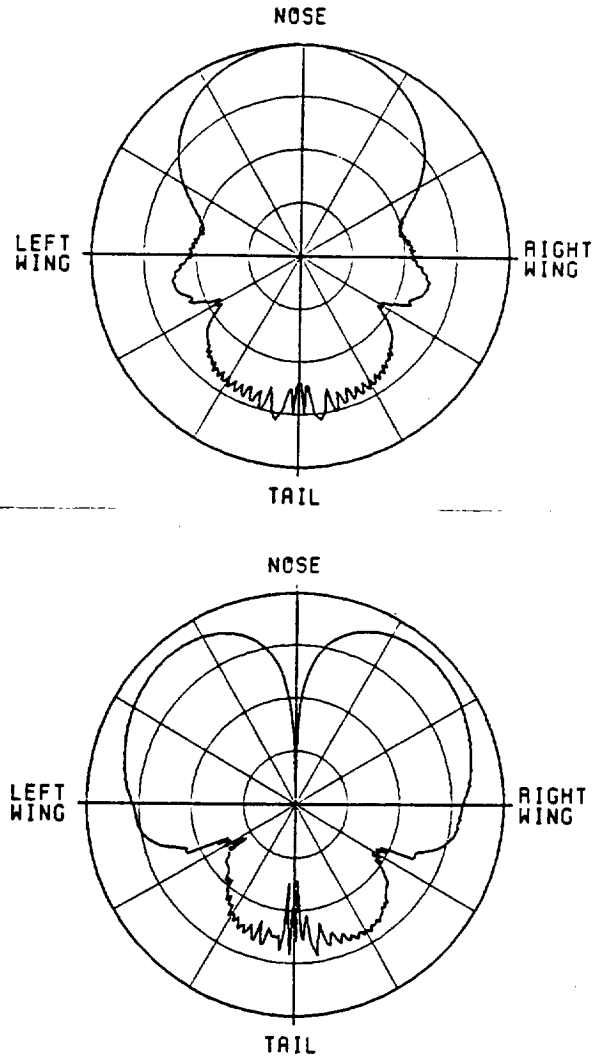

Figure 18. Σ and Δ beam azimuth patterns at elevation angle of 15° above horizontal. All plates included in aircraft model.

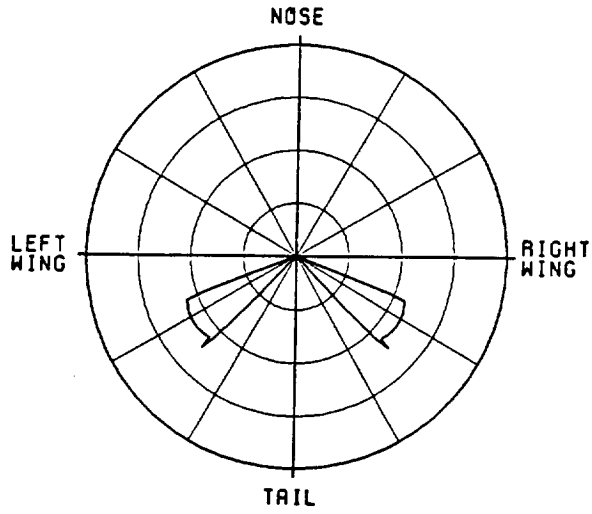

(a) Σ beam

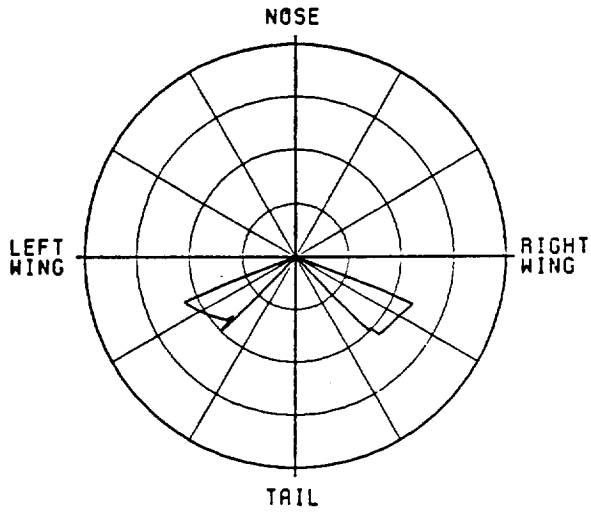

(SCALE: EACH DIVISION=10DB)

(b) Δ beam

Figure 19. Azimuth pattern cut 15° elevation angle reflected field from wings only.

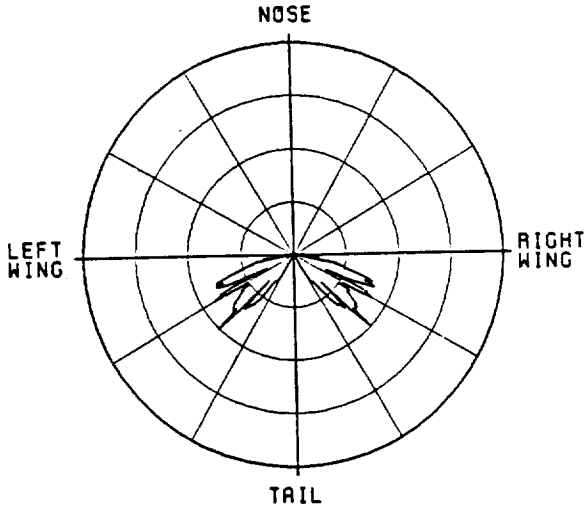

(a) Σ beam

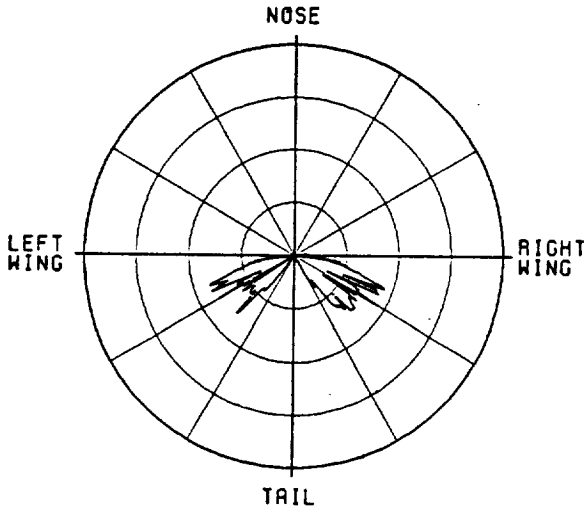

(SCALE: EACH DIVISION=10DB)

(b) Δ beam

Figure 20. Azimuth pattern cut, 15° elevation angle diffracted field from wings only.

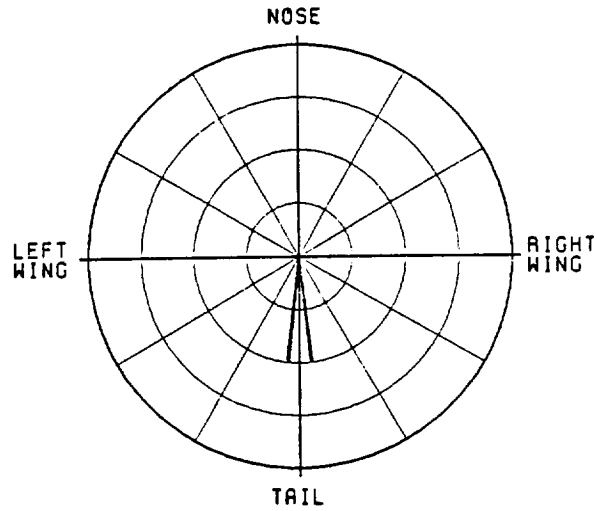

(a) Σ beam

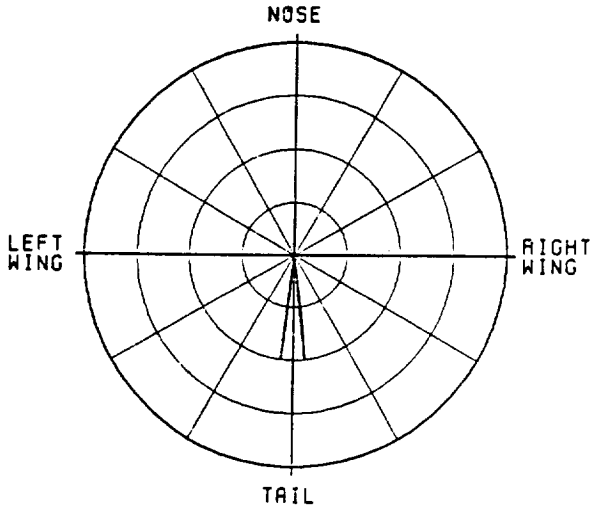

(SCALE: EACH DIVISION=10DB)

(b) Δ beam

Figure 21. Azimuth pattern at 15° elevation angle reflected field from vertical stabilizer only.

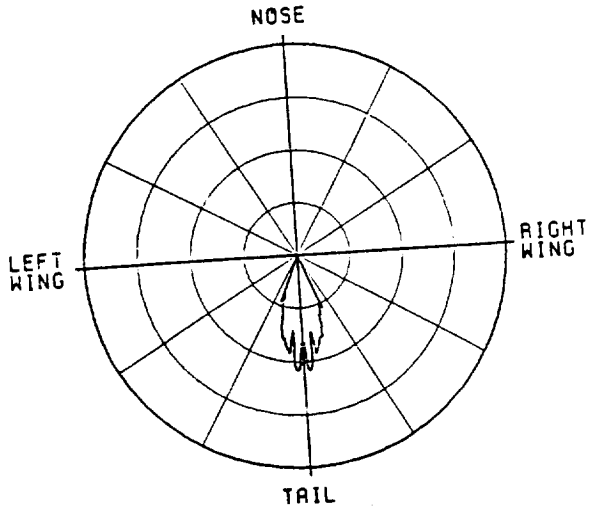

(a) Σ beam

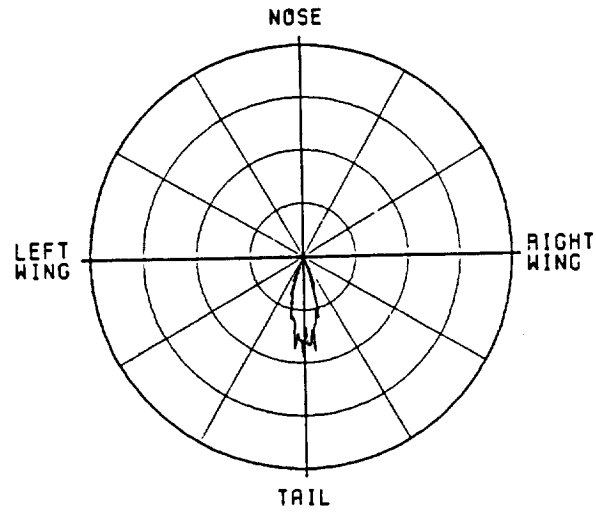

(SCALE: EACH DIVISION=10DB)

(b) Δ beam

Figure 22. Azimuth pattern at 15° elevation angle diffraction from vertical stabilizer only.

Figure 23 shows the monopulse characteristic produced from the ideal Σ and Δ beam patterns in Figure 17. Comparing this to the monopulse characteristic in Figure 24, obtained from the Σ and Δ beams in Figure 18, reveals that scattering has no effect when the beams are steered toward the nose of the aircraft. As the beams are steered toward the right wing as shown in Figure 25, the scattering from the wing begins to cause very small ripple in the monopulse characteristic as illustrated in Figure 26. When the beams are over the right wing, as shown in Figure 27, the ripple in the azimuth patterns in the region of the main beam become even more severe. The ripple in the corresponding monopulse characteristic increases accordingly as illlustrated in Figure 28. As the beams are steered into the region between the right wing and tail, as shown in Figure 29, the main beam shows the effects of both the strong reflection from the wing and the diffraction from the vertical stabilizer. This degrades even further in the monopulse characteristic as illustrated in Figure 30. In Figure 31 the beams are pointed directly at the tail. This strongly illuminates the vertical stabilizer and the diffraction causes large ripple magnitude in the azimuth patterns. The corresponding monopulse characteristic in Figure 32 shows severe distortion due to this ripple.

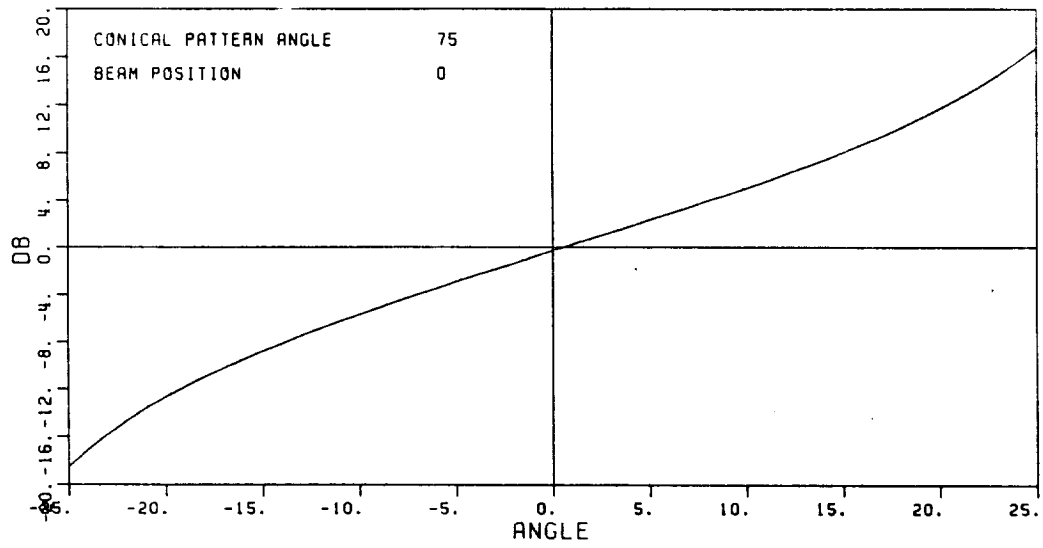

Figure 23. Ideal monopulse characteristic.

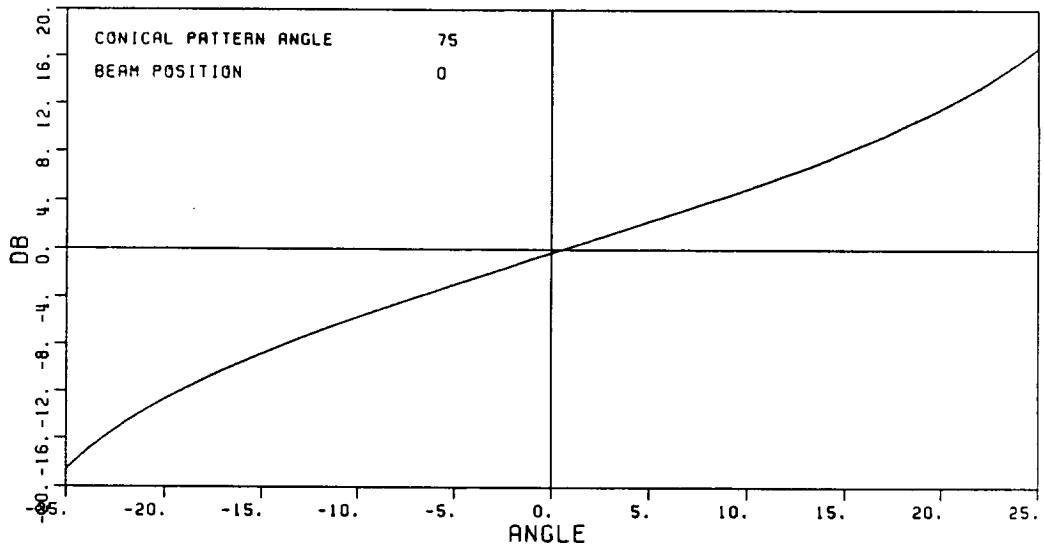

Figure 24. Monopulse characteristic of TCAS II antenna mounted on a Boeing 737.

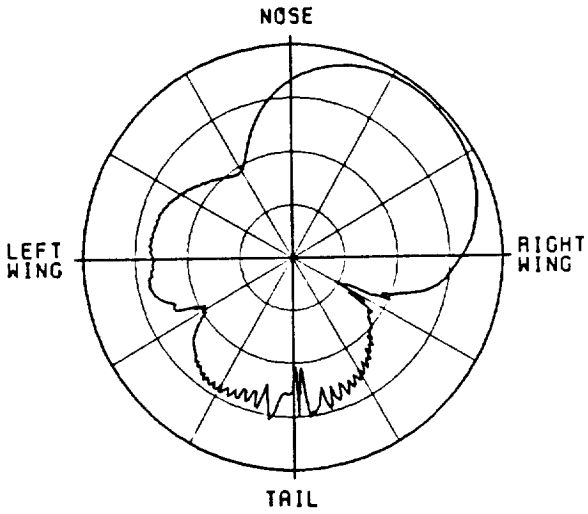

(a) Σ beam

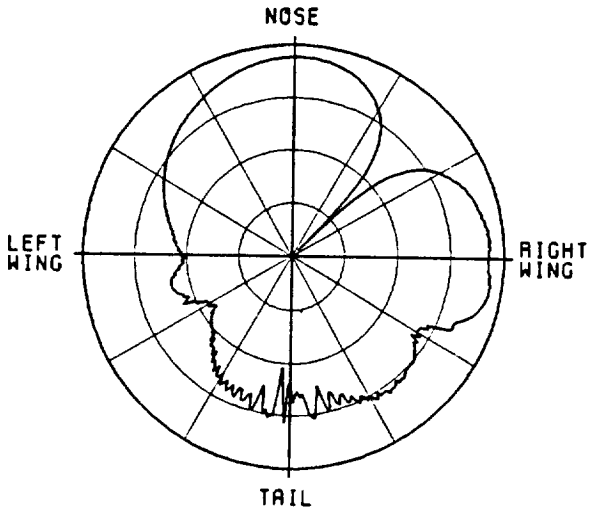

(SCALE: EACH DIVISION=10DB)

(b) Δ beam

Figure 25. Azimuth pattern cut at 15° elevation.

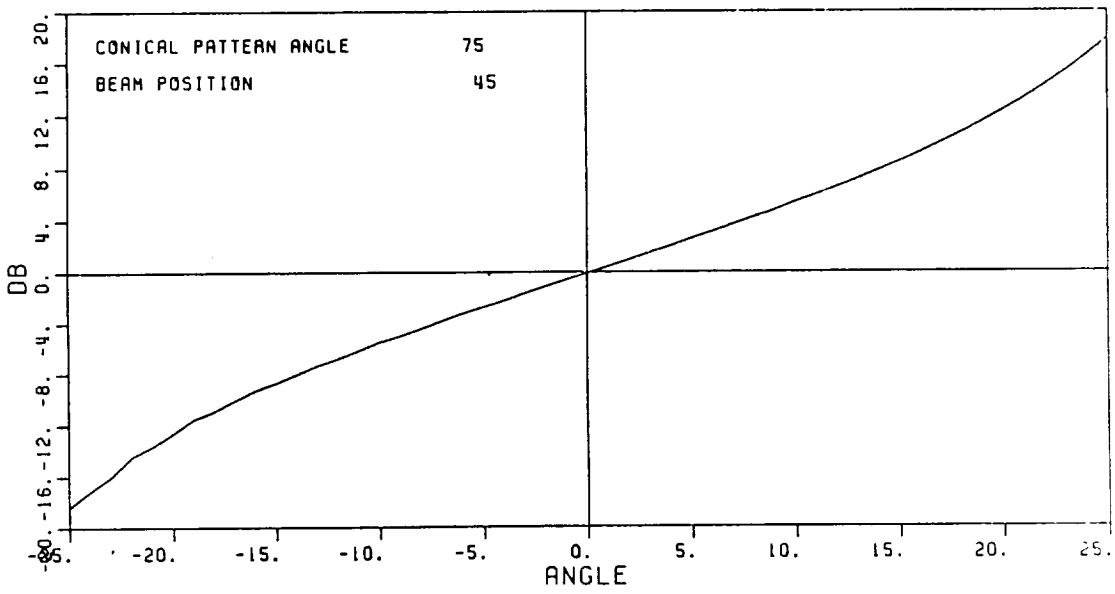

Figure 26. Monopulse characteristic of TCAS II mounted on a Boeing 737. Beams steered to 45° to the right of the nose.

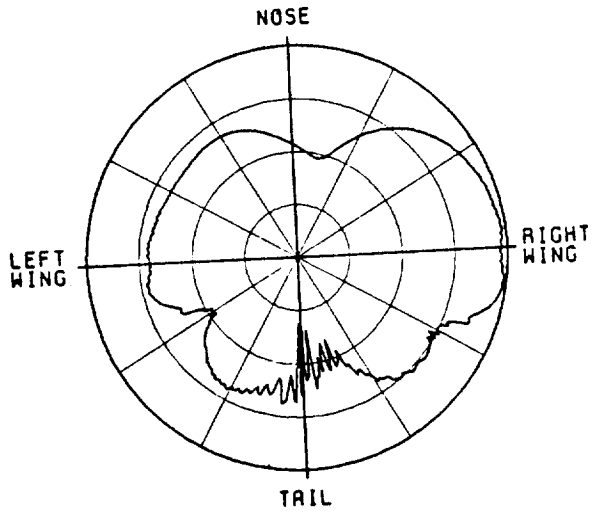

(a) Σ beam

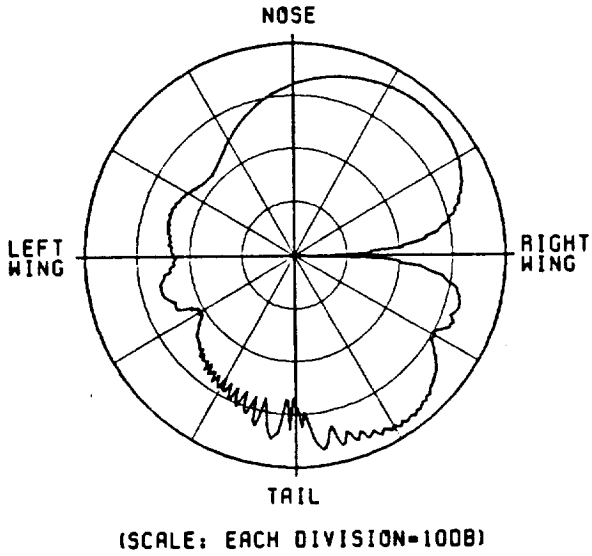

(b) Δ beam

Figure 27. Azimuth pattern cut, 15° elevation angle.

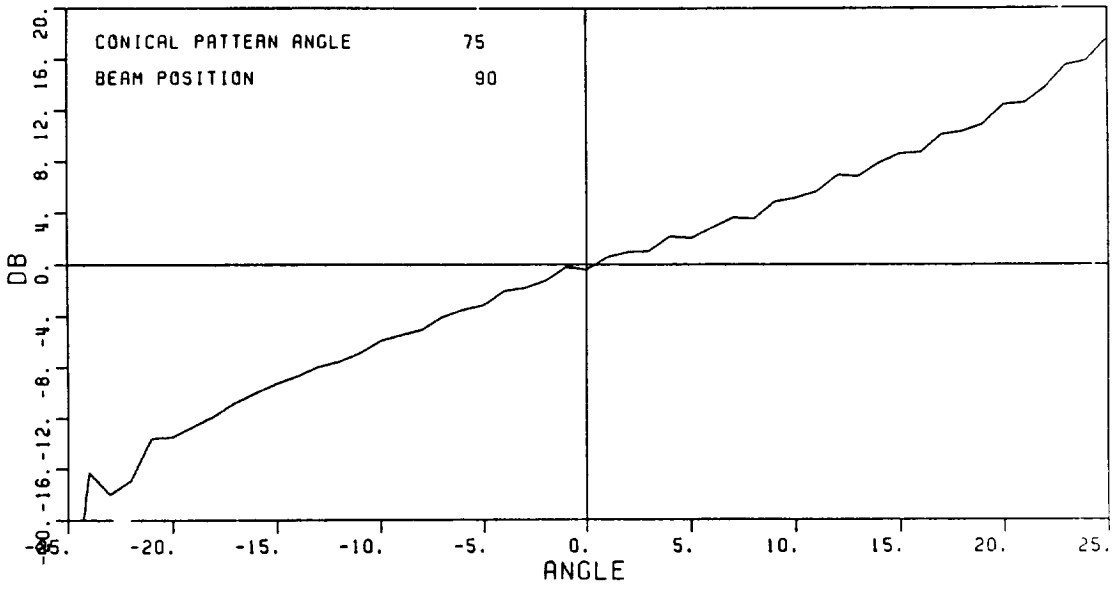

Figure 28. Monopulse characteristic of TCAS II mounted on a Boeing 737. Beams steered over right wing.

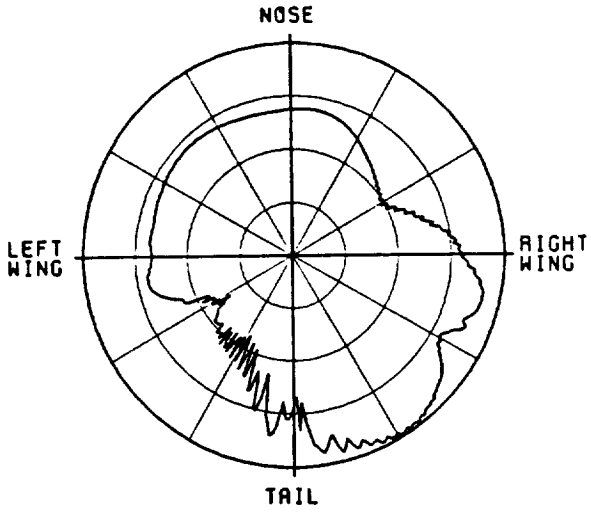

(a) Σ beam

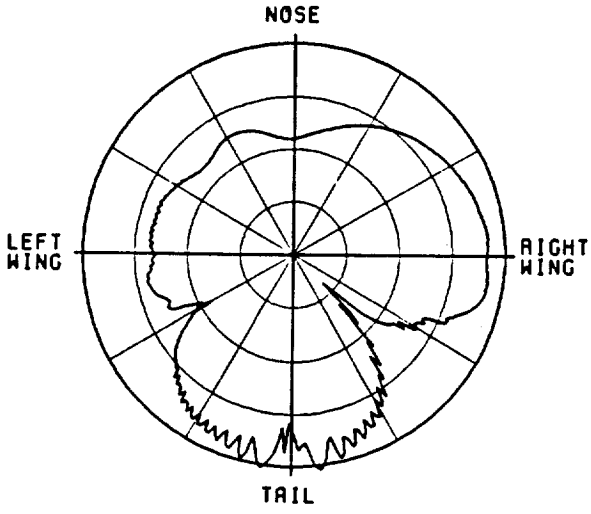

(SCALE: EACH DIVISION=10DB)

(b) Δ beam

Figure 29. Azimuth pattern cut 15° elevation angle for 135° azimuth beam position.

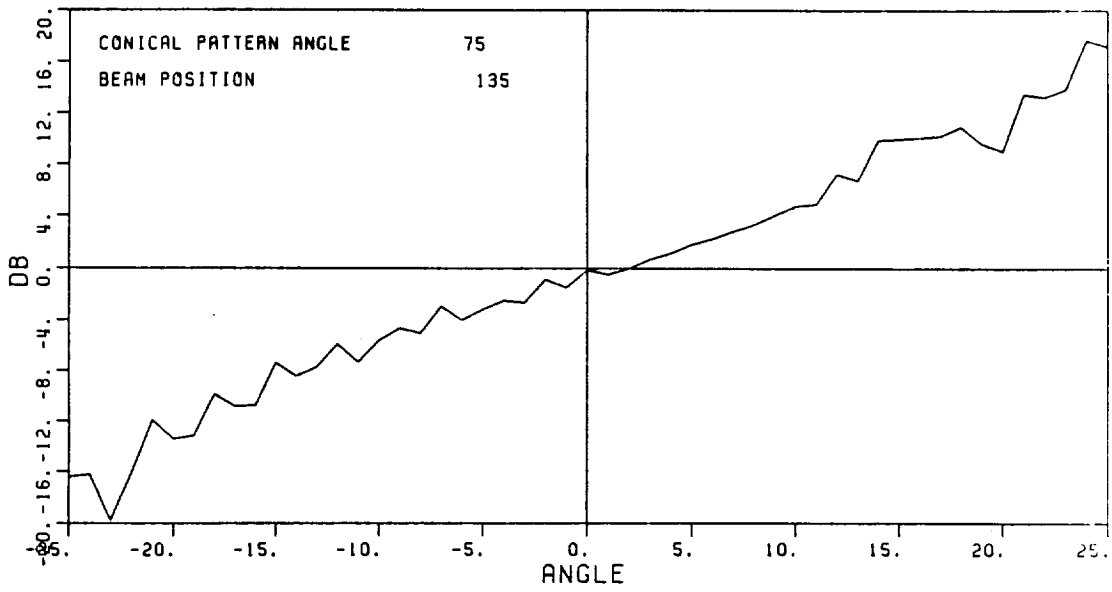

Figure 30. Monopulse characteristic of the TCAS II mounted on a Boeing 737. Beam steered to 135° to the right of the nose.

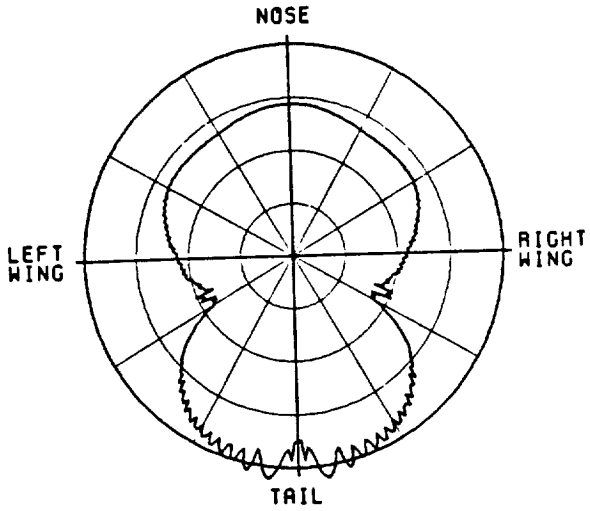

(a) Σ beam

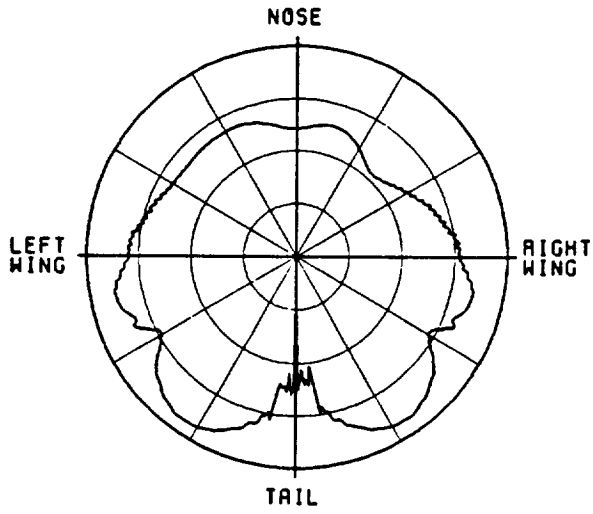

(b) Δ beam

Figure 31. Azimuth pattern cut, 15° elevation angle.

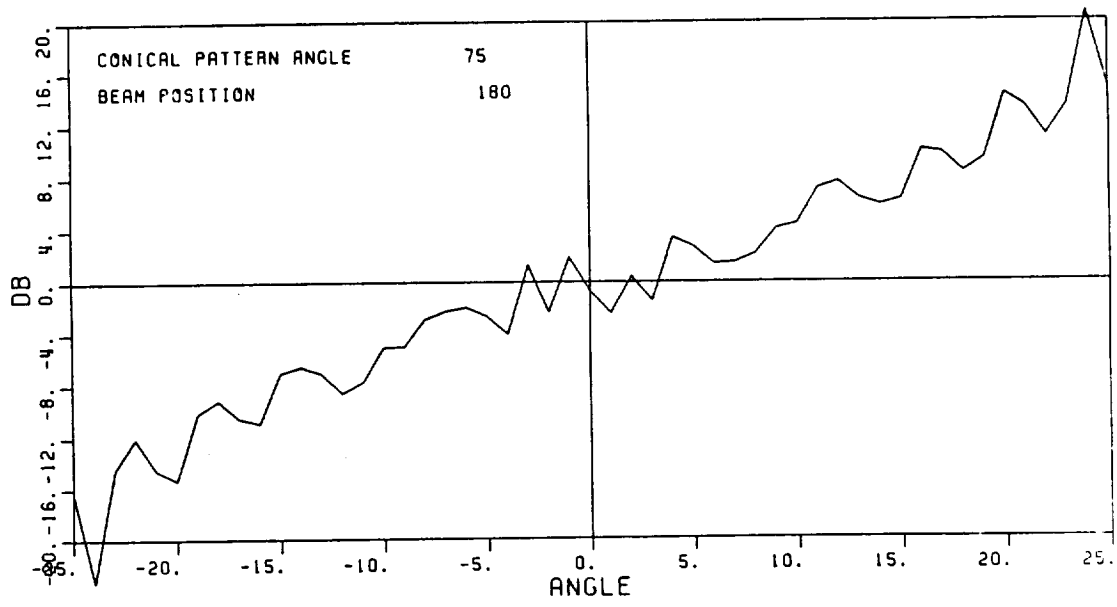

Figure 32. Monopulse characteristic of the TCAS II mounted on a Boeing 737. Beams steered toward tail.

Figures 33 through 37 illustrate the effect of varying the elevation angle of the pattern cut while the beams are directed toward the tail. Figures 33, 34, and 35 represent the azimuth patterns and monopulse characteristics of the TCAS II antenna at elevation angles of 0, 10 and 20 degrees. The magnitude of the distortion in the azimuth patterns and monopulse characteristics is approximately the same for all of these elevation angles. Figures 36 and 37 show the azimuth patterns and monopulse characteristics at elevation angles of 25 and 30 degrees. The distortion in these patterns is much less than that found in the patterns for the lower elevation angles. This is due to the fact that the pattern cut elevation angle is now above the angle at which the source field is blocked by the tail, 22 degrees, as illustrated in Figure 38.

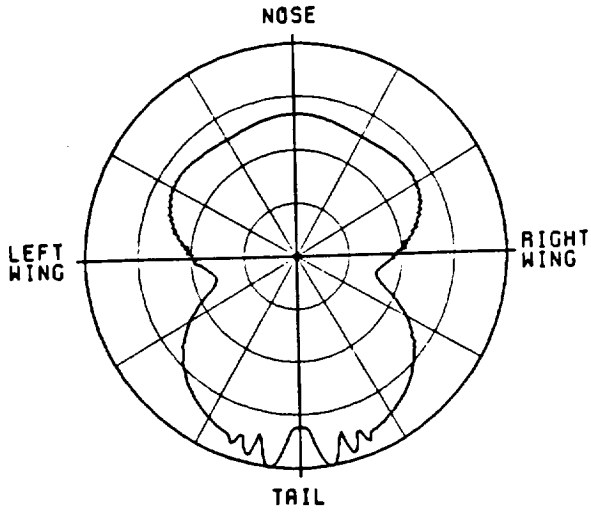

(a) Σ beam

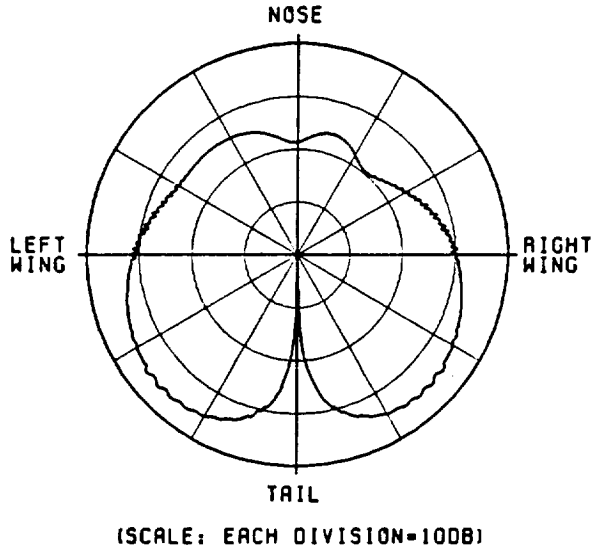

(b) Δ beam

Figure 33. Azimuth pattern cut, 0° elevation angle.

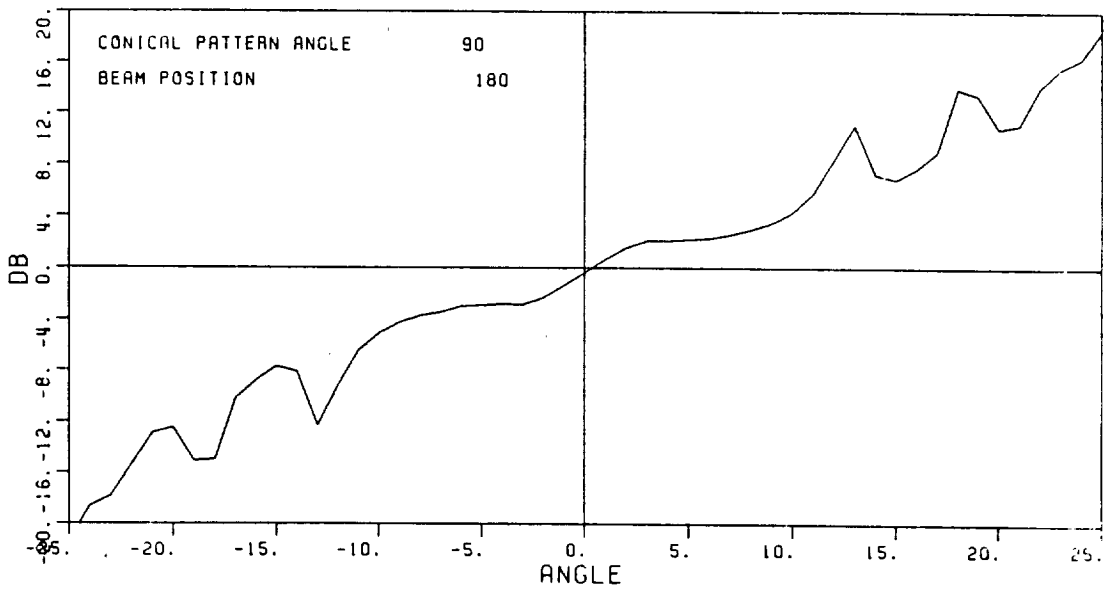

(c) corresponding monopulse characteristic

Figure 33. (Continued)

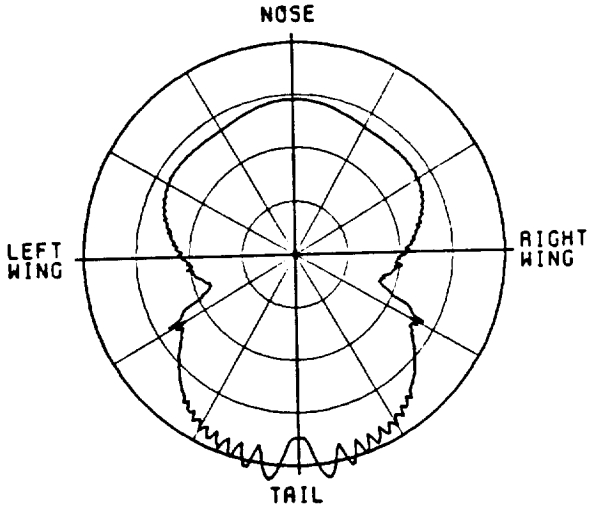

(a) Σ beam

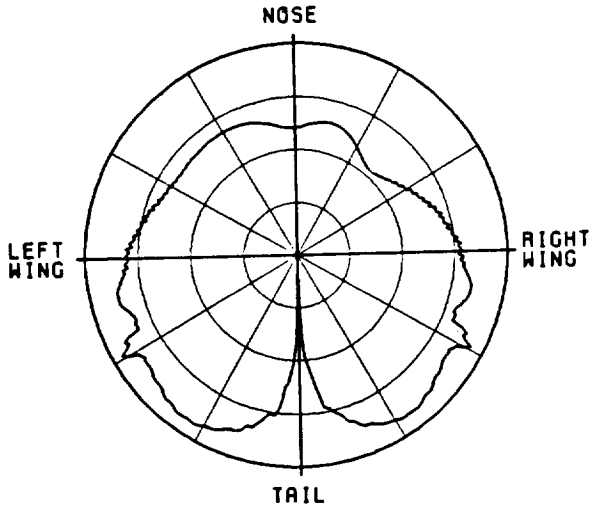

(SCALE: EACH DIVISION=10DB)

(b) Δ beam

Figure 34. Azimuth pattern cut, 10° elevation angle.

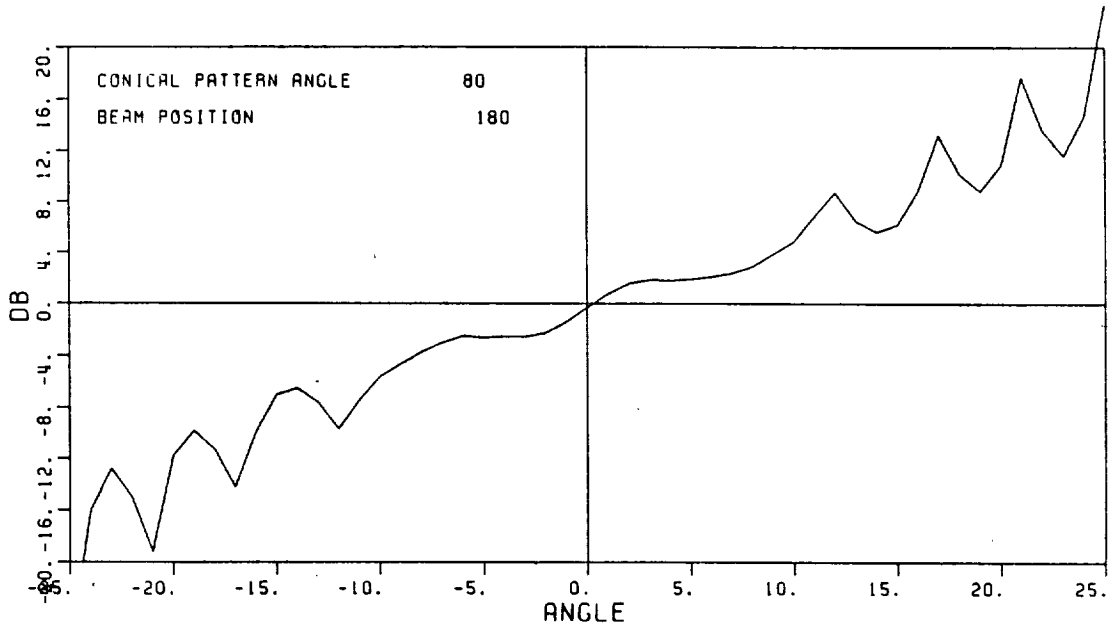

(c) Corresponding monopulse characteristic

Figure 34. (Continued).

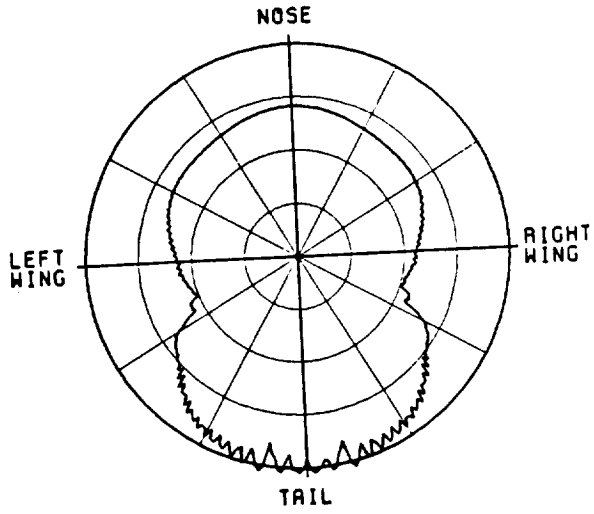

(a) Σ beam

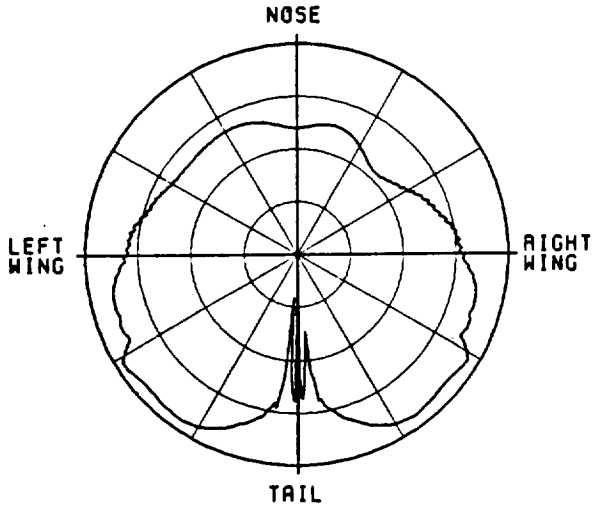

(SCALE: EACH DIVISION=10DB)

(b) Δ beam

Figure 35. Azimuth pattern cut, 20° elevation angle.

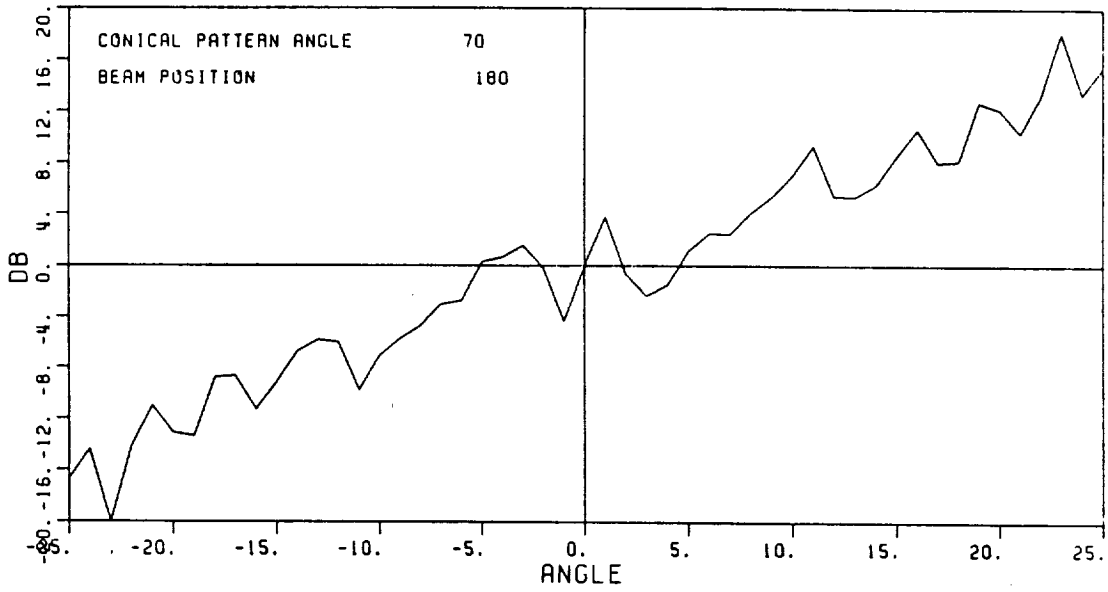

(c) Corresponding monopulse characteristic

Figure 35. (Continued).

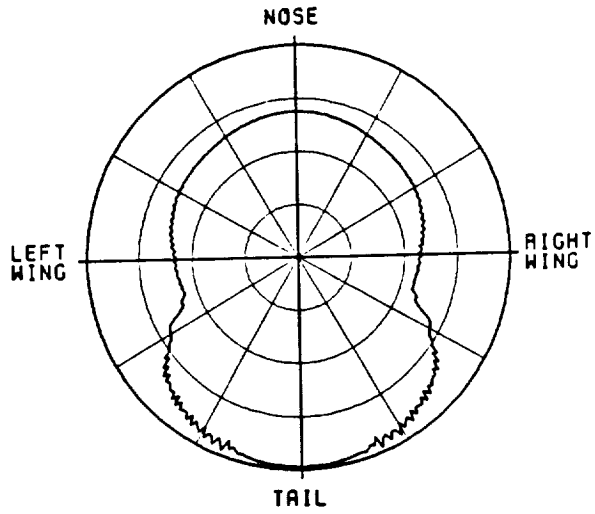

(a) Σ beam

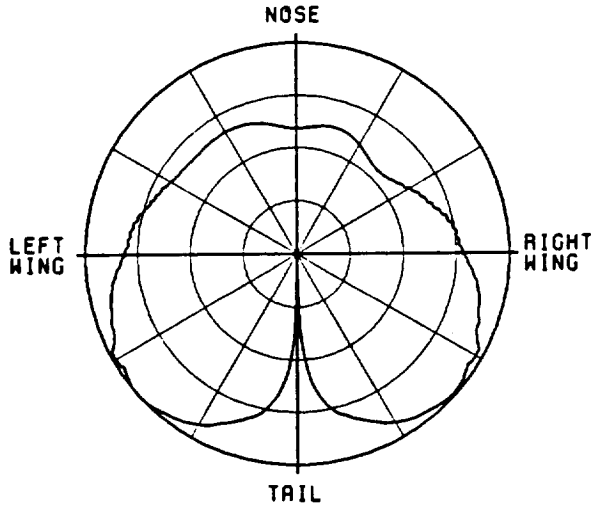

(b) Δ beam

Figure 36. Azimuth pattern cut, 25° elevation angle.

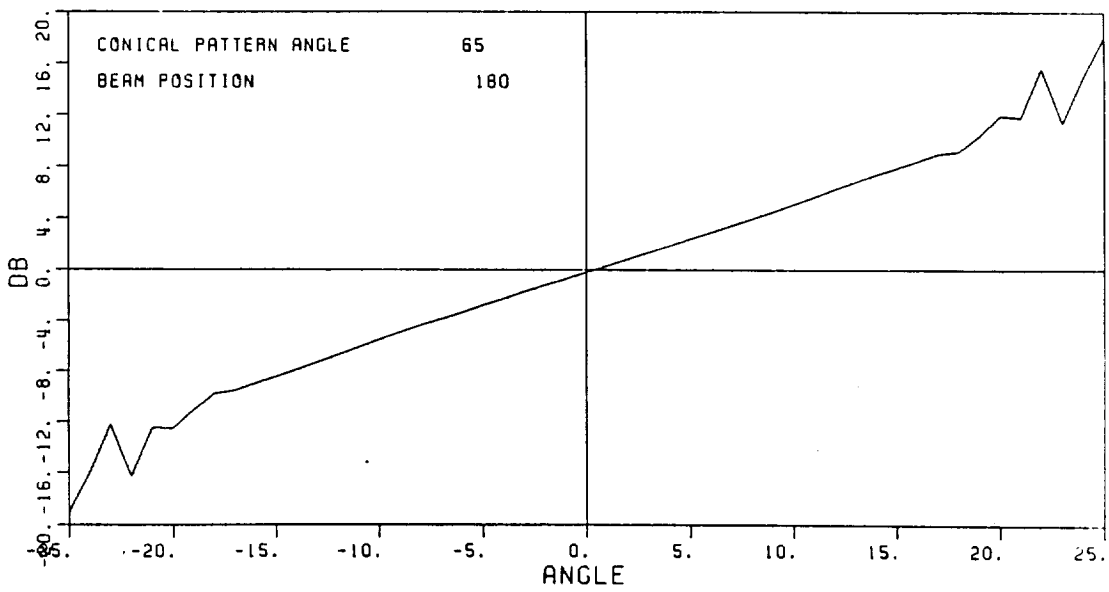

(c) Corresponding monopulse characteristic

Figure 36. (Continued).

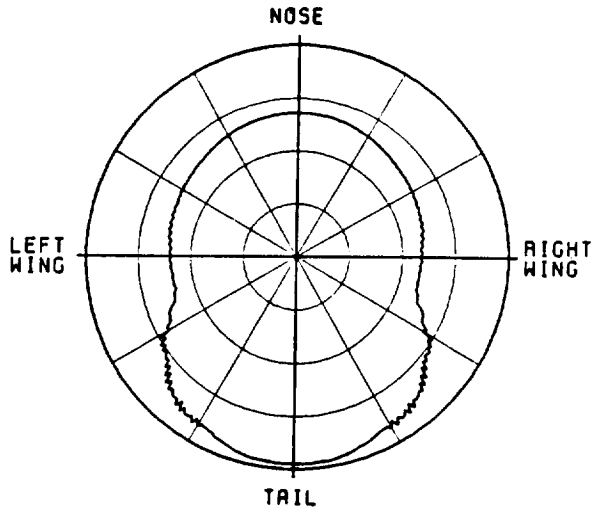

(a) Σ beam

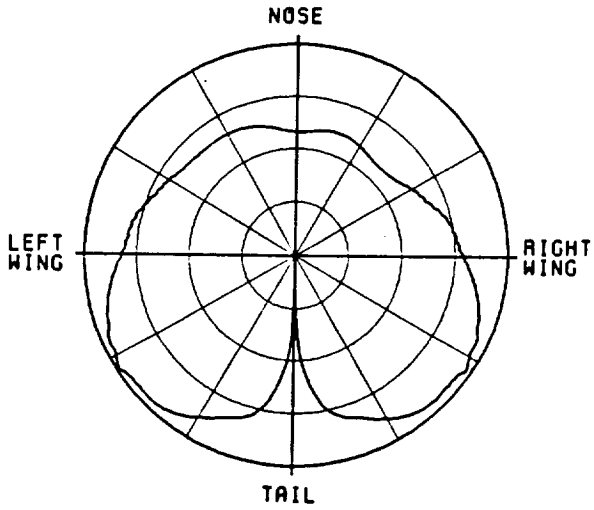

(SCALE: EACH DIVISION=10DB)

(b) Δ beam

Figure 37. Azimuth pattern cut, 30° elevation angle.

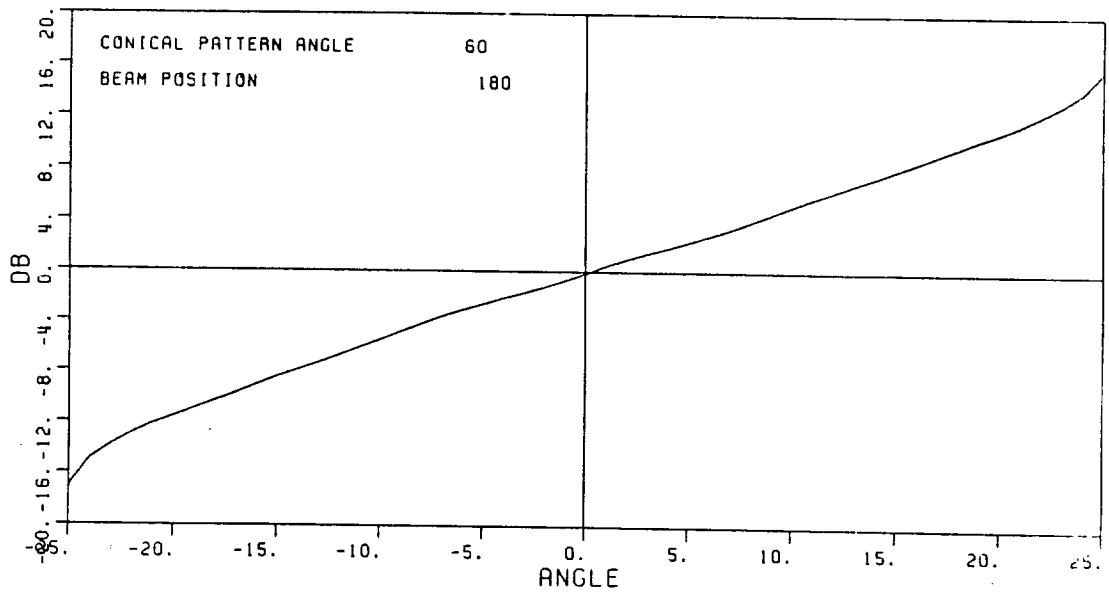

(c) Corresponding monopulse characteristic

Figure 37. (Continued).

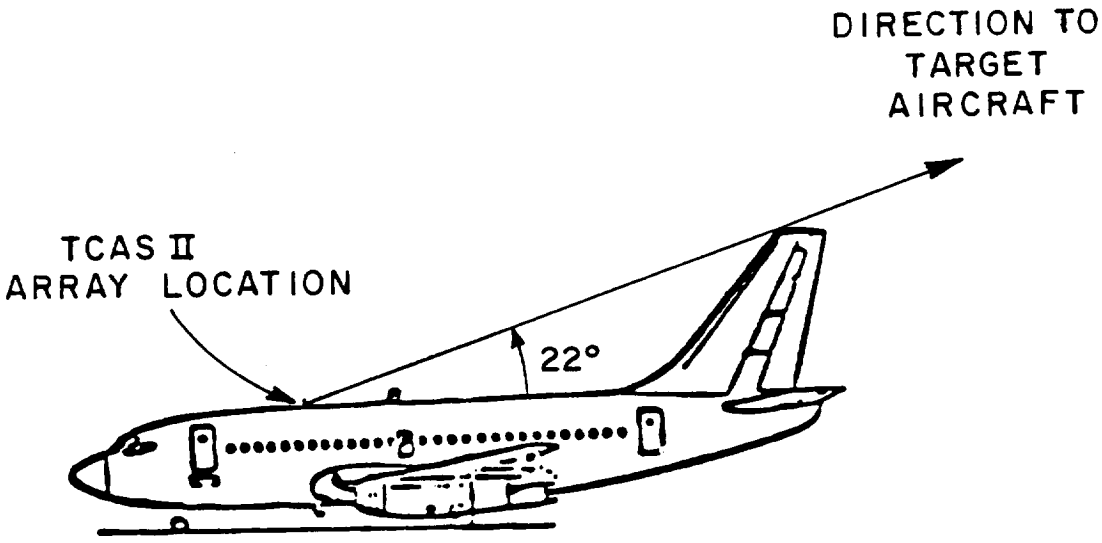

Figure 38. Side view of the Boeing 737 showing the 22° angle between the TCAS II antenna and the vertical stabilizer.

V. TCAS II ARRAY LOCATION STUDY

The purpose of this chapter is to demonstrate the fact that the effects of scattering on the Σ and Δ beams may be reduced by mounting the circular array as far away as possible from the major source of scattering, the vertical stabilizer. It will also be shown that mounting the array close to the nose of the aircraft reduces the effects of fuselage blockage at elevation angles below the horizon when the Σ and Δ beams are steered in the region forward of the wings (azimuth beam position between 0° and ±90°).

Five different antenna locations are considered as shown in Figure 39. The Σ and Δ beams are steered toward the tail of the aircraft so that the vertical stabilizer is strongly illuminated. The azimuth pattern cut is taken at a 10 degree elevation angle. Figure 40 shows the Σ and Δ beam patterns for the case when the array is mounted at position A, approximately 15 feet in front of the vertical stabilizer. The ripple magnitude in the Σ beam, in the direction of the tail, is quite large. The Δ beam remains relatively uneffected in this direction due to the null in the pattern illuminating the vertical stabilizer. The linear region of the monopulse characteristic, obtained from this case, is shown in Figure 41. The distorting effects of the scattering from the vertical stabilizer are quite severe.

The Σ and Δ beams for the array mounted at position B are shown in Figure 42. The scattering from the vertical stabilizer is still very

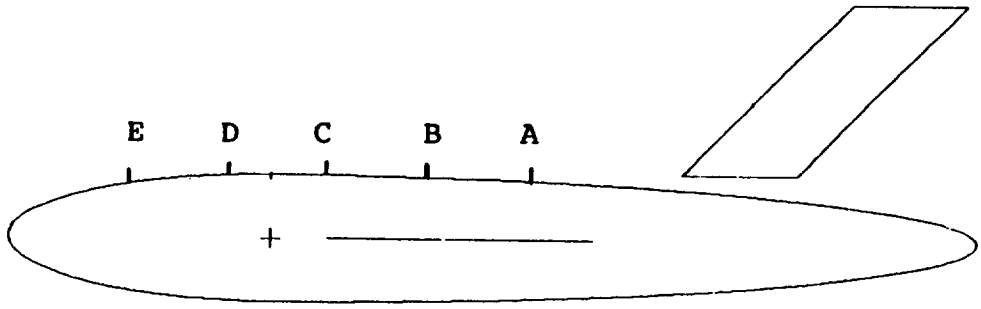

Figure 39. Five different array locations on the 737 computer model.

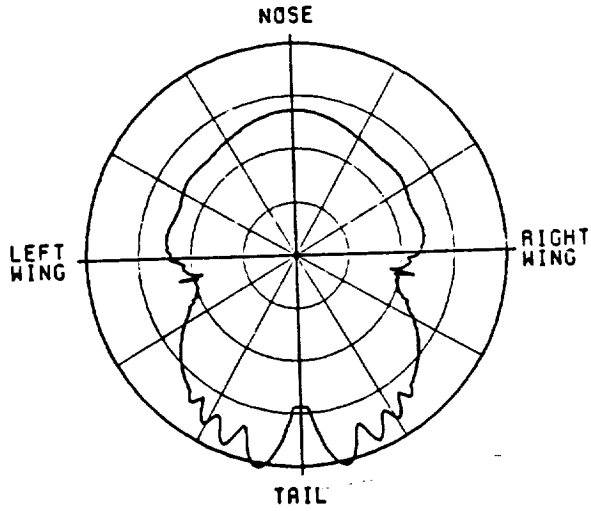

(a) Σ beam

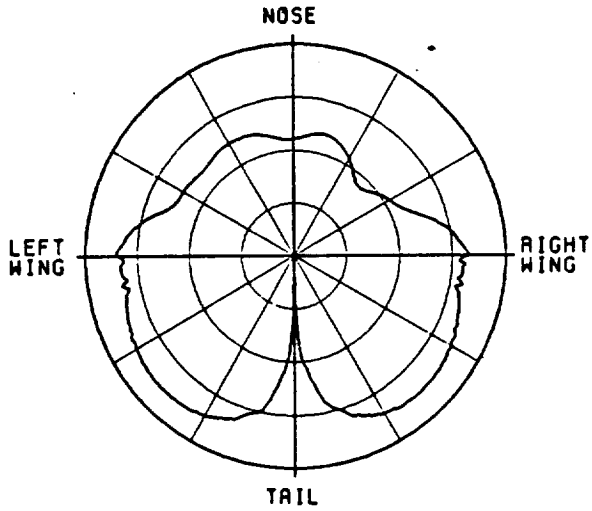

(SCALE: EACH DIVISION=10DB)

(b) Δ beam

Figure 40. Azimuth pattern at 10° elevation angle with array at position A.

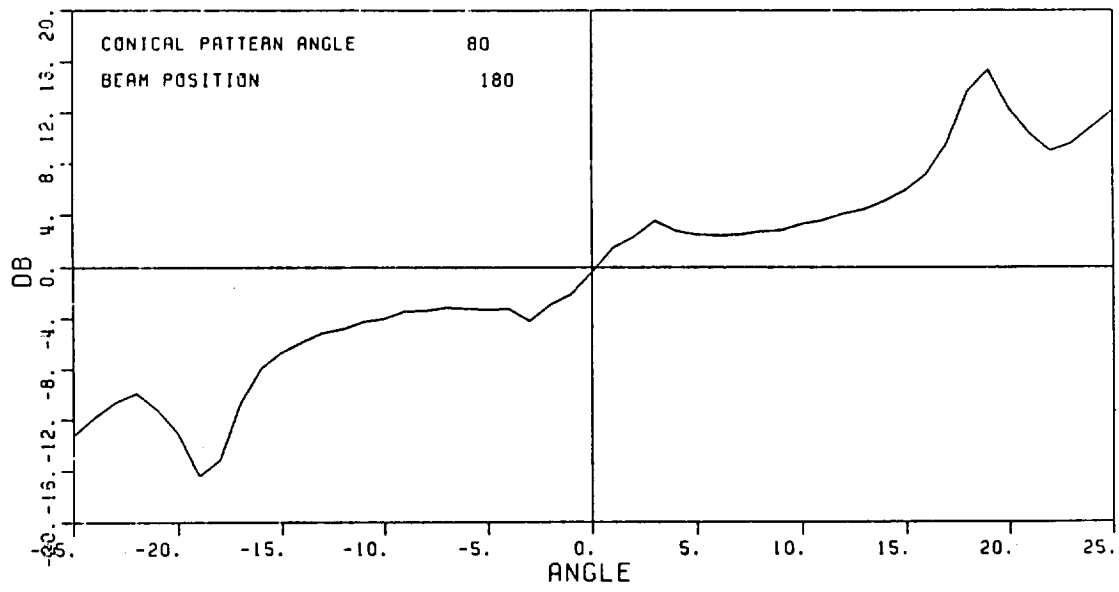

Figure 41. Monopulse characteristic for array at position A. Beam steered toward tail.

strong although less than at position A. The linear region of the monopulse characteristic, in Figure 43, shows minimal improvement.

Position C is the location where the circular array was mounted for the analysis done in Chapter 4. The Σ and Δ beams for this case are shown in Figure 44. Again the Σ beam shows a small but noticable decrease in the amplitude of the ripple caused by the vertical stabilizer. The monopulse characteristic as shown in Figure 45 is improved although the ripple frequency caused by scattering has increased, the ripple amplitude has decreased.

When the array is mounted at position D the Σ beam, as shown in Figure 46, shows further improvement. Even though the Δ beam has remained essentially uneffected, the improvement in the Σ beam has resulted in a very significant improvement in the monopulse characteristic as illustrated in Figure 47.

The last array location to be considered is at position E. The Σ and Δ beams for this case are shown in Figure 48. These patterns have a slightly different overall shape than the previous four cases. This is due to the change in the surface of the composite ellipsoid as the array location approaches the region representing the nose of the aircraft. The Σ beam in this final position exhibits a very large improvement over previous cases in that the ripple amplitude caused by the vertical stabilizer is markedly smaller. The monopulse characteristic, as shown in Figure 49, reflects this in that the amplitude of the ripple has significantly decreased.

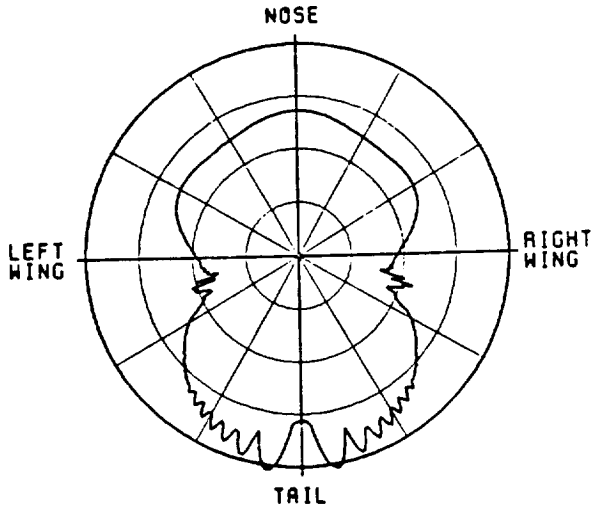

(a) Σ beam

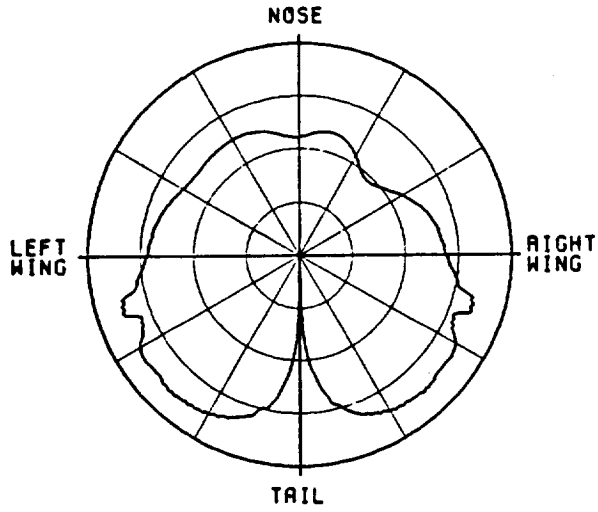

(b) Δ beam

Figure 42. Azimuth pattern at 10° elevation angle with array at position B.

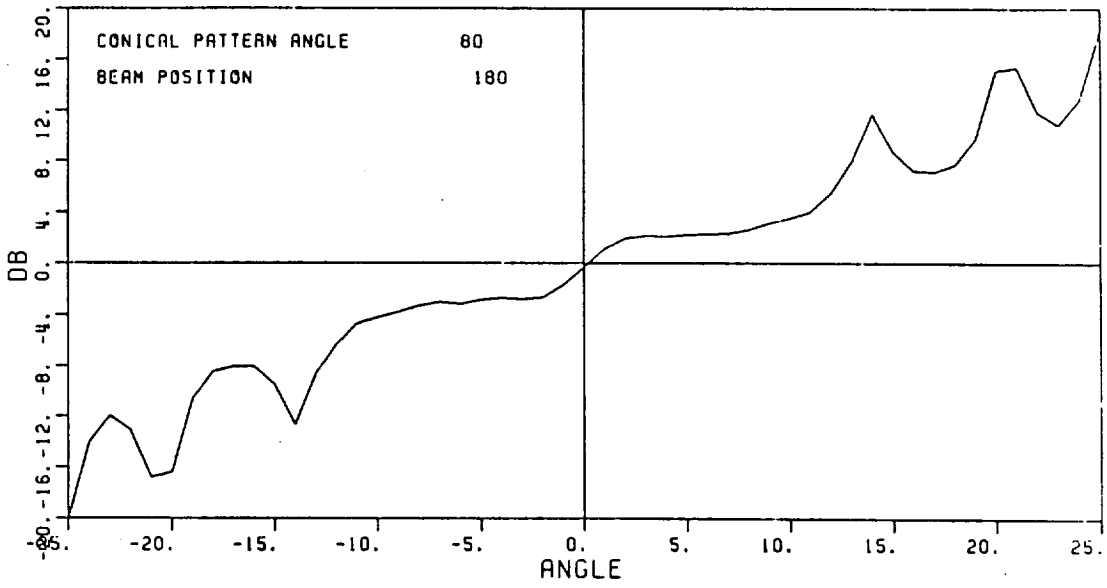

Figure 43. Monopulse characteristic for array at position B. Beam steered toward tail.

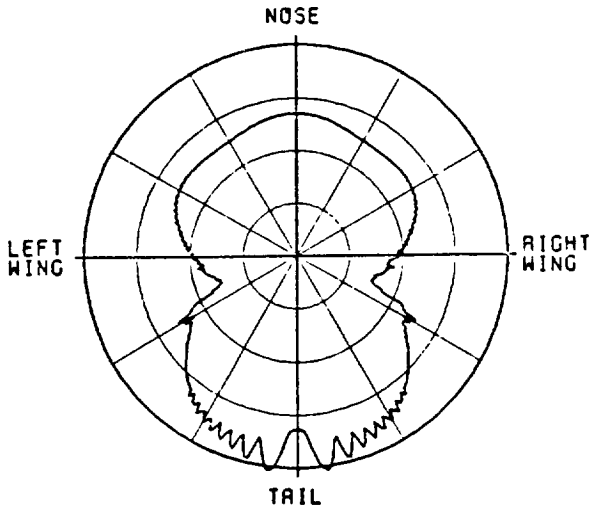

(b) Δ beam

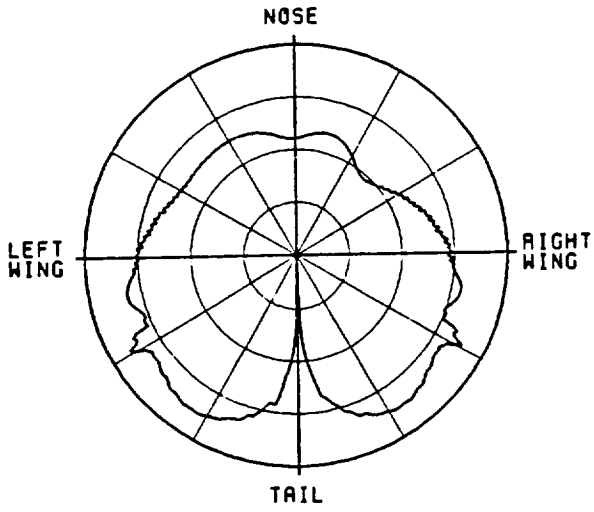

(a) Σ beam

Figure 44. Azimuth pattern at 10° elevation angle with array at position C.

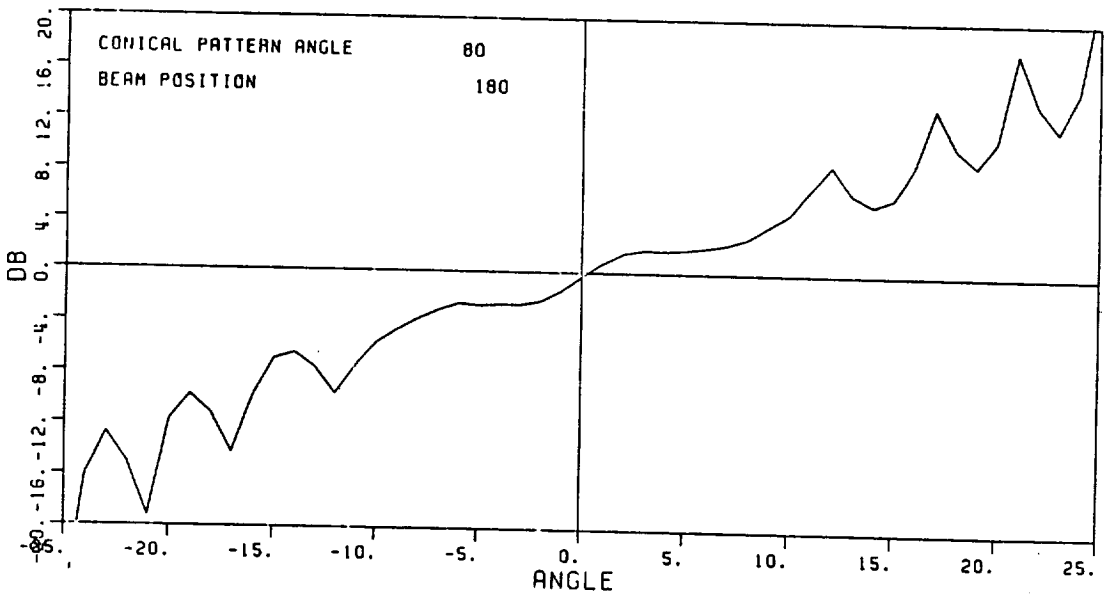

Figure 45. Monopulse characteristic for array at position C. Beam steered toward tail.

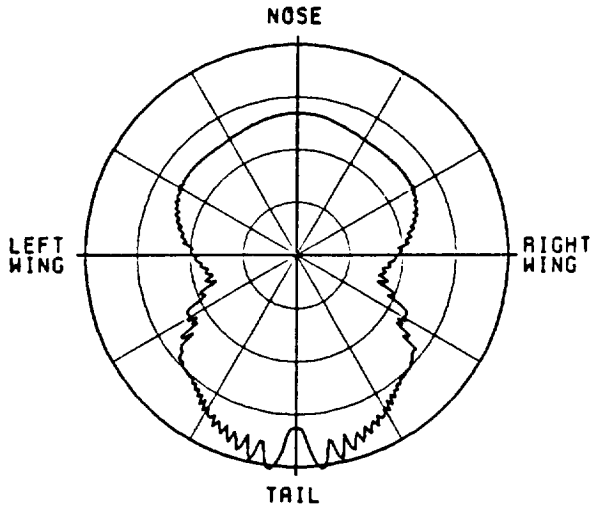

(a) Σ beam

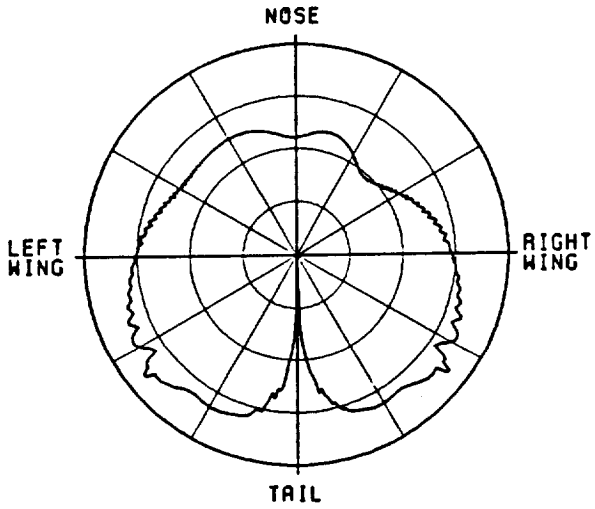

(b) Δ beam

Figure 46. Azimuth pattern at 10° elevation angle with array at position D.

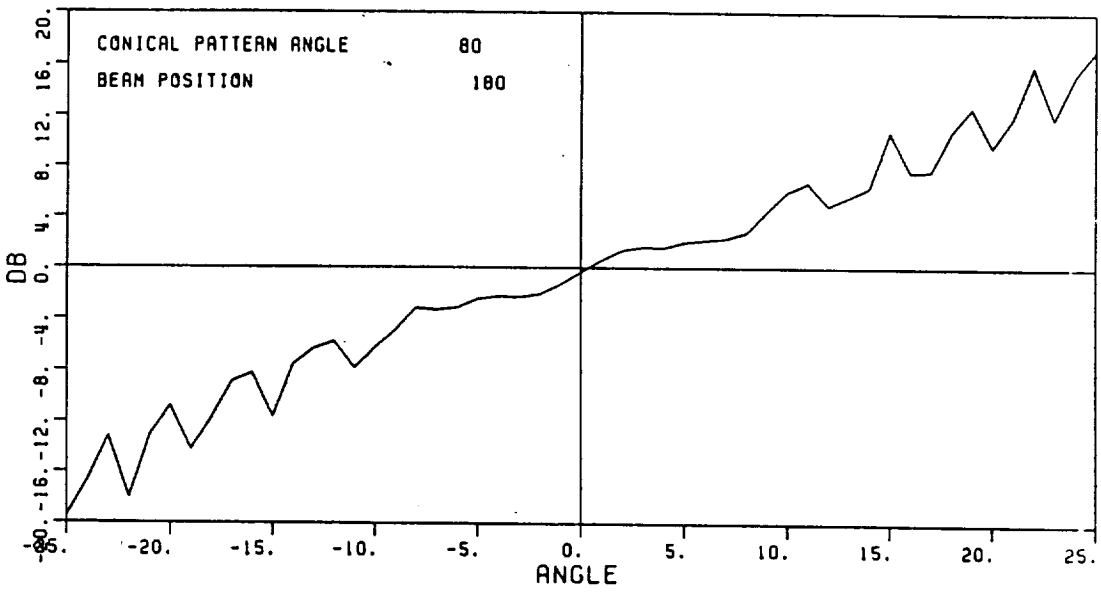

Figure 47. Monopulse characteristic for array at position D. Beam steered toward tail.

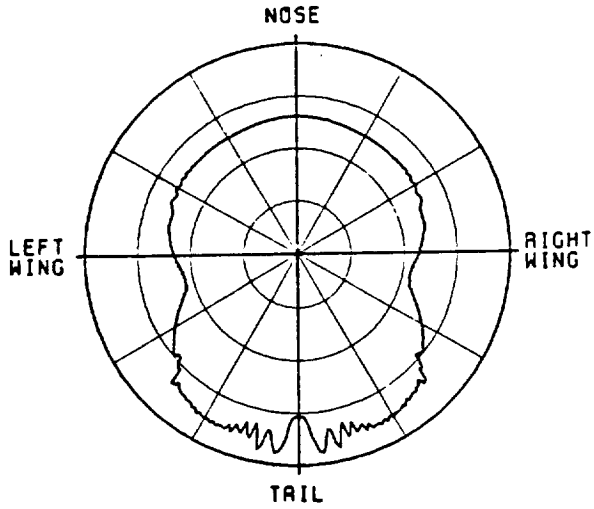

(a) Σ beam

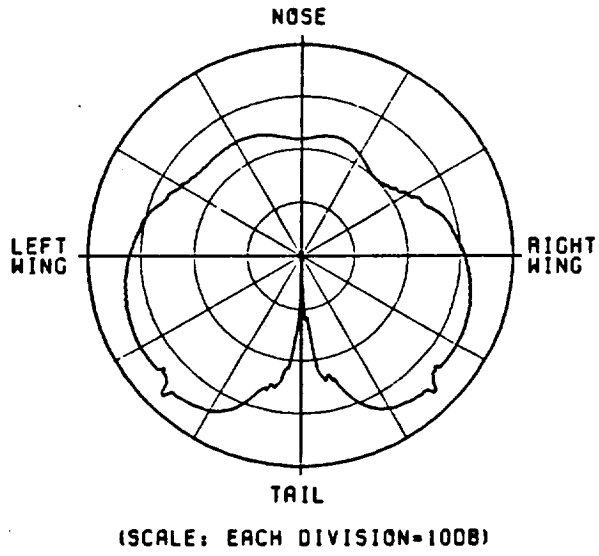

(b) Δ beam

Figure 48. Azimuth pattern at 10° elevation angle with array at position E.

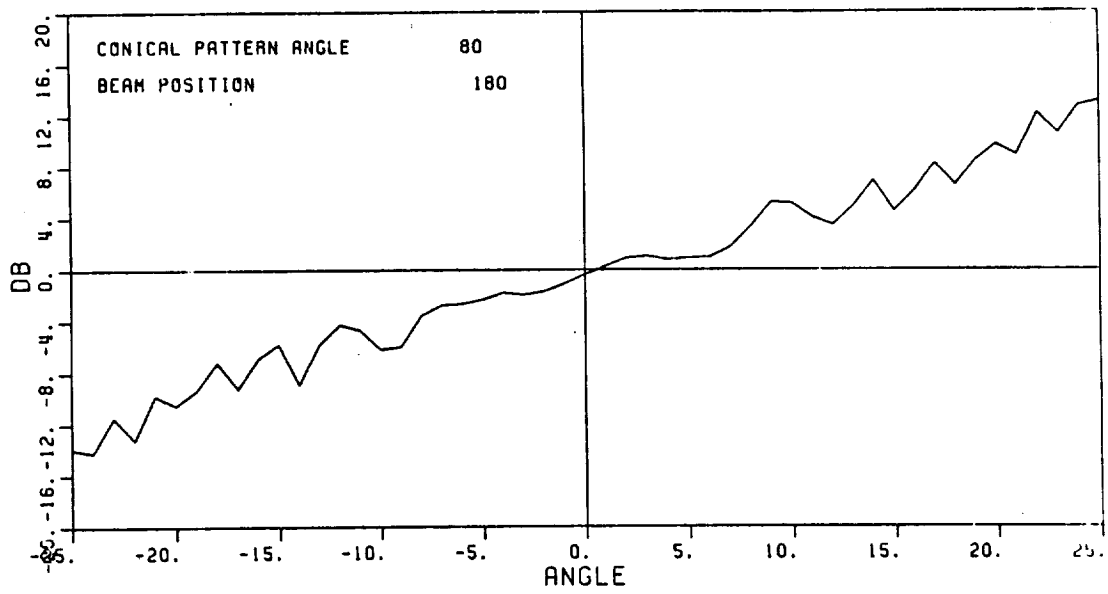

Figure 49. Monopulse characteristic for array at position E. Beams steered toward tail.

In order to determine the effects of fuselage blockage on the Σ and Δ beams at low elevation angles when the beams are steered in the forward direction, it is necessary to simulate the extended nose section of the Boeing 737 aircraft. This is accomplished by adding two plates to the computer model as shown in Figure 50. The aircraft code input data for the two nose plates is given in Appendix B.

Figures 51 through 58 show the Σ and Δ beams and monopulse characteristics for the case in which the TCAS II array is mounted at position A. In Figures 51 through 54, the beams are steered to 0°, 30°, 60° and 90° in azimuth at an elevation angle 10° below the horizon. It is apparent that fuselage blockage is causing a deep null in the patterns in the direction of the nose of the aircraft. This in turn causes distortion in the corresponding monopulse characteristic. This distortion is particularly severe when the beams are directed toward the nose so that the null in the Σ beam caused by fuselage blockage is aligned with the null in the Δ beam. In Figures 55 through 58, the elevation angle of the pattern cut is decreased to 20° below the horizon for azimuth beam positions of 0°, 30°, 60° and 90°. The null caused by fuselage blockage is much deeper at this elevation angle and is responsible for very severe distortion in the monopulse characteristics especially when the beams are steered directly over the nose of the aircraft.

In Figures 59 through 66, the array is mounted at position B. Figures 59 through 62 show the Σ and Δ beam patterns and monopulse characteristics of the TCAS II array when the beams are steered to 0°,

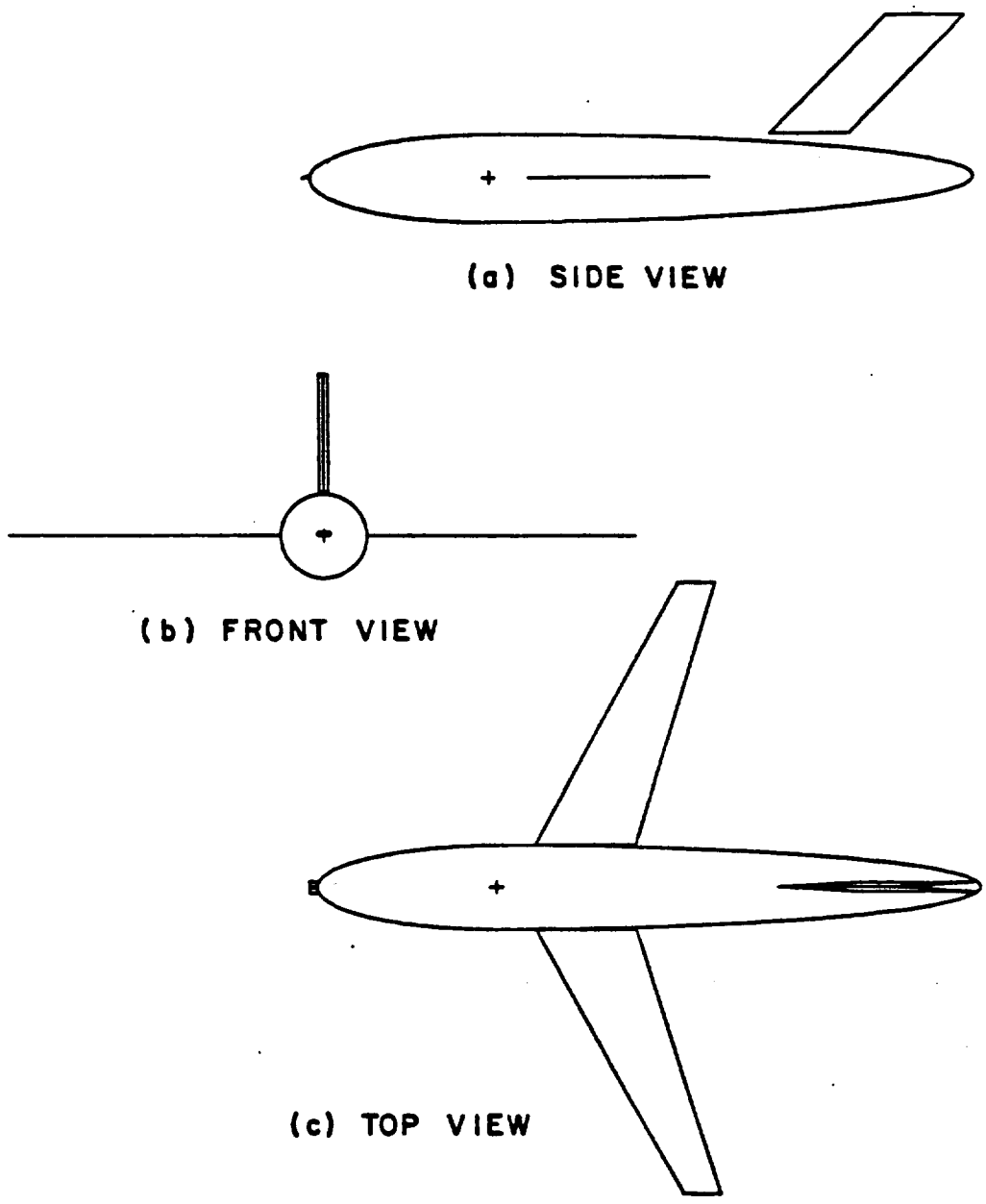

Figure 50. Computer simulated model of a Boeing 737 with two plates added to model the nose of the aircraft.

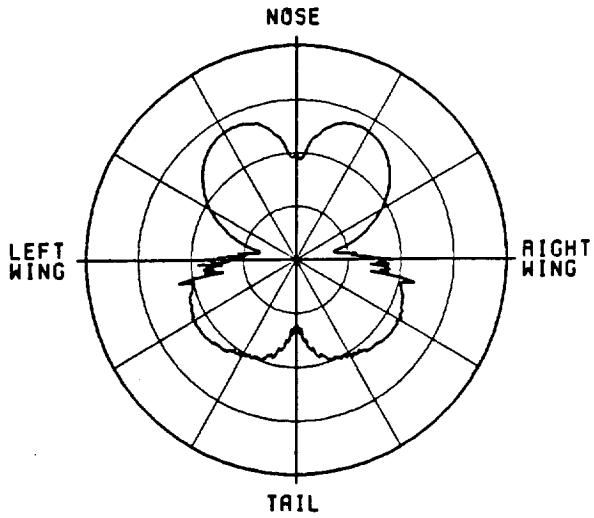

a) Σ beam

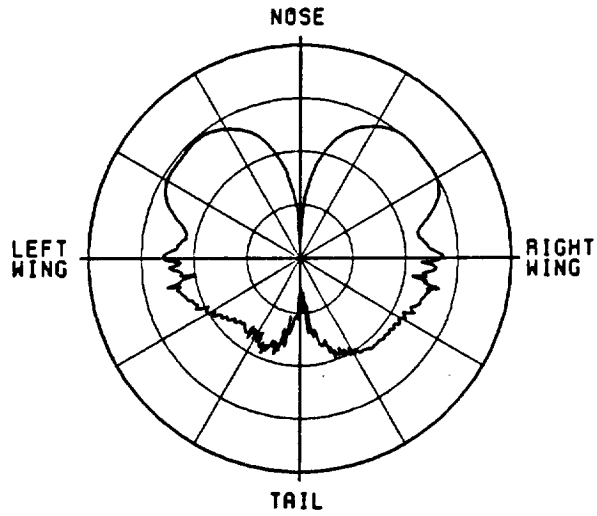

(SCALE: EACH DIVISION=10DB)

b) Δ beam

Figure 51. Azimuth pattern at an elevation angle 10° below the horizon for 0° azimuth beam position. Array at position A.

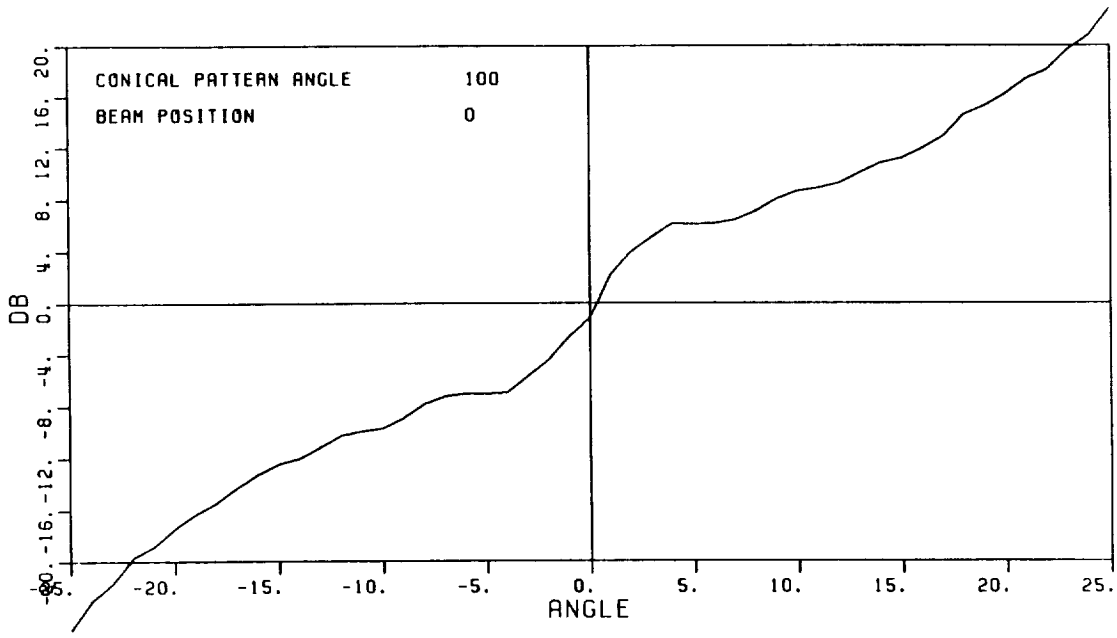

c) Corresponding monopulse characteristic

Figure 51. (Continued).

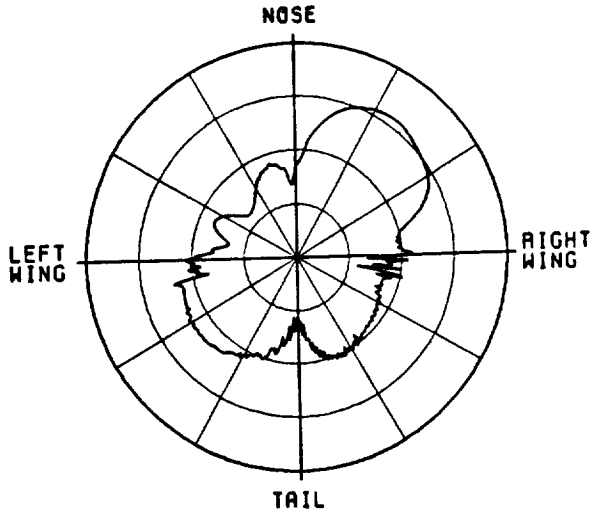

a) Σ beam

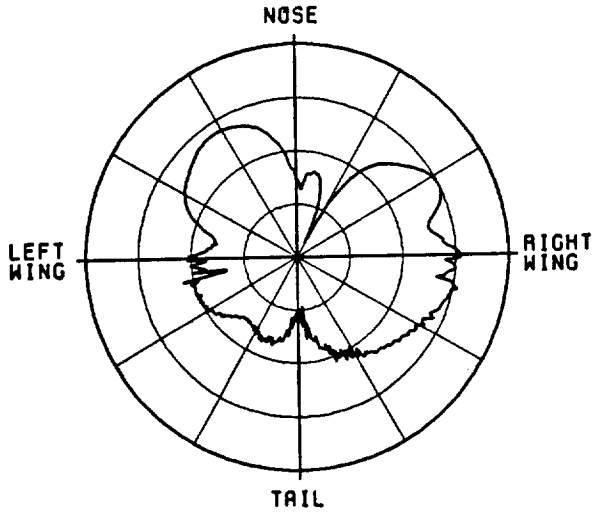

b) Δ beam

Figure 52. Azimuth pattern at an elevation angle 10° below the horizon for 30° azimuth beam position. Array at position A.

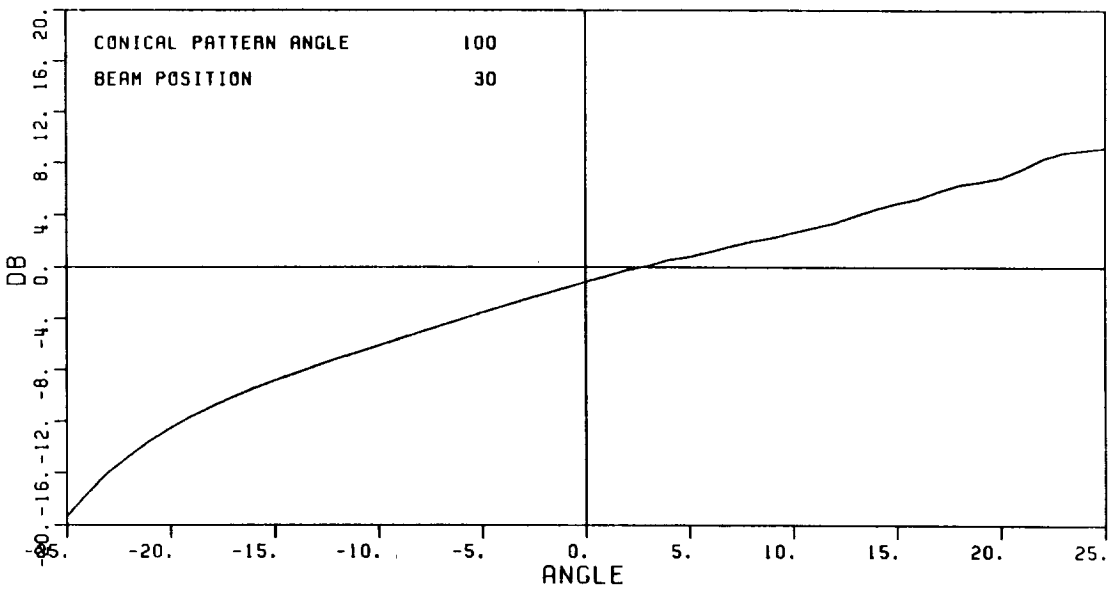

c) Corresponding monopulse characteristic

Figure 52. (Continued).

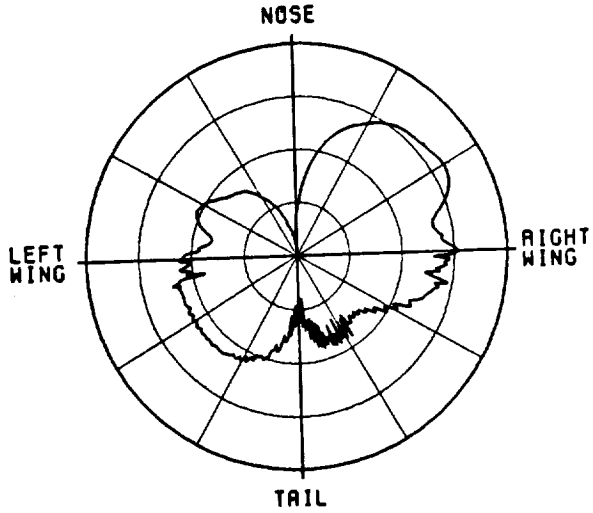

a) Σ beam

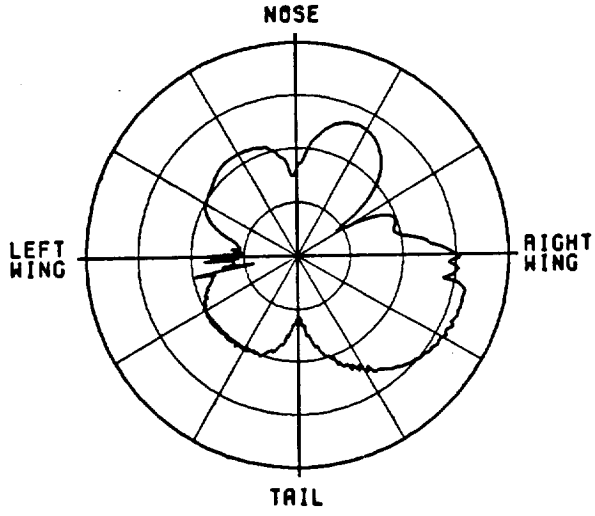

(SCALE: EACH DIVISION=10DB)

b) Δ beam

Figure 53. Azimuth pattern at an elevation angle 10° below the horizon for 60° azimuth beam position. Array at position A.

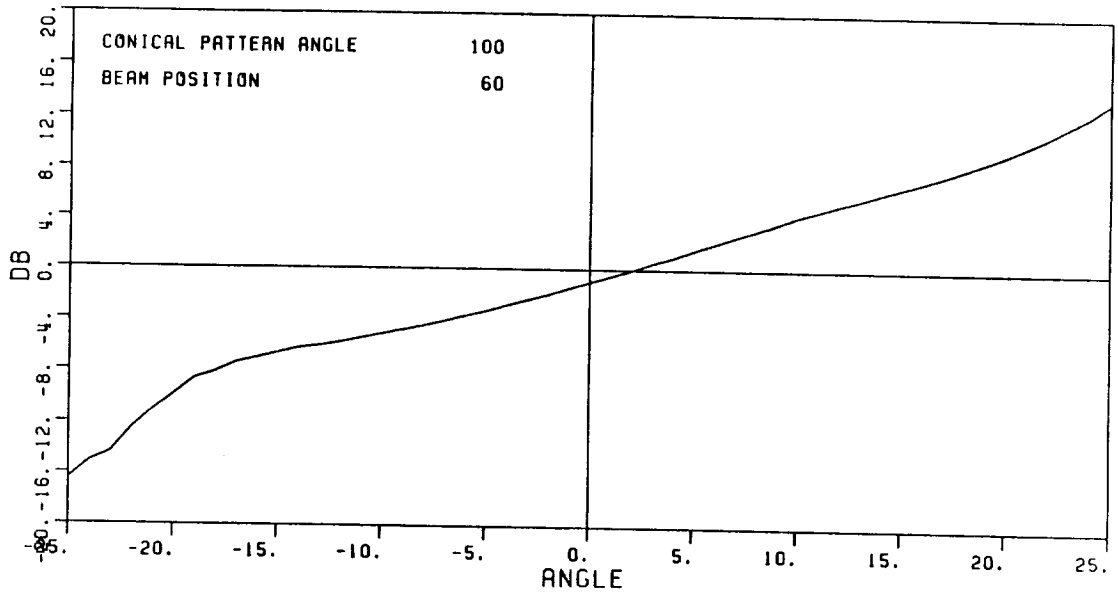

c) Corresponding monopulse characteristic

Figure 53. (Continued).

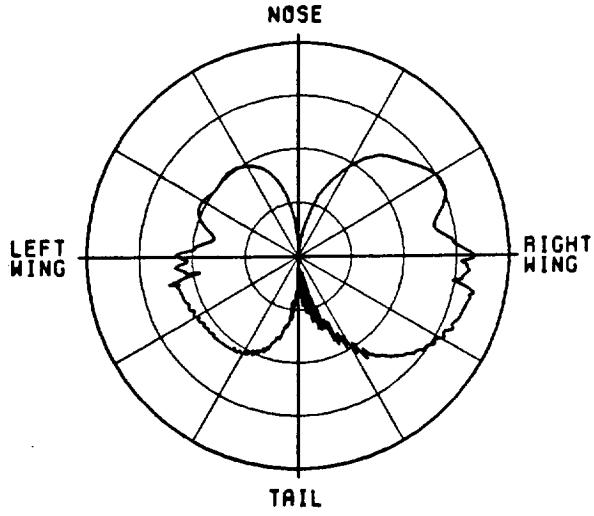

a) Σ beam

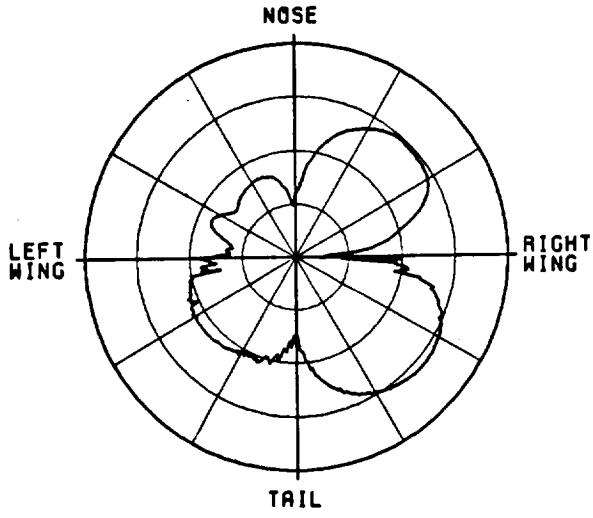

(SCALE: EACH DIVISION=10DB)

b) Δ beam

Figure 54. Azimuth pattern at an elevation angle 10° below the horizon for 90° azimuth beam position. Array at position A.

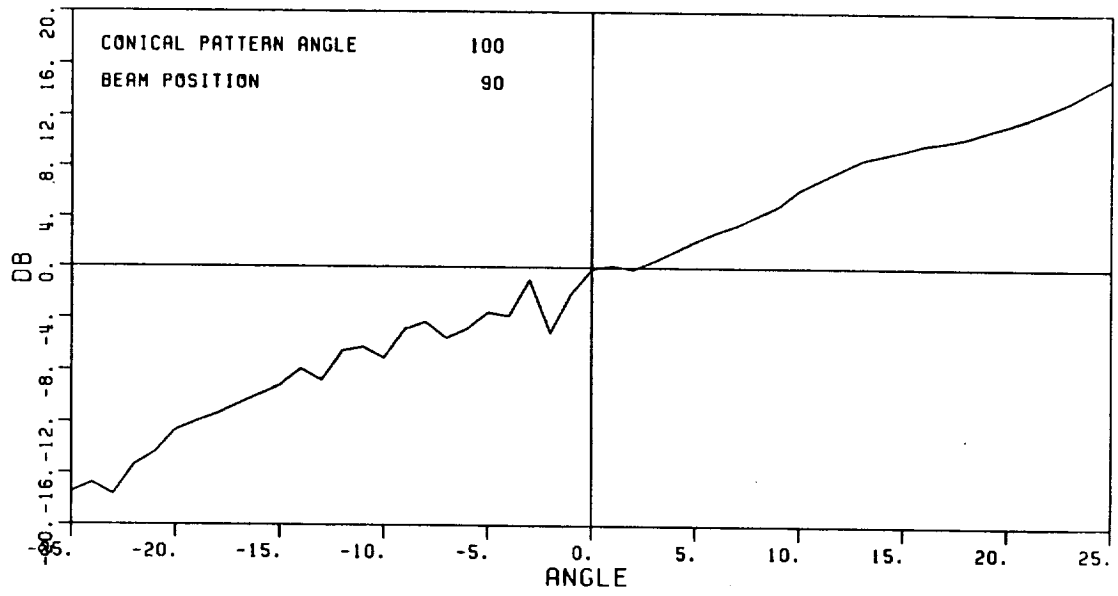

c) Corresponding monopulse characteristic

Figure 54. (Continued).

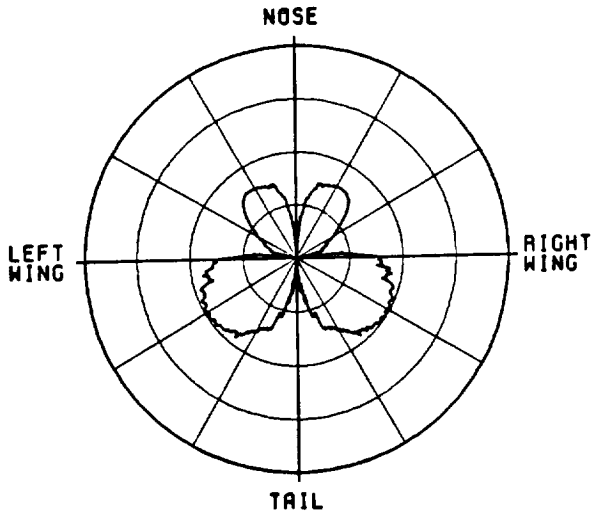

a) Σ beam

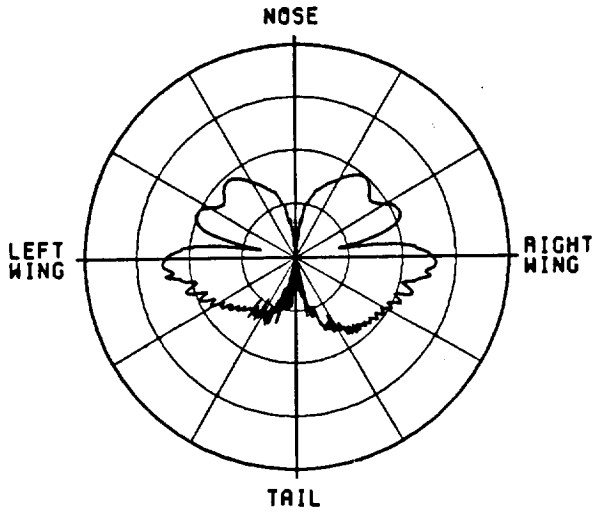

(SCALE: EACH DIVISION=10DB)

b) Δ beam

Figure 55. Azimuth pattern at an elevation angle 20° below the horizon for 0° azimuth beam position. Array at position A.

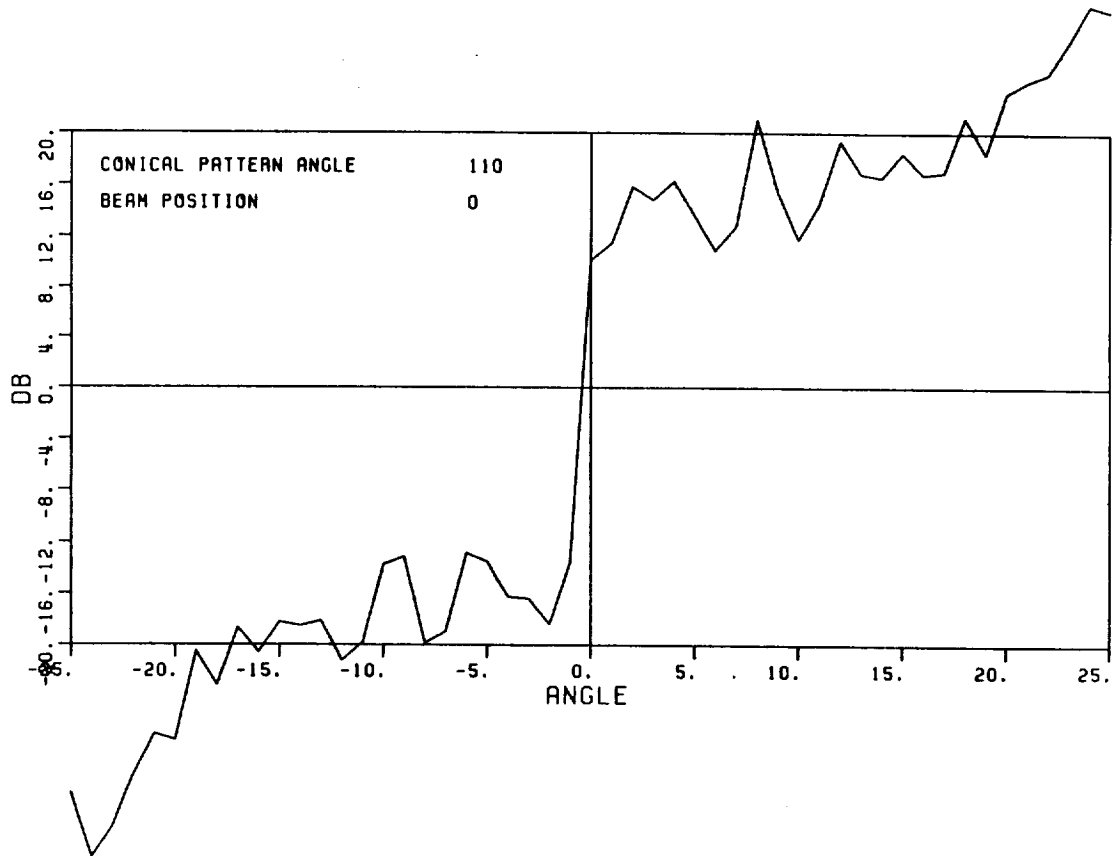

c) Corresponding monopulse characteristic

Figure 55. (Continued).

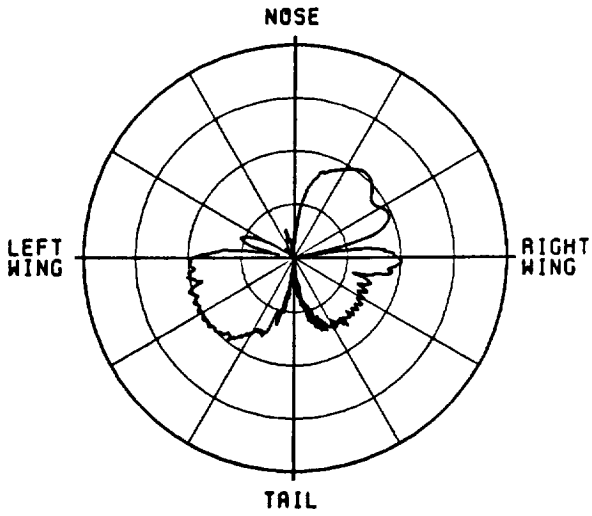

a) Σ beam

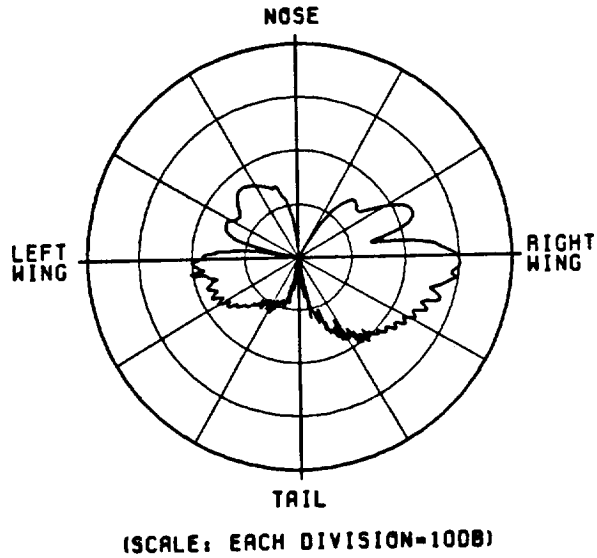

b) Δ beam

Figure 56. Azimuth pattern cut at an elevation angle 20° below the horizon for 30° azimuth beam position. Array at position A.

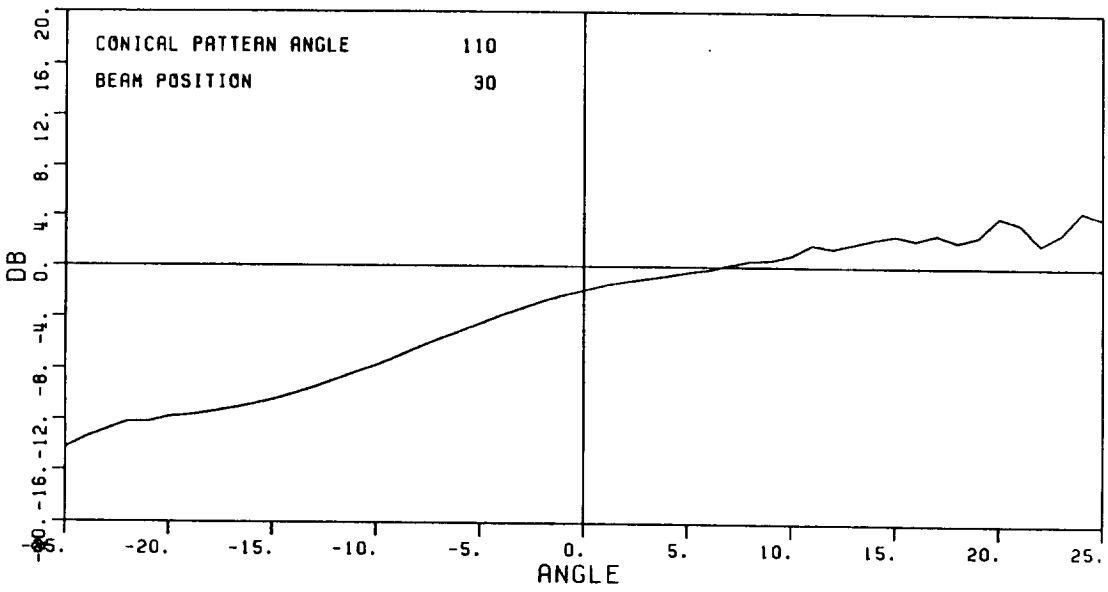

c) Corresponding monopulse characteristic

Figure 56. Continued).

C-2

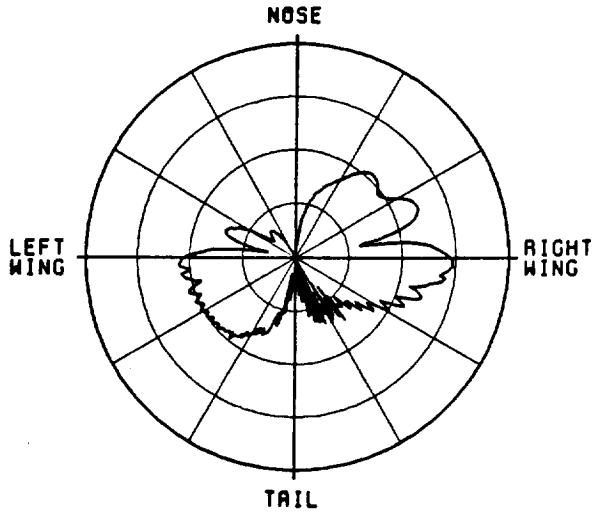

a) Σ beam

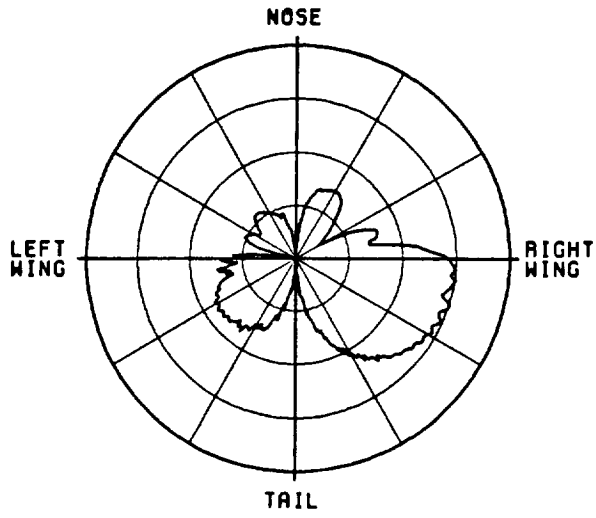

(SCALE: EACH DIVISION=10DB)

b) Δ beam

Figure 57. Azimuth pattern cut an an elevation angle 20° below the horizon for 60° azimuth beam position. Array at position A.

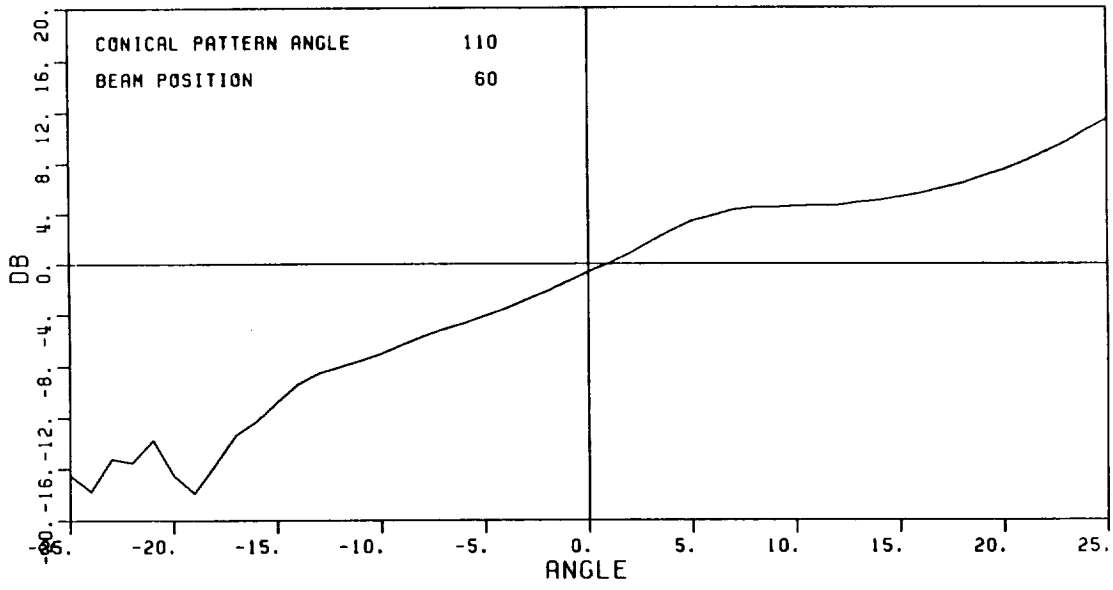

c) Corresponding monopulse characteristic

Figure 57. (Continued).

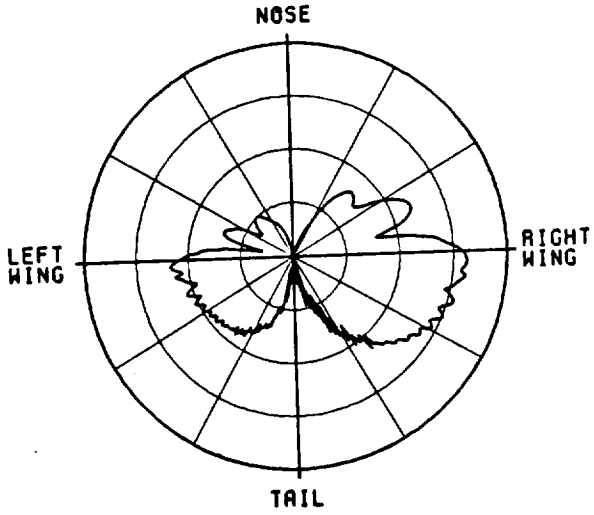

a) Σ beam

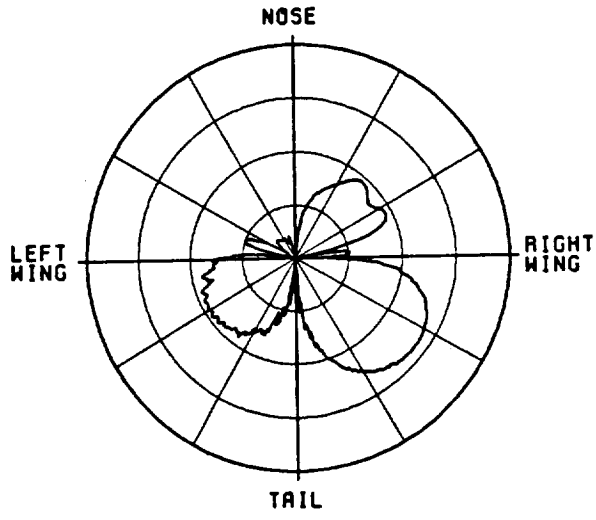

(SCALE: EACH DIVISION=10DB)

b) Δ beam

Figure 58. Azimuth pattern cut at an elevation angle 20° below the horizon for 90° azimuth beam position. Array at position A.

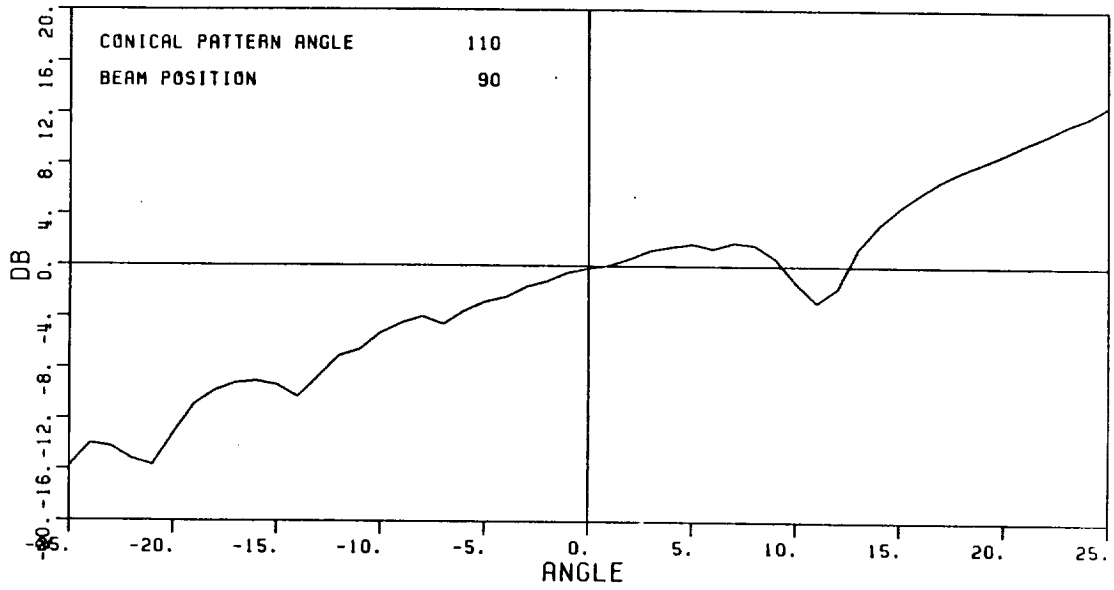

c) Corresponding monopulse characteristic

Figure 58. (Continued).

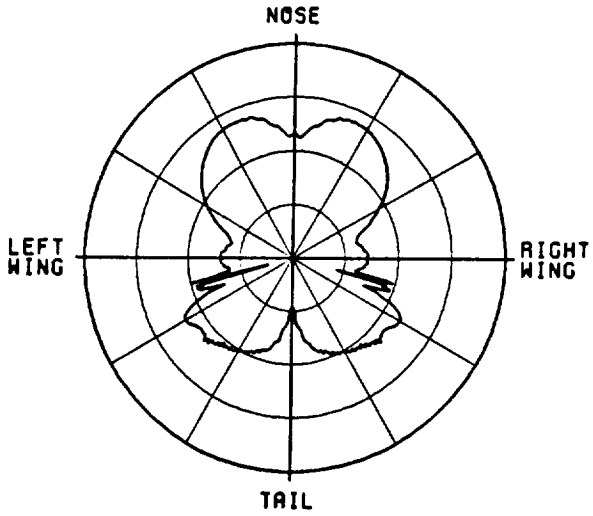

a) Σ beam

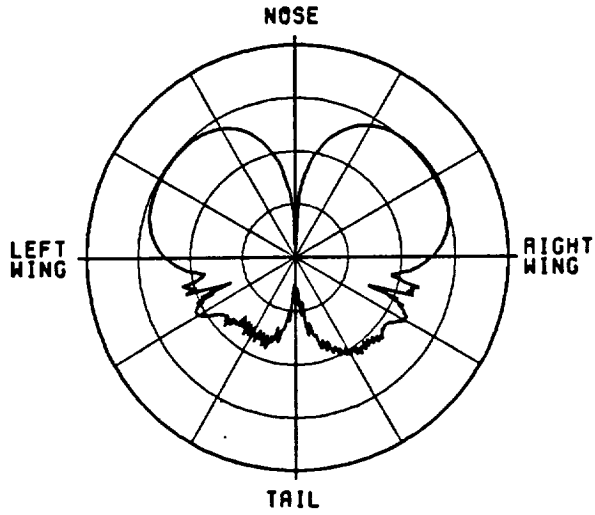

(SCALE: EACH DIVISION=10DB)

b) Δ beam

Figure 59. Azimuth pattern at an elevation angle 10° below the horizon for 0° azimuth beam position. Array at position B.

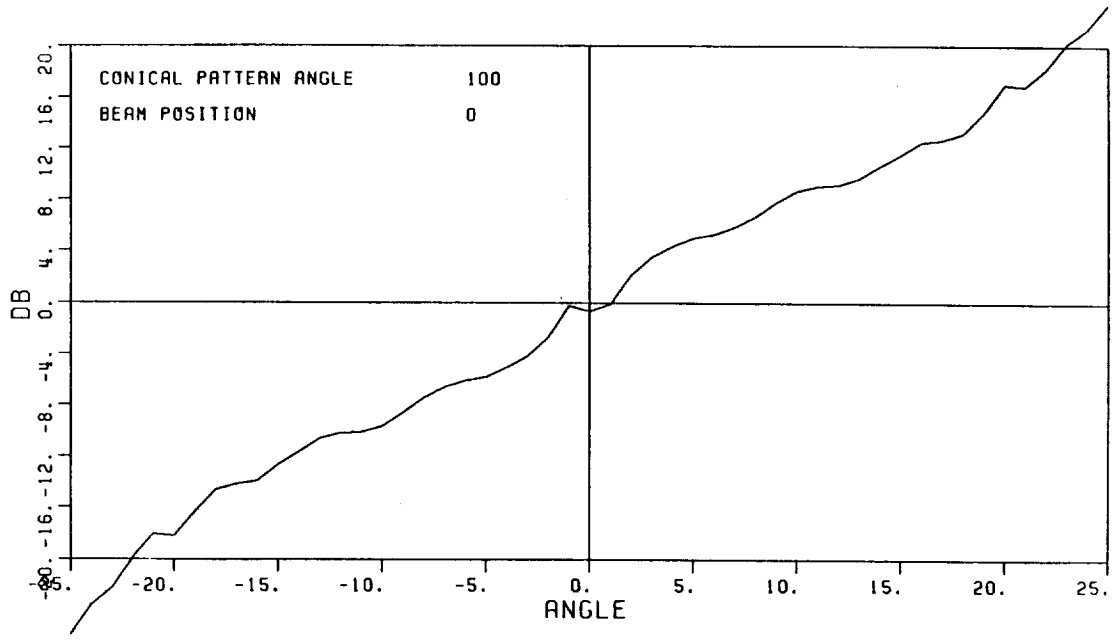

c) Corresponding monopulse characteristic

Figure 59. (Continued).

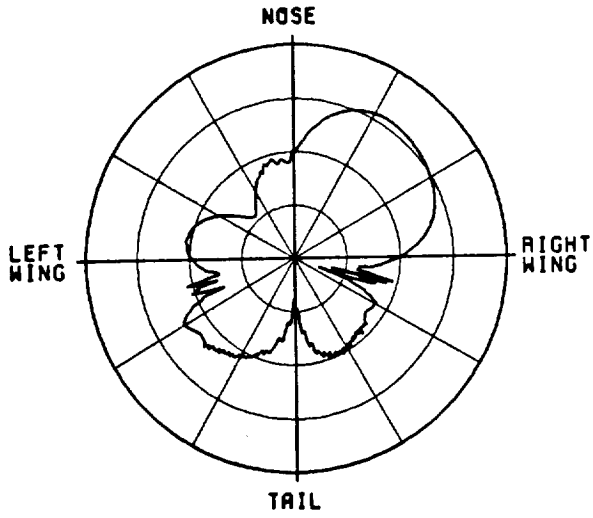

a) Σ beam

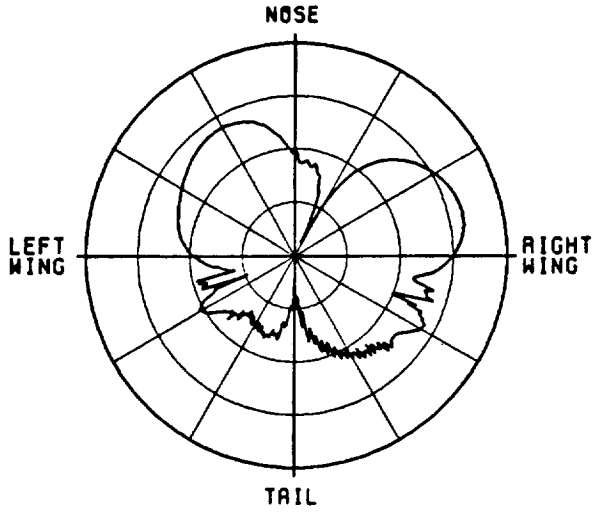

(SCALE: EACH DIVISION=10DB)

b) Δ beam

Figure 60. Azimuth pattern at an elevation angle 10° below the horizon for 30° azimuth beam position. Array at position B.

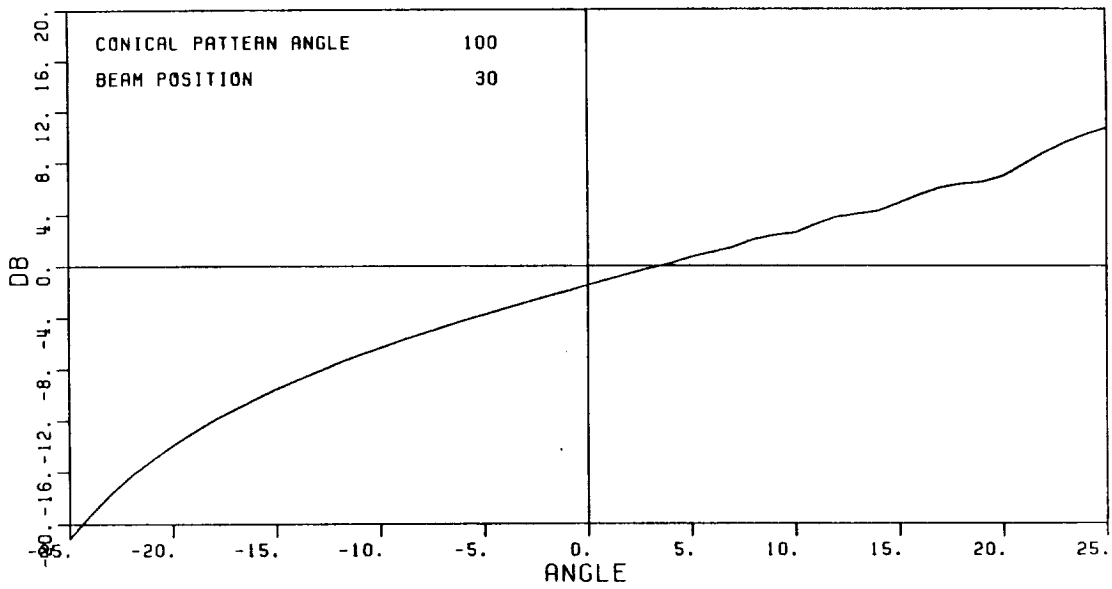

c) Corresponding monopulse characteristic

Figure 60. (Continued).

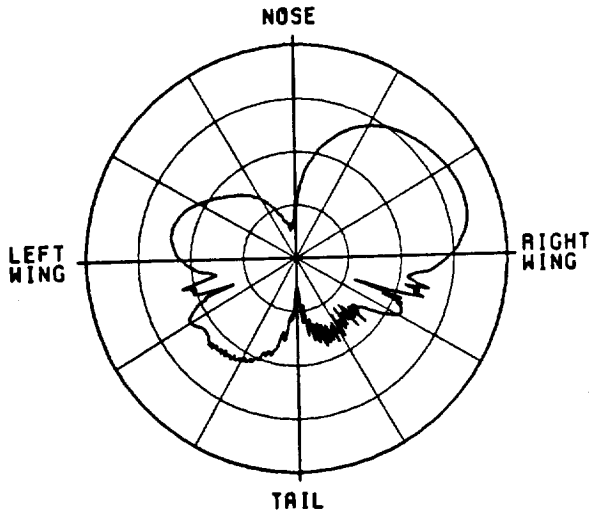

a) Σ beam

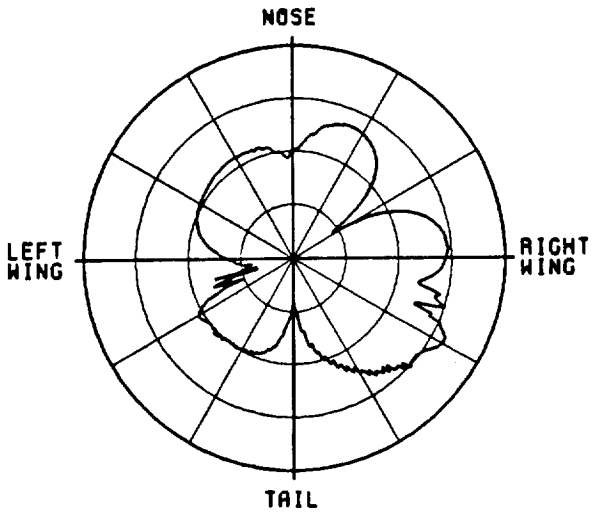

(SCALE: EACH DIVISION=10DB)

b) Δ beam

Figure 61. Azimuth pattern at an elevation angle 10° below the horizon for 60° azimuth beam position. Array at position B.

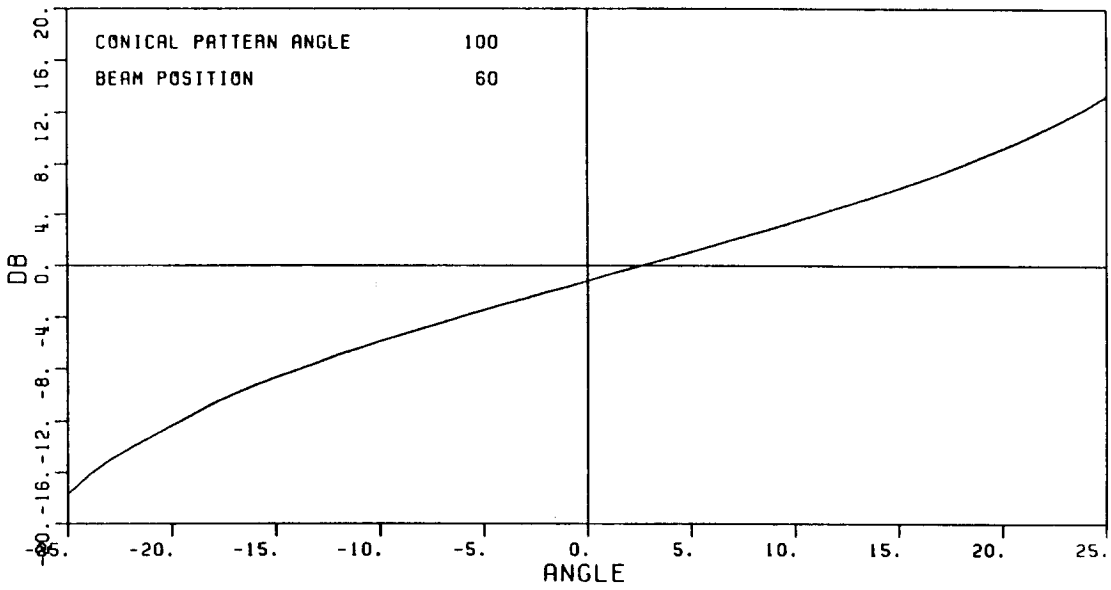

c) Corresponding monopulse characteristic

Figure 61. (Continued).

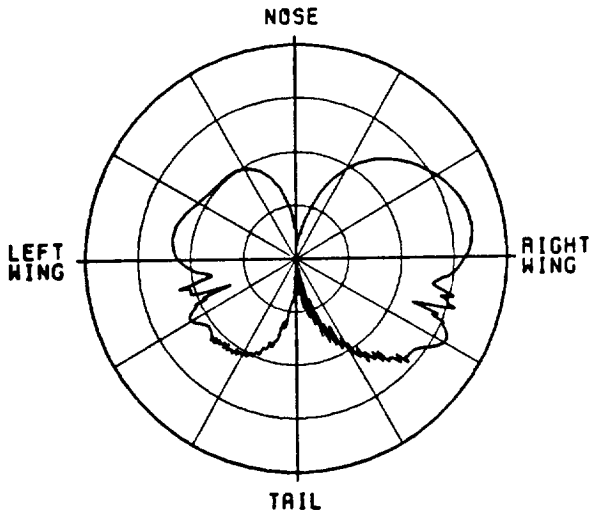

a) Σ beam

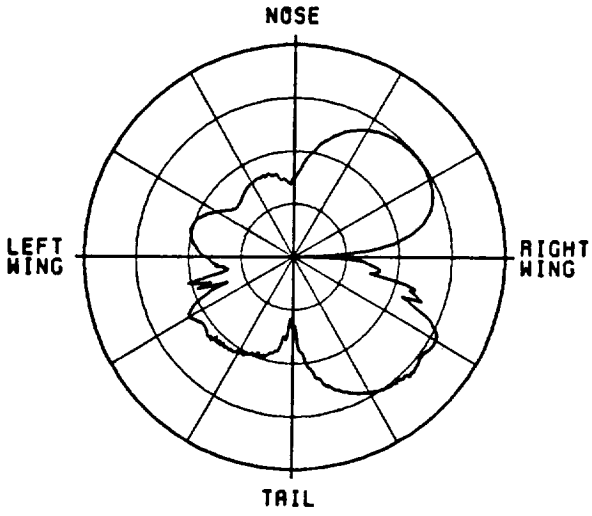

(SCALE: EACH DIVISION=10DB)

b) Δ beam

Figure 62. Azimuth pattern at an elevation angle 10° below the horizon for 90° azimuth beam position. Array at position B.

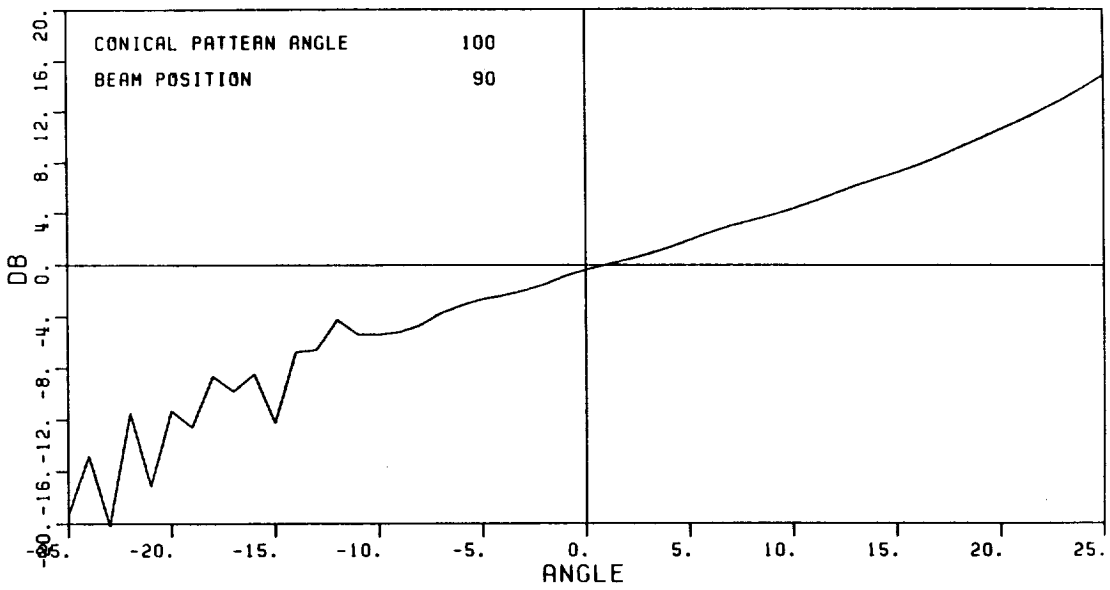

c) Corresponding monopulse characteristic

Figure 62. (Continued).

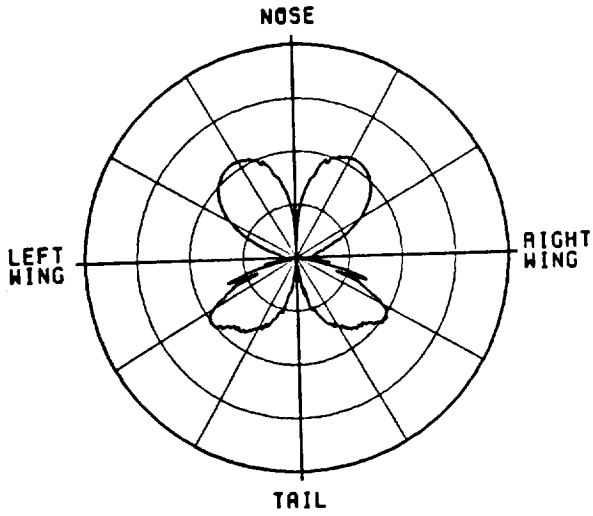

a) Σ beam

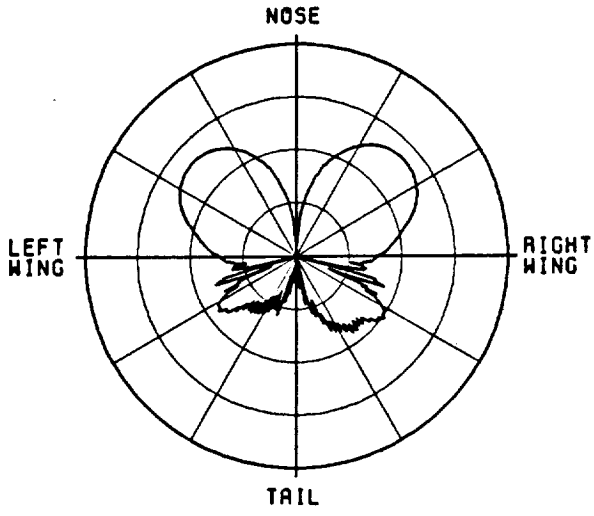

b) Δ beam

Figure 63. Azimuth pattern at an elevation angle 20° below the horizon for 0° azimuth beam position. Array at position B.

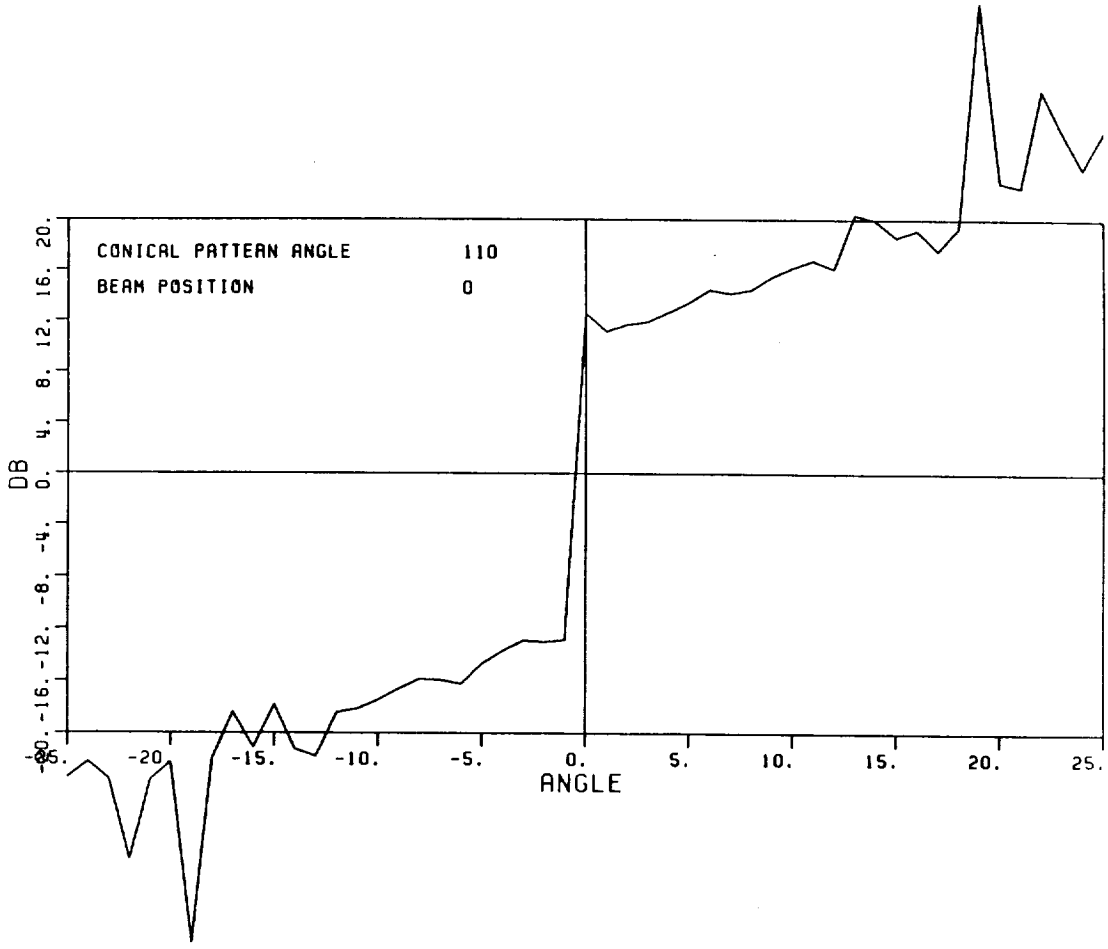

c) Corresponding monopulse characteristic

Figure 63. (Continued).

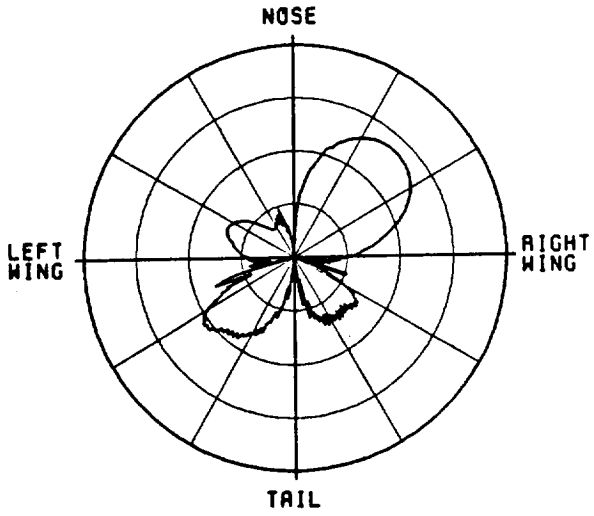

a) Σ beam

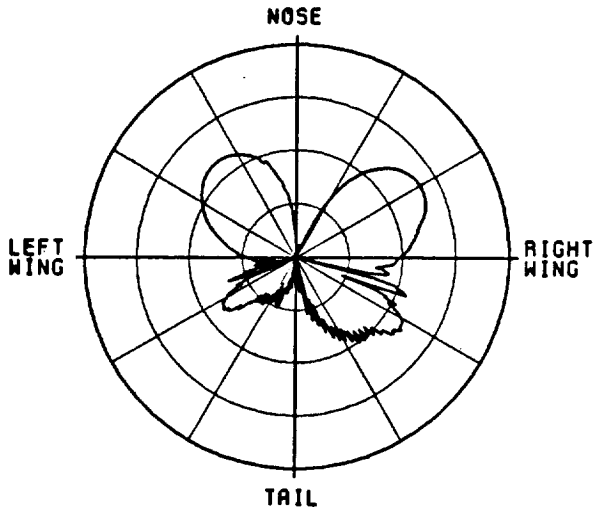

(SCALE: EACH DIVISION=10DB)

b) Δ beam

Figure 64. Azimuth pattern at an elevation angle 20° below the horizon for 30° azimuth beam position. Array at position B.

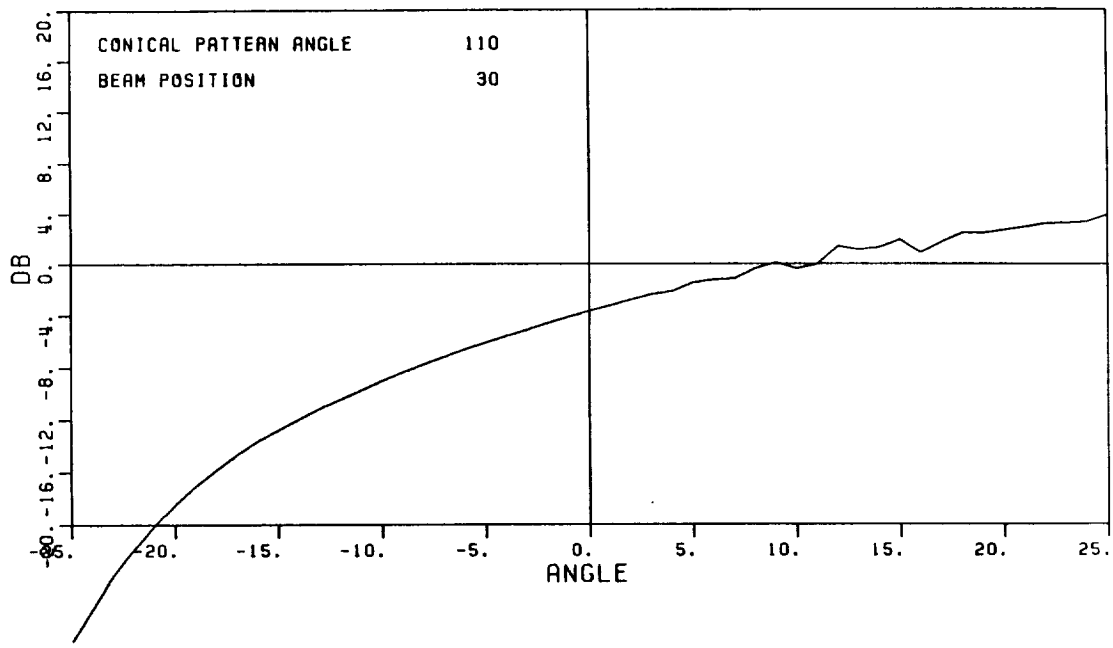

c) Corresponding monopulse characteristic

Figure 64. (Continued).

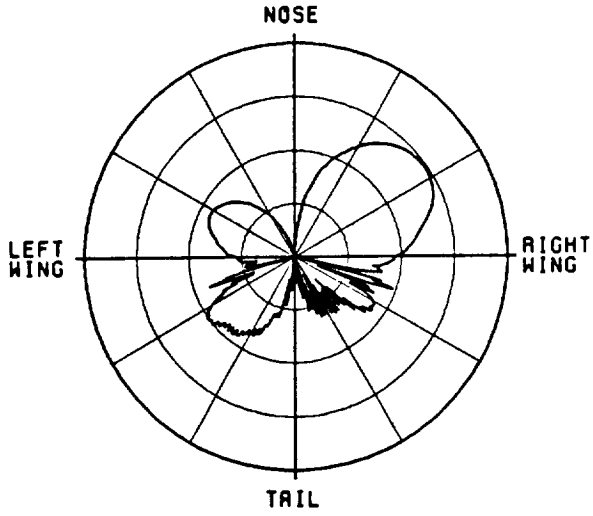

a) Σ beam

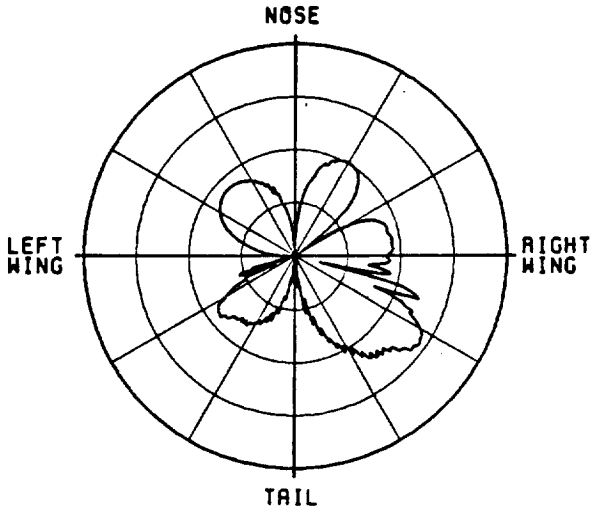

(SCALE: EACH DIVISION=10DB)

b) Δ beam

Figure 65. Azimuth pattern at an elevation angle 20° below the horizon for 60° azimuth beam position. Array at position B.

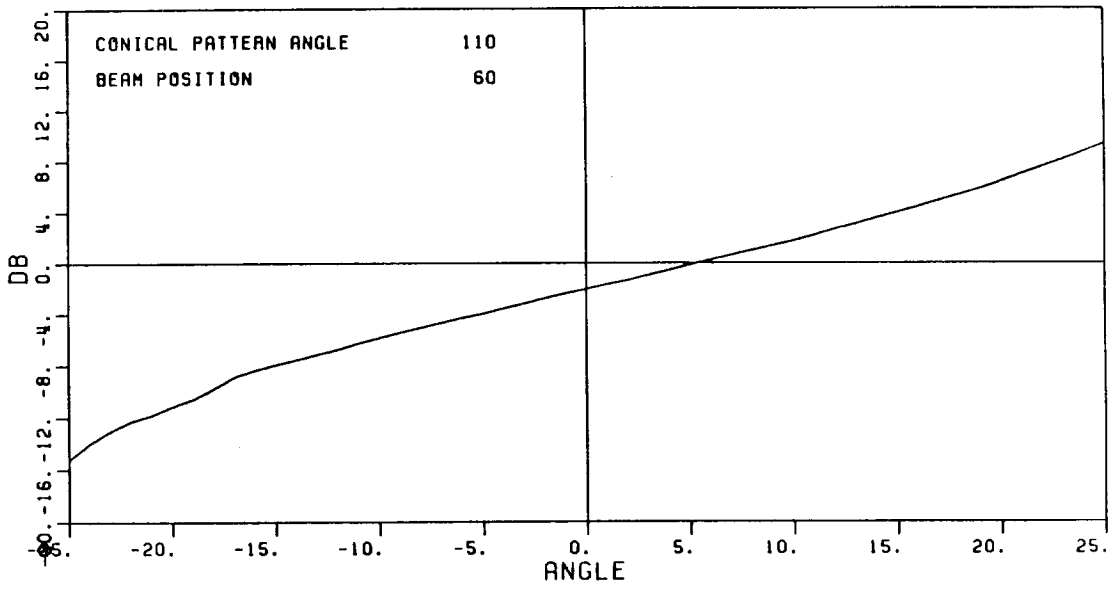

c) Corresponding monopulse characteristic

Figure 65. (Continued).

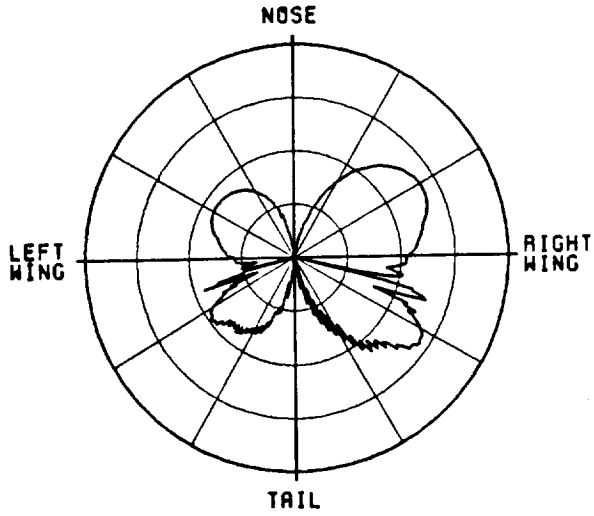

a) Σ beam

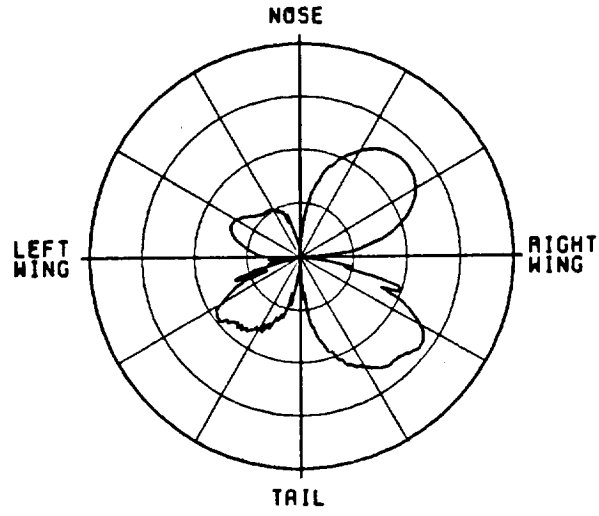

(SCALE: EACH DIVISION=10DB)

b) Δ beam

Figure 66. Azimuth pattern at an elevation angle 20° below the horizon for 90° azimuth beam position. Array at position B.

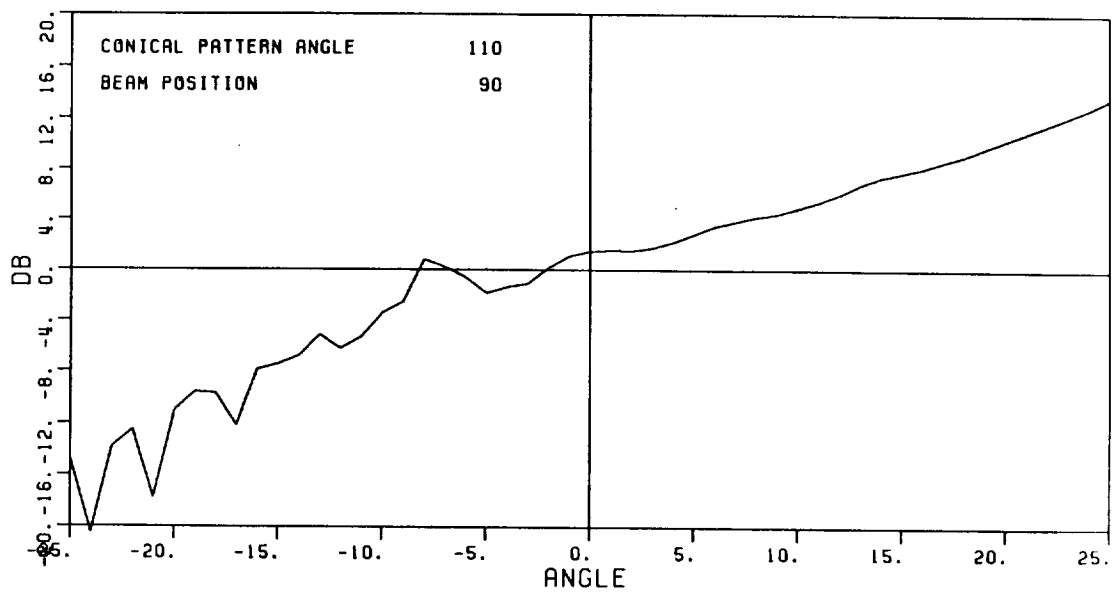

c) Corresponding monopulse characteristic

Figure 66. (Continued).

30°, 60° and 90° in azimuth at an elevation angle 10° below the horizon. The null in the direction of the nose, caused by fuselage blockage, is not as deep at this location as it was for the same pattern cut with the array positioned at location A. The monopulse characteristics show minimal improvement. Figures 63 through 66 represent the Σ and Δ beam patterns and monopulse characteristics at an elevation angle 20° below the horizon. At this elevation angle the fuselage blockage is again responsible for a very deep null in the direction of the nose of the aircraft, and the corresponding monopulse characteristics exhibit a high degree of distortion when the beams are directed toward or near this null.

Figures 67 through 74 show the Σ and Δ beam patterns and monopulse characteristics for the case when the circular array is located at position C. In Figures 67 through 70, the elevation angle of the pattern cut is 10 below the horizon for azimuth beam positions of 0°, 30°, 60° and 90°. The null in the direction of the nose of the aircraft is much less severe than those appearing in the patterns of the previous two array locations. This leads to substantial improvement in the corresponding monopulse characteristics at all four of the azimuth beam positions considered here. The elevation angle is decreased to 20° below the horizon in Figures 71 through 74. The null caused by fuselage blockage is still quite deep at this array location and elevation angle, but it does show improvement over the preceeding two cases for the same pattern cut. The corresponding monopulse characteristics exhibit similar improvement.

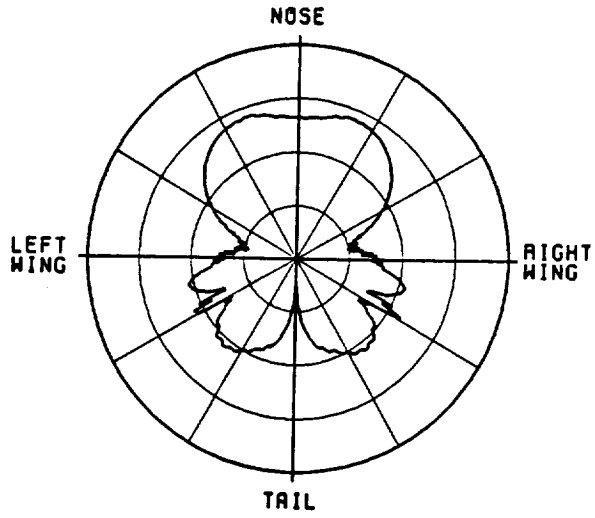

a) Σ beam

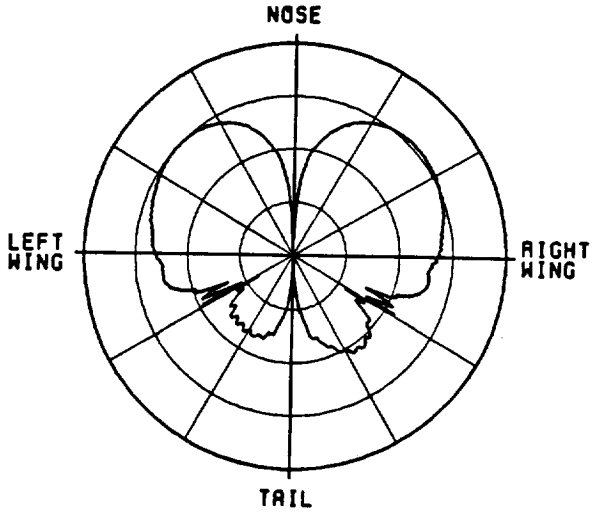

b) Δ beam

Figure 67. Azimuth pattern at an elevation angle 10° below the horizon for 0° azimuth beam position. Array at position C.

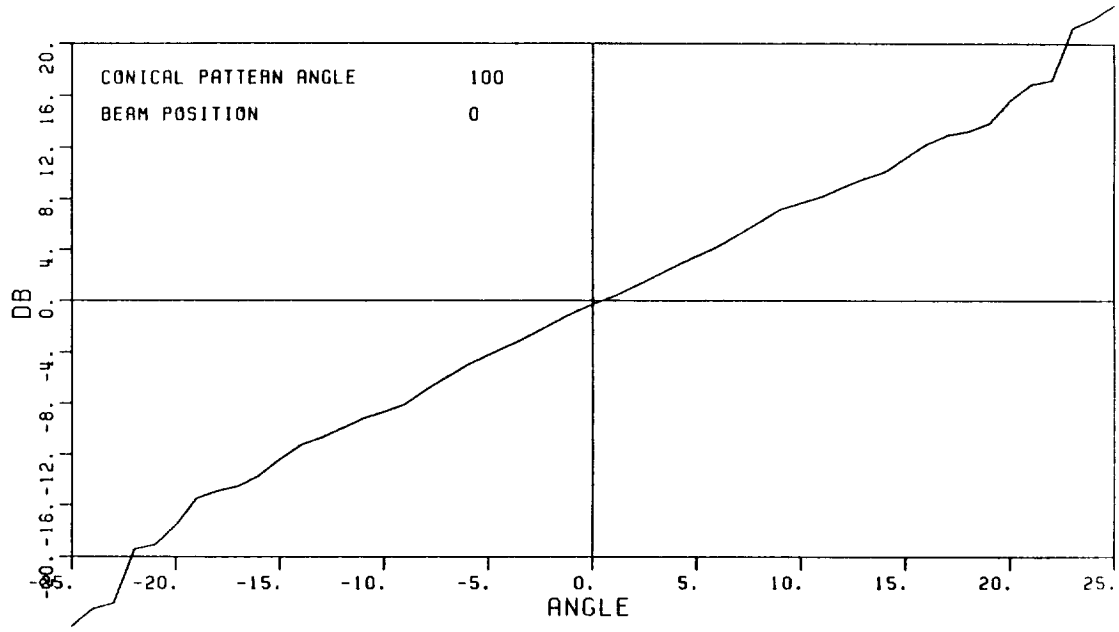

c) Corresponding monopulse characteristic

Figure 67. (Continued).

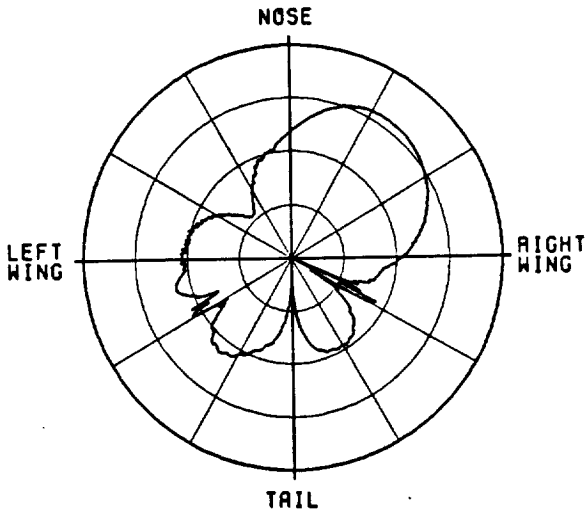

a) Σ beam

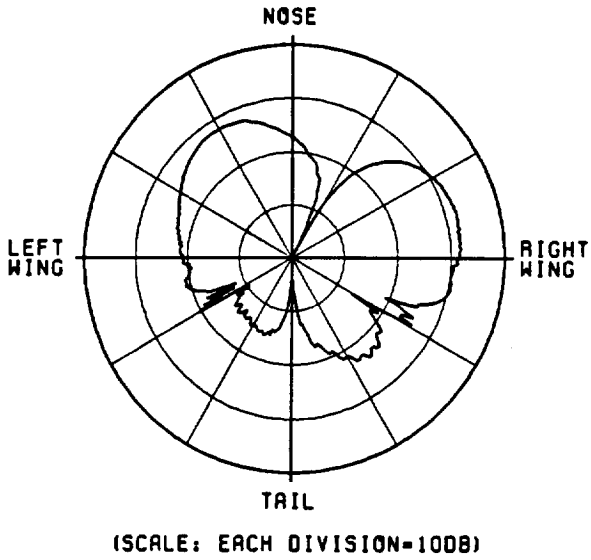

b) Δ beam

Figure 68. Azimuth pattern at an elevation angle 10° below the horizon for 30° azimuth beam position. Array at position C.

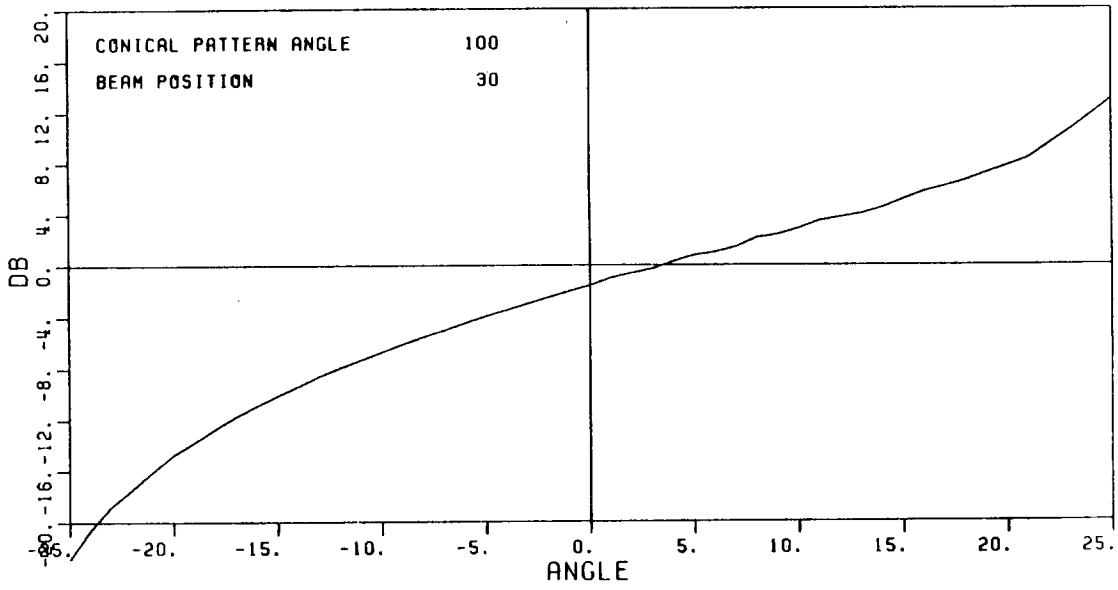

c) Corresponding monopulse characteristic

Figure 68. (Continued).

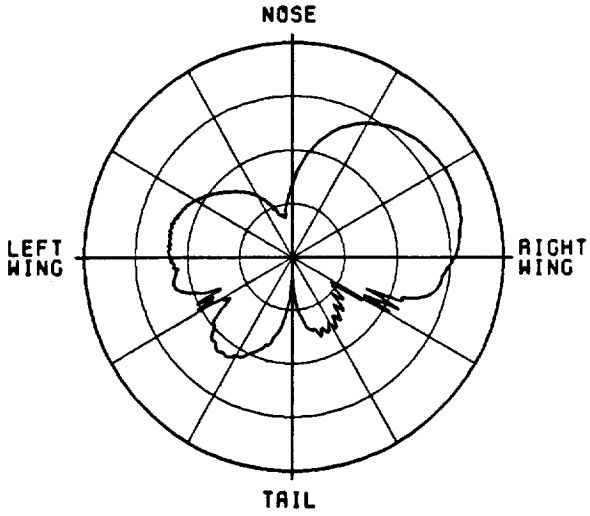

a) Σ beam

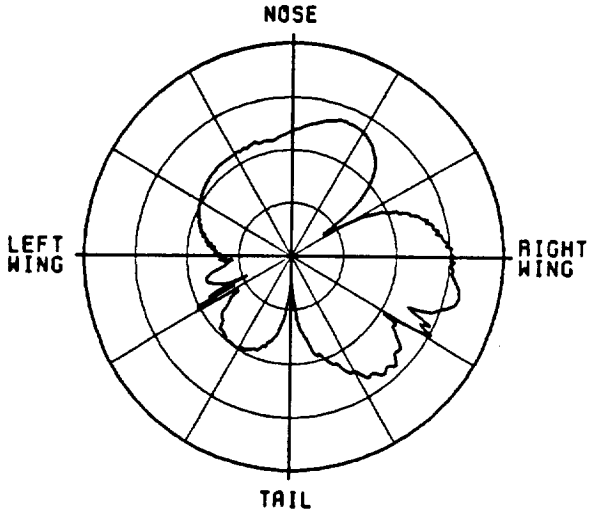

(SCALE: EACH DIVISION=10DB)

b) Δ beam

Figure 69. Azimuth pattern at an elevation angle 10° below the horizon for 60° azimuth beam position. Array at position C.

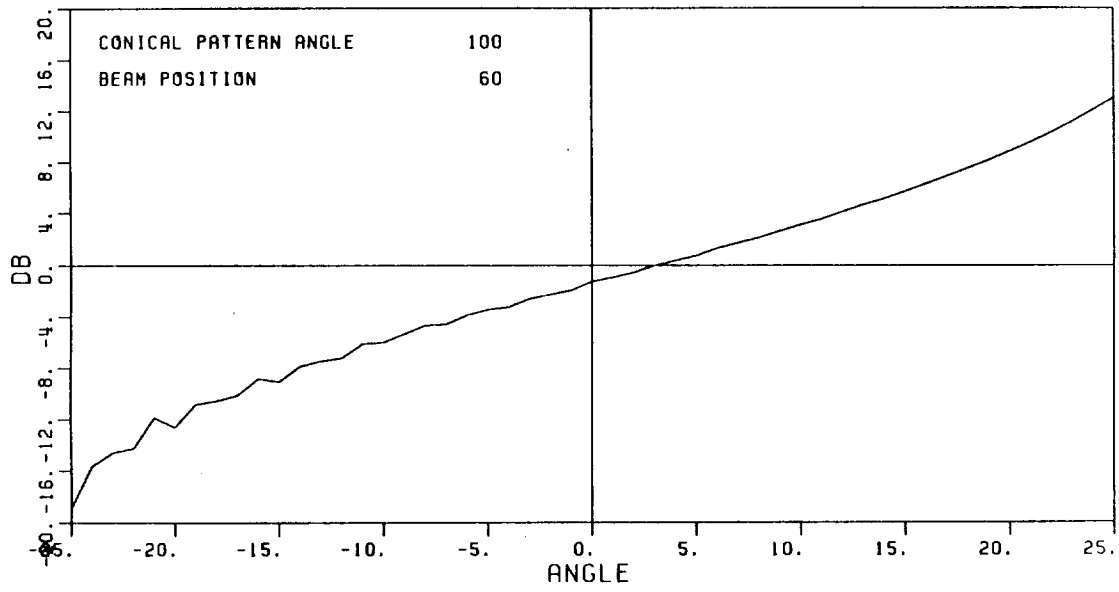

c) Corresponding monopulse characteristic

Figure 69. (Continued).

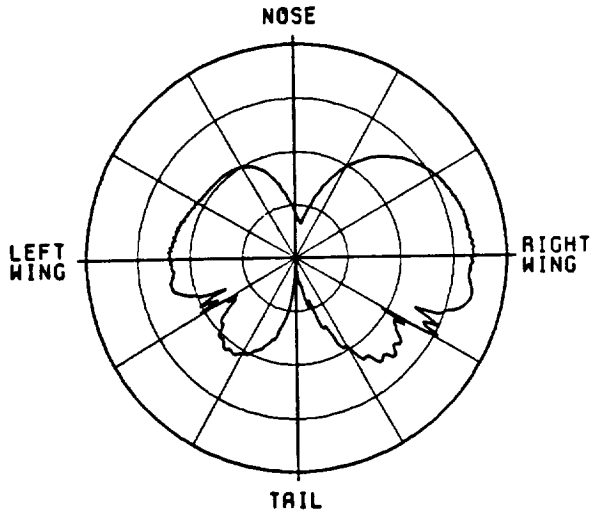

a) Σ beam

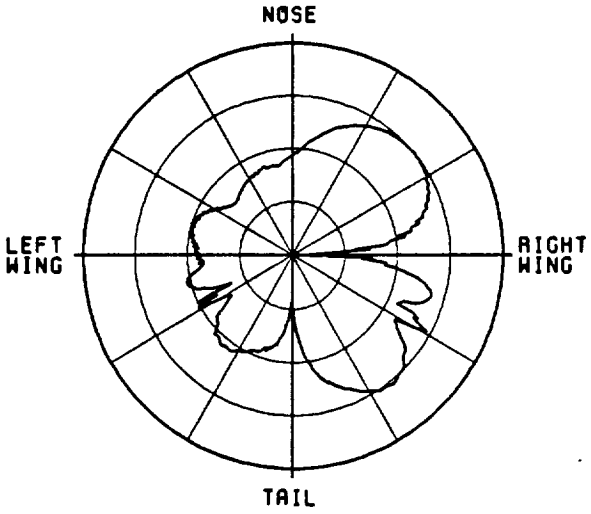

(SCALE: EACH DIVISION=10DB)

b) Δ beam

Figure 70. Azimuth pattern at an elevation angle 10° below the horizon for 90° azimuth beam position. Array at position C.

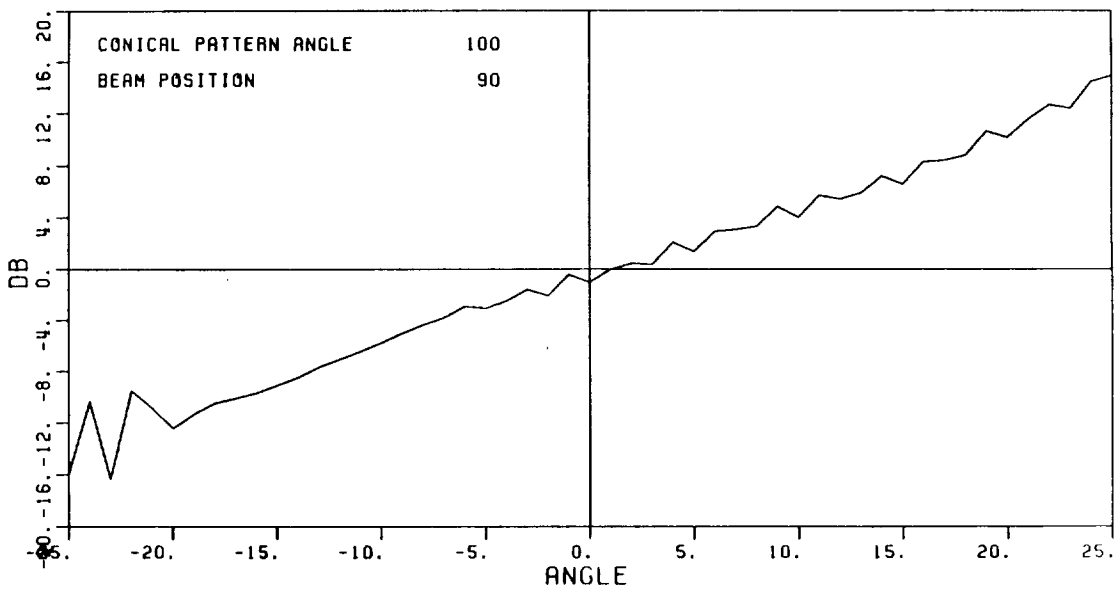

c) Corresponding monopulse characteristic

Figure 70. (Continued).

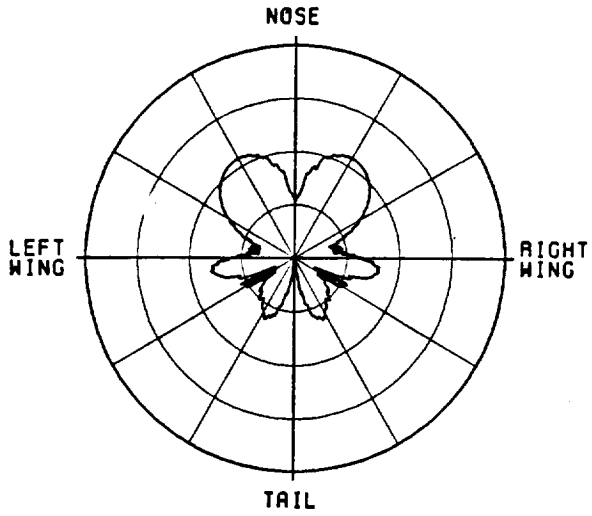

a) Σ beam

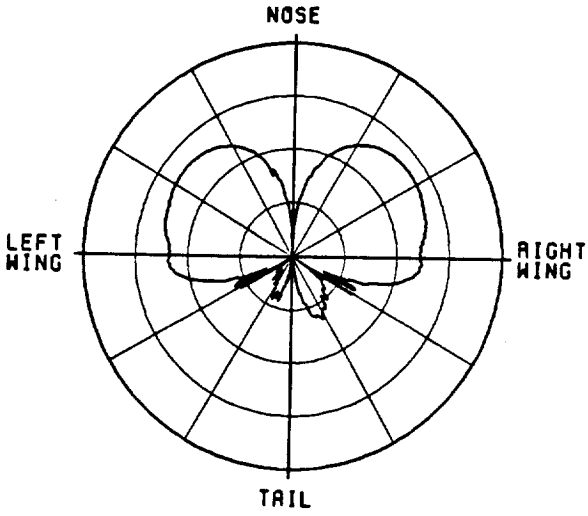

(SCALE: EACH DIVISION=10DB)

b) Δ beam

Figure 71. Azimuth pattern at an elevation angle 20° below the horizon for 0° azimuth beam position. Array at position C.

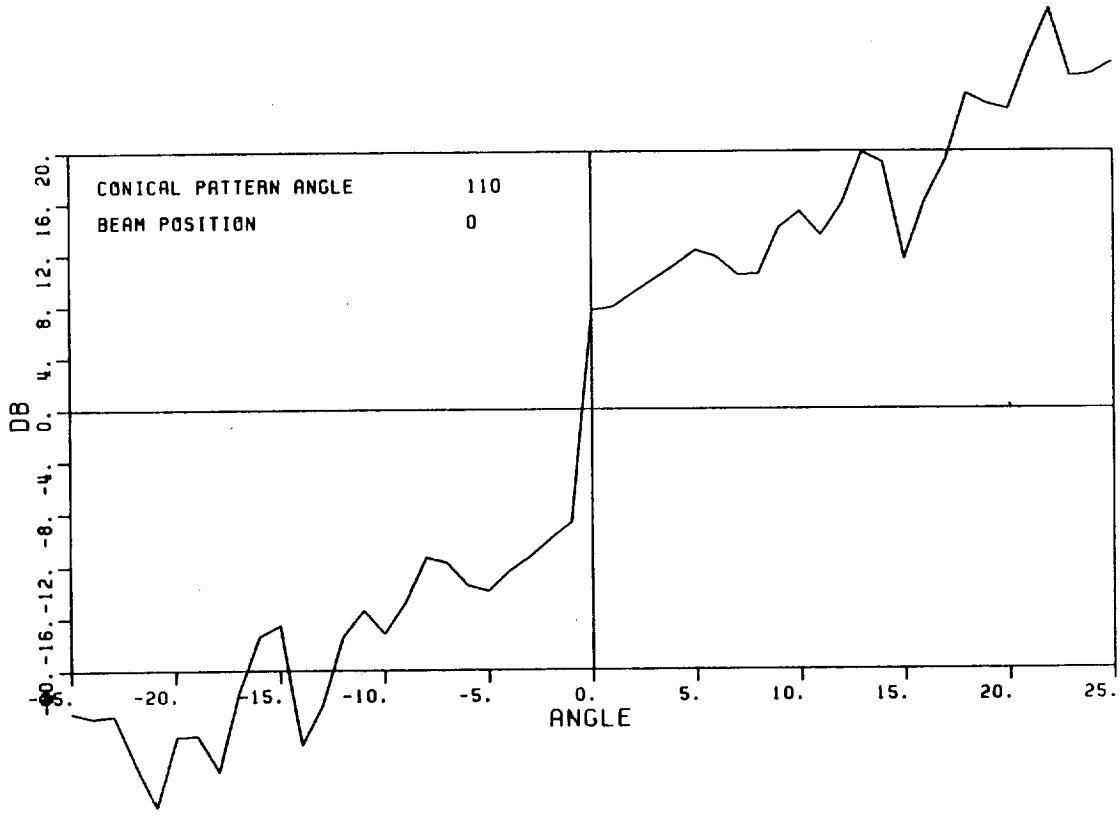

c) Corresponding monopulse characteristic

Figure 71. (Continued).

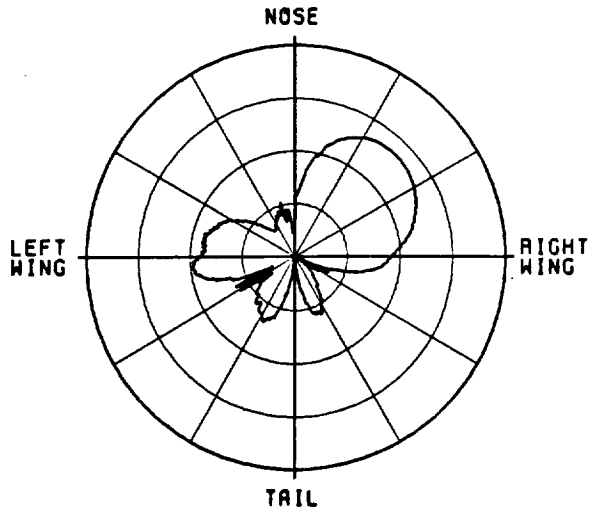

a) Σ beam

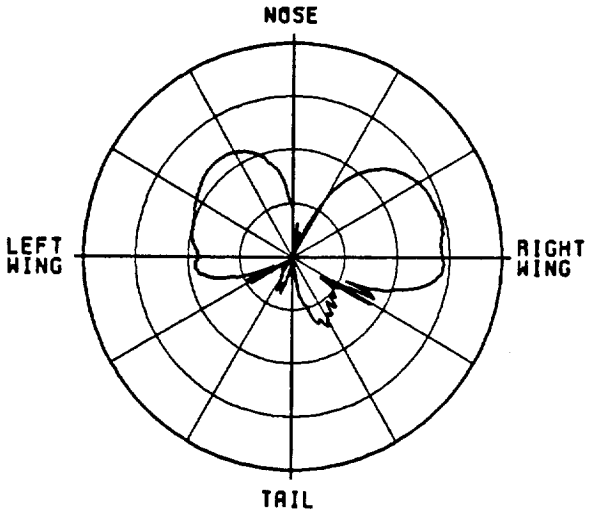

(SCALE: EACH DIVISION=10DB)

b) Δ beam

Figure 72. Azimuth pattern at an elevation angle 20° below the horizon for 30° azimuth beam position. Array at position C.

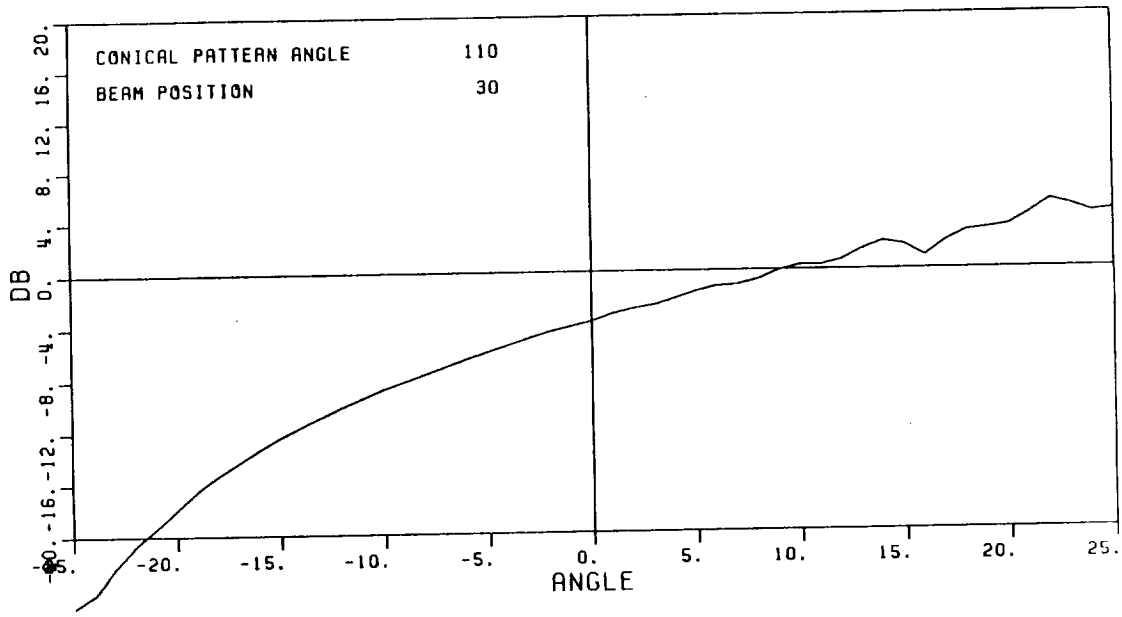

c) Corresponding monopulse characteristic

Figure 72. (Continued).

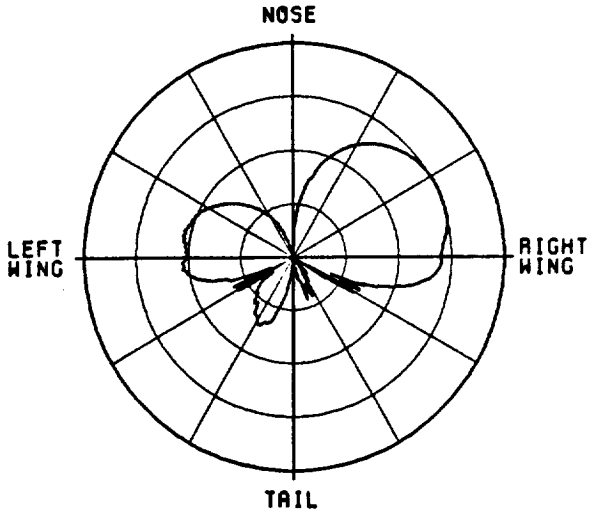

a) Σ beam

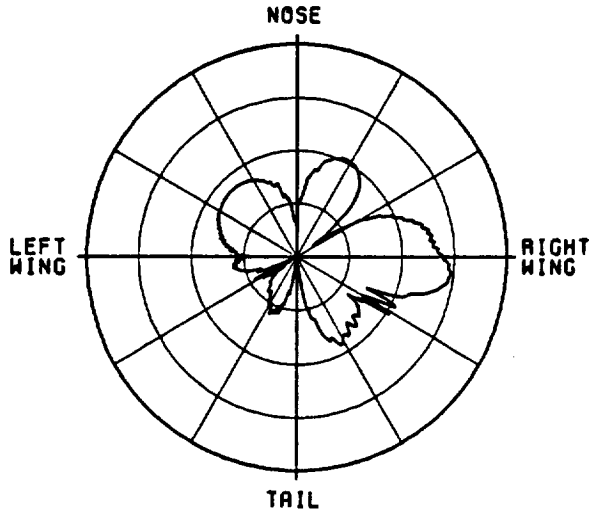

(SCALE: EACH DIVISION=10DB)

b) Δ beam

Figure 73. Azimuth pattern at an elevation angle 20° below the horizon for 60° azimuth beam position. Array at position C.

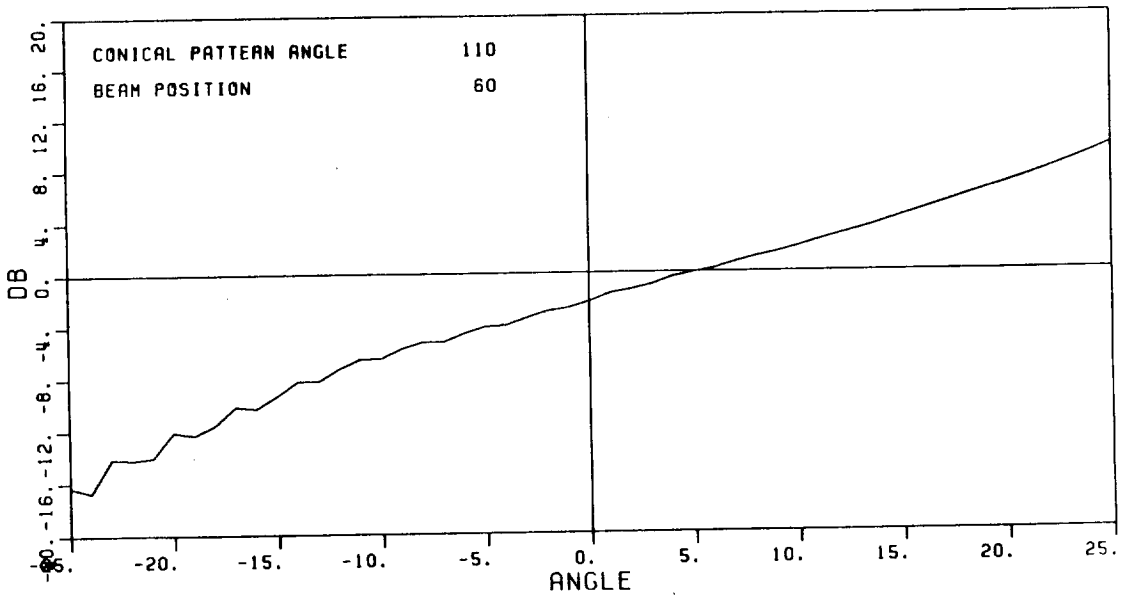

c) Corresponding monopulse characteristic

Figure 73. (Continued).

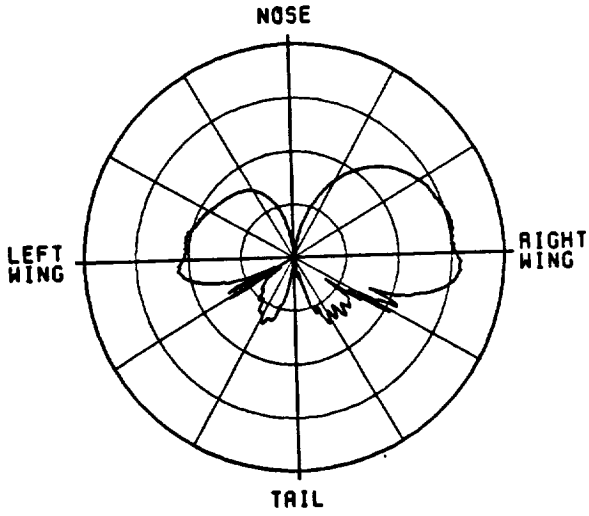

a) Σ beam

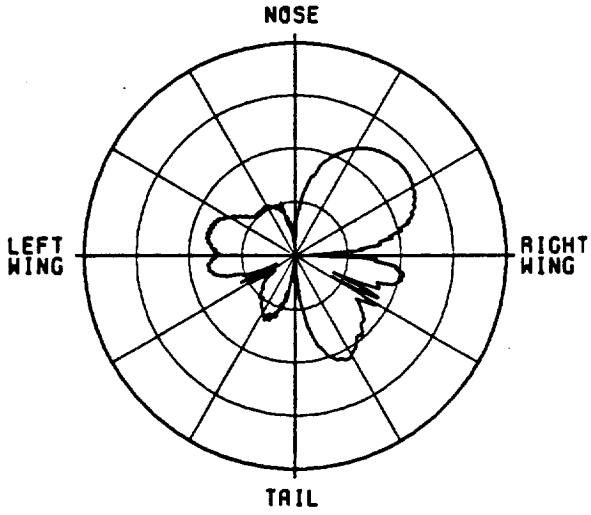

(SCALE: EACH DIVISION=10DB)

b) Δ beam

Figure 74. Azimuth pattern at an elevation angle 20° below the horizon for 90° azimuth beam position. Array at position C.

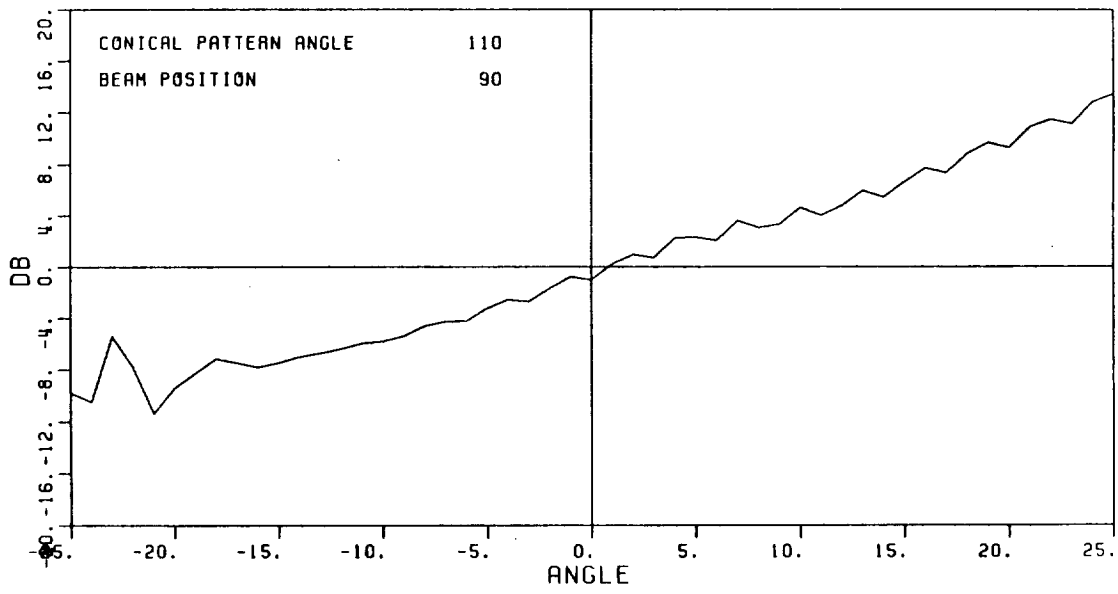

c) Corresponding monopulse characteristic

Figure 74. (Continued).

Figures 75 through 82 show the Σ and Δ beam patterns at azimuth beam positions of 0°, 30°, 60° and 90° at elevation angles 10° and 20° below the horizon for the case where the array is located at position D. At the 10° elevation angle, the null in the direction of the nose of the aircraft, which appeared in all previous cases, is no longer present. When the elevation angle is decreased to 20° below the horizon a small null appears in the direction of the nose. All of the corresponding monopulse characteristics show improvement.

Figures 83 through 90 represent the Σ and Δ beam patterns and monopulse characteristics for azimuth beam positions of 0°, 30°, 60° and 90° at elevation angles 10° and 20° below the horizon for the array located at position E. In this case, at both elevation angles, there are no noticeable nulls in the patterns in the direction of the nose of the aircraft. The patterns are no longer blocked by the fuselage in this direction. In addition, because the array is well removed from the scattering structures when mounted at this location their effect on the beam patterns is small. The corresponding monopulse characteristics, at all four azimuth beam positions considered in this case, show very little distortion.

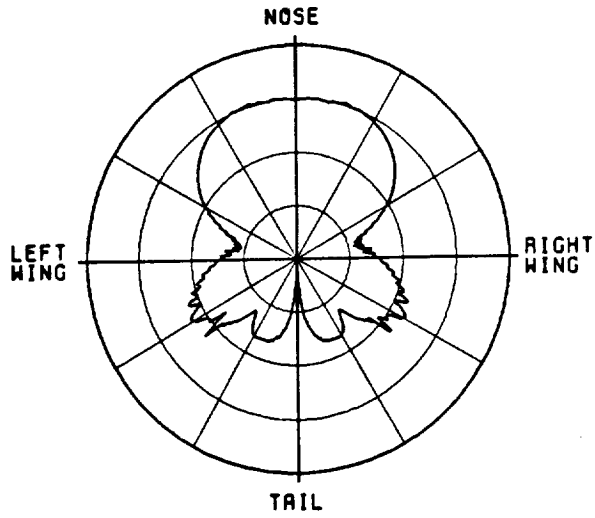

a) Σ beam

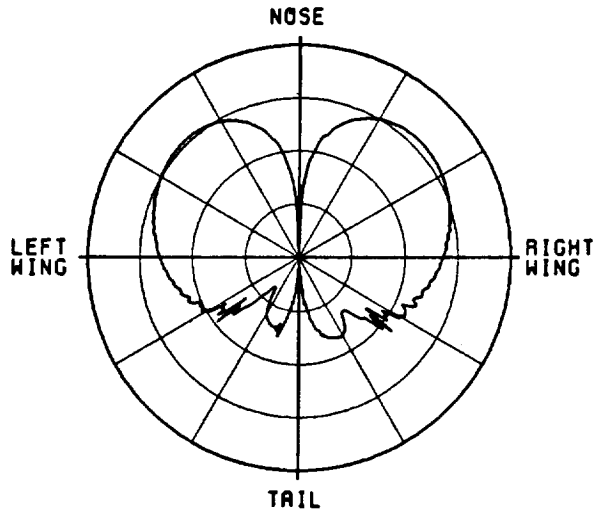

(SCALE: EACH DIVISION=10DB)

b) Δ beam

Figure 75. Azimuth pattern at an elevation angle 10° below the horizon for 0° azimuth beam position. Array at position D.

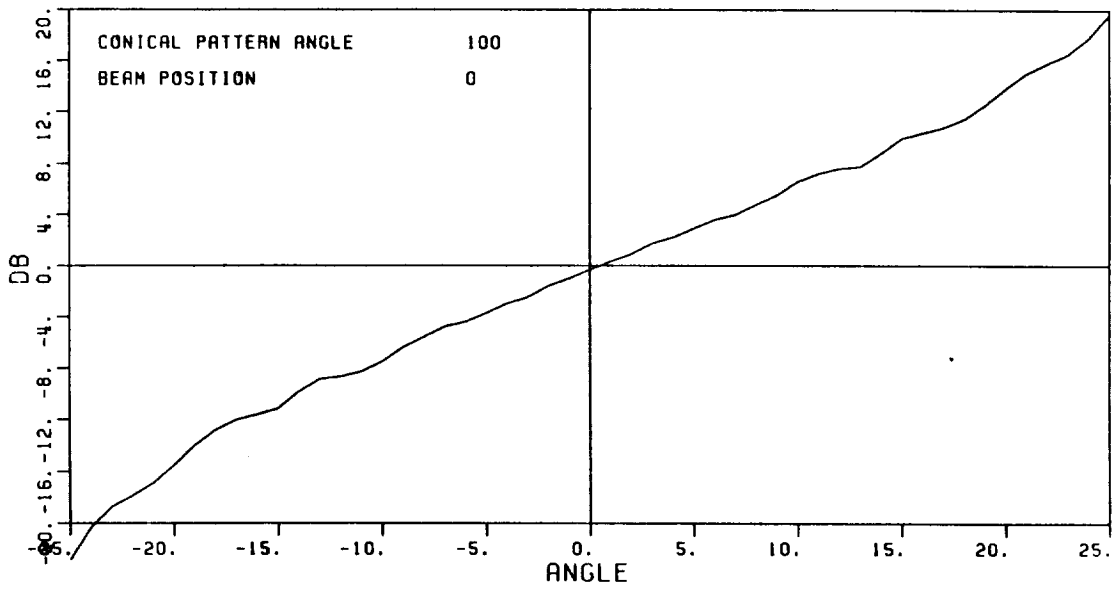

c) Corresponding monopulse characteristic

Figure 75. (Continued).

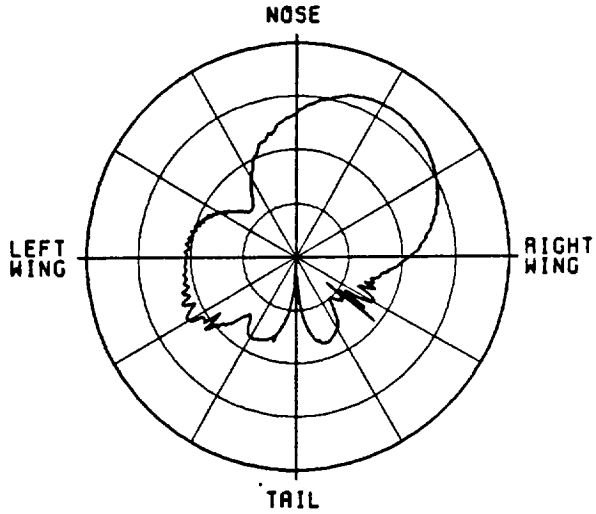

a) Σ beam

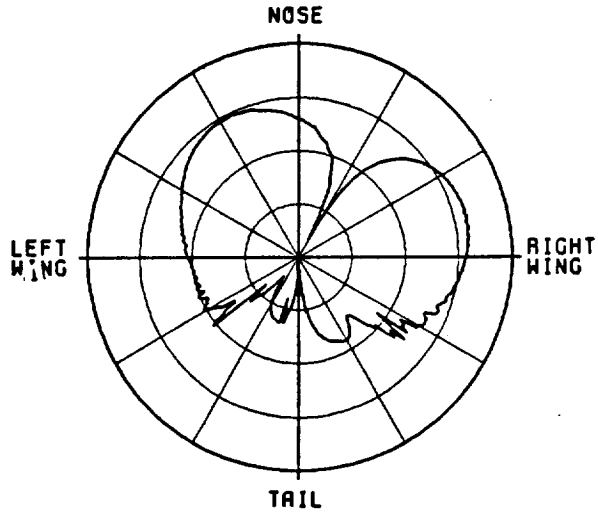

b) Δ beam

Figure 76. Azimuth pattern at an elevation angle 10° below the horizon for 30° azimuth beam position. Array at position D.

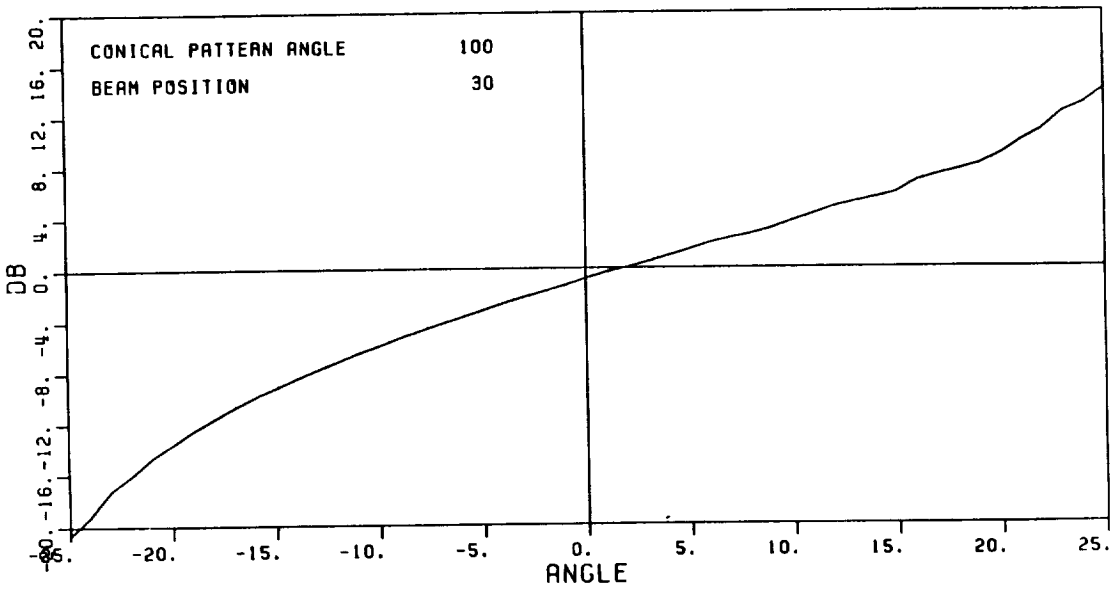

c) Corresponding monopulse characteristic

Figure 76. (Continued).

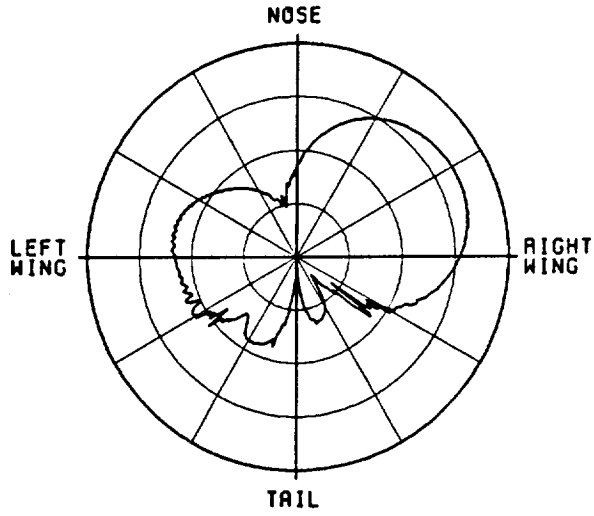

a) Σ beam

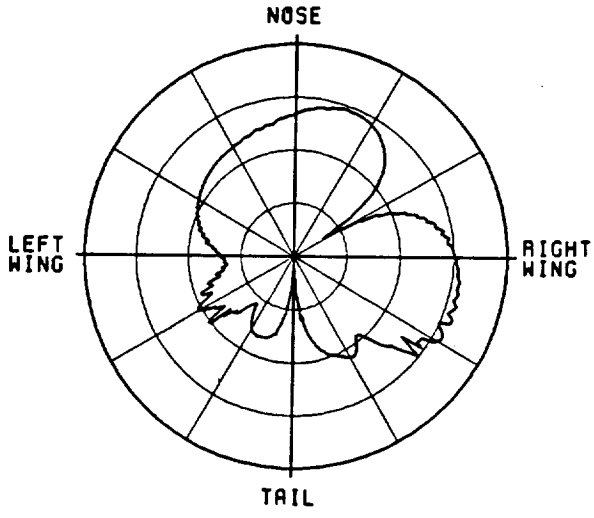

(SCALE: EACH DIVISION=10DB)

b) Δ beam

Figure 77. Azimuth pattern at an elevation angle 10° below the horizon for 60° azimuth beam position. Array at position D.

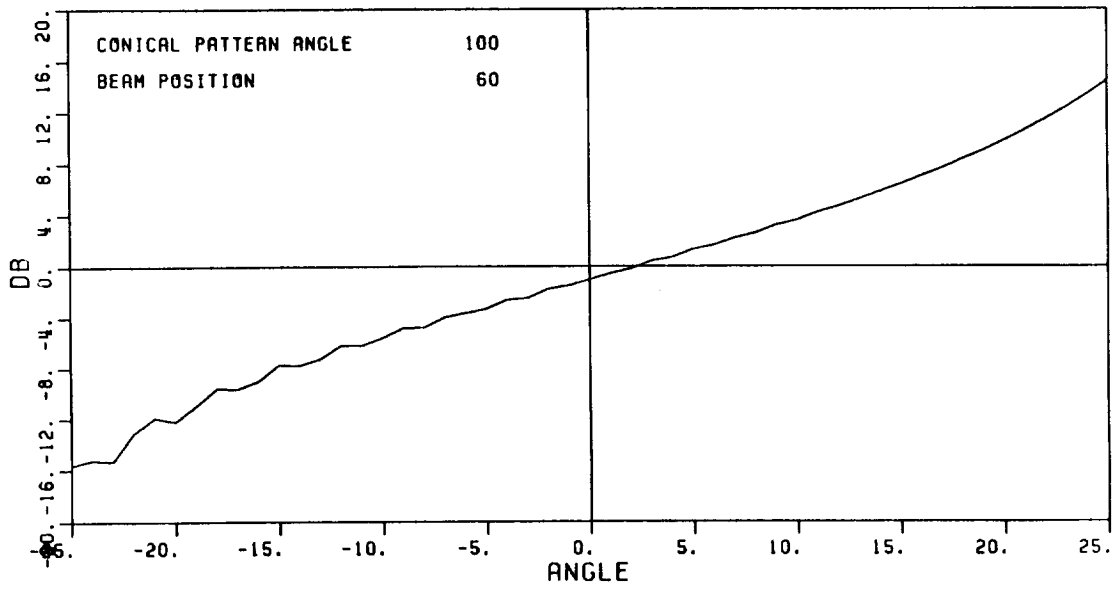

c) Corresponding monopulse characteristic

Figure 77. (Continued).

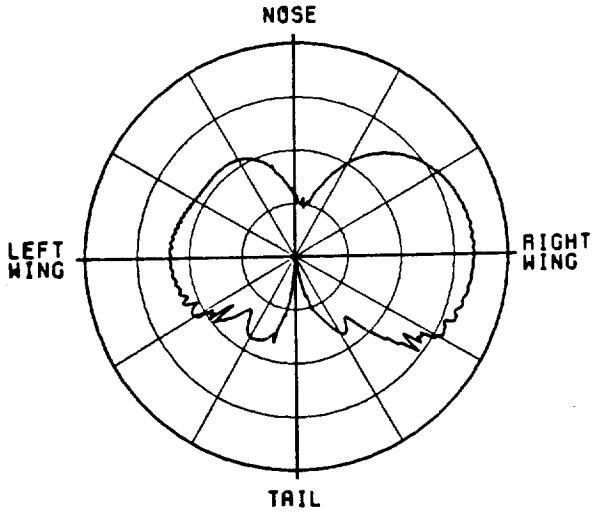

a) Σ beam

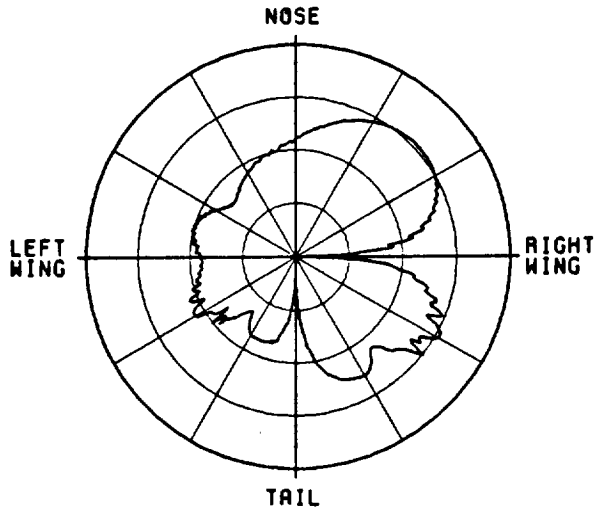

(SCALE: EACH DIVISION=10DB)

b) Δ beam

Figure 78. Azimuth pattern at an elevation angle 10° below the horizon for 90° azimuth beam position. Array at position D.

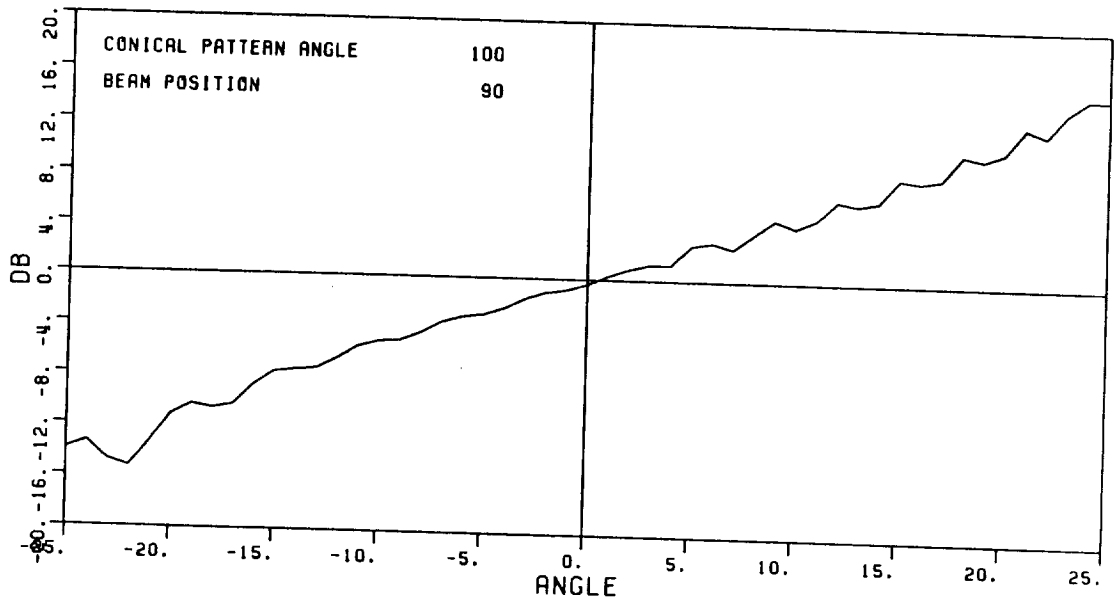

c) Corresponding monopulse characteristic

Figure 78. (Continued).

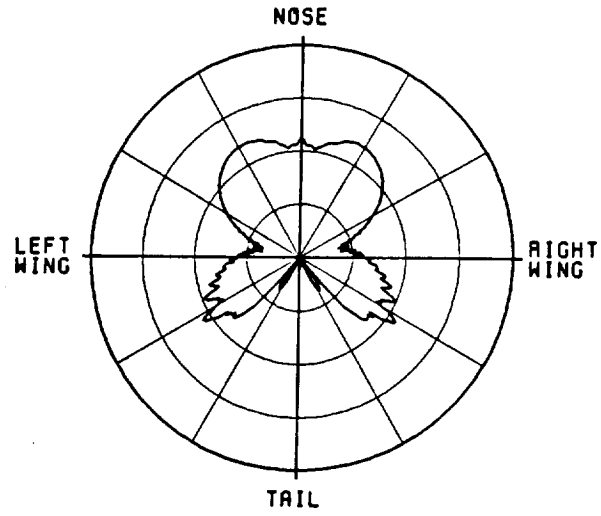

a) Σ beam

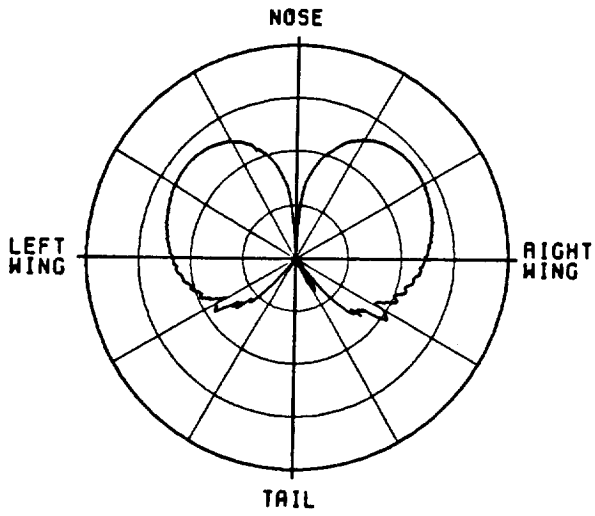

(SCALE: EACH DIVISION=10DB)

b) Δ beam

Figure 79. Azimuth pattern at an elevation angle 20° below the horizon for 0° azimuth beam position. Array at position D.

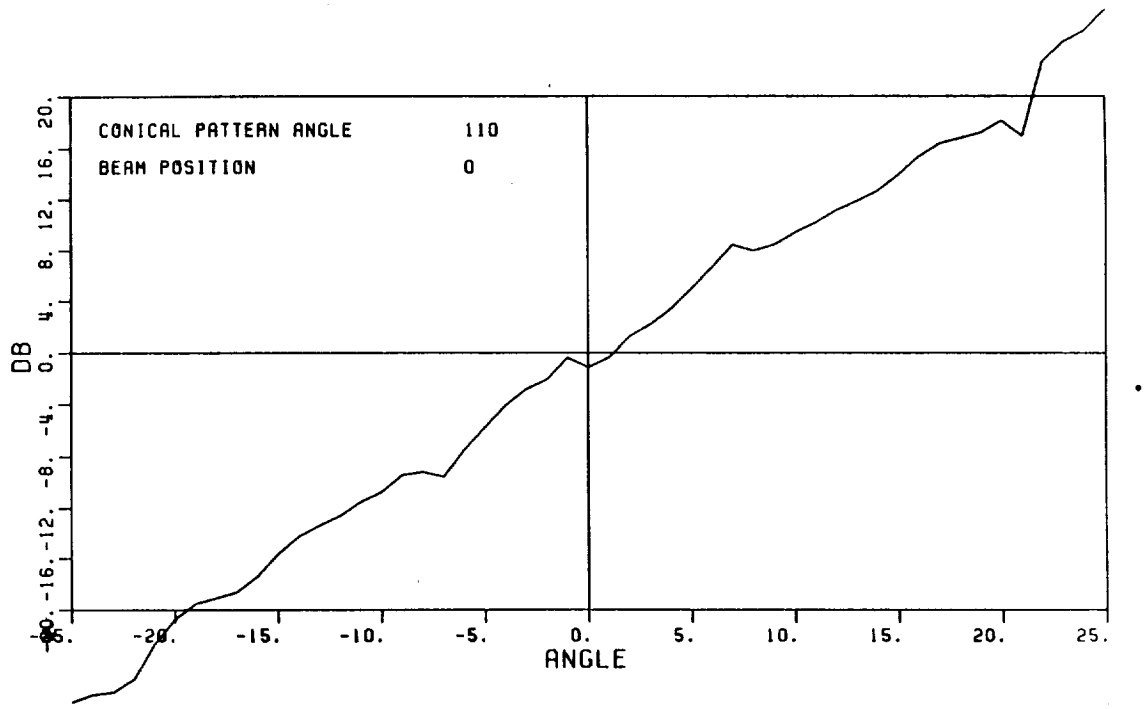

c) Corresponding monopulse characteristic

Figure 79. (Continued).

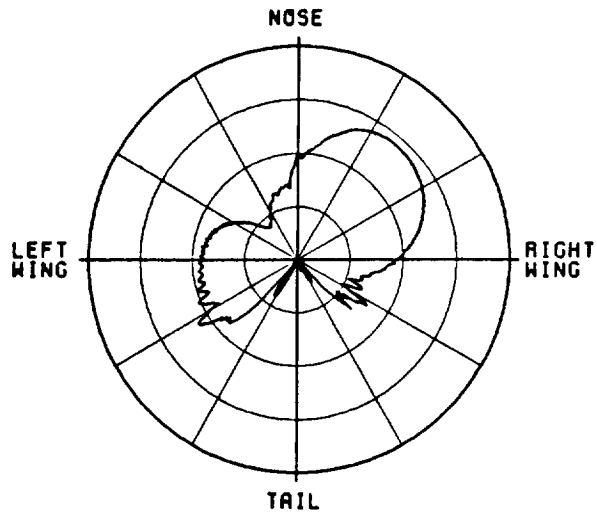

a) Σ beam

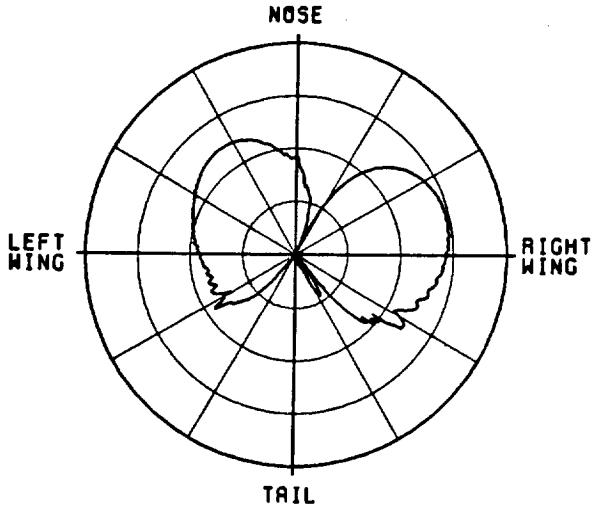

(SCALE: EACH DIVISION=10DB)

b) Δ beam

Figure 80. Azimuth pattern at an elevation angle 20° below the horizon for 30° azimuth beam position. Array at position D.

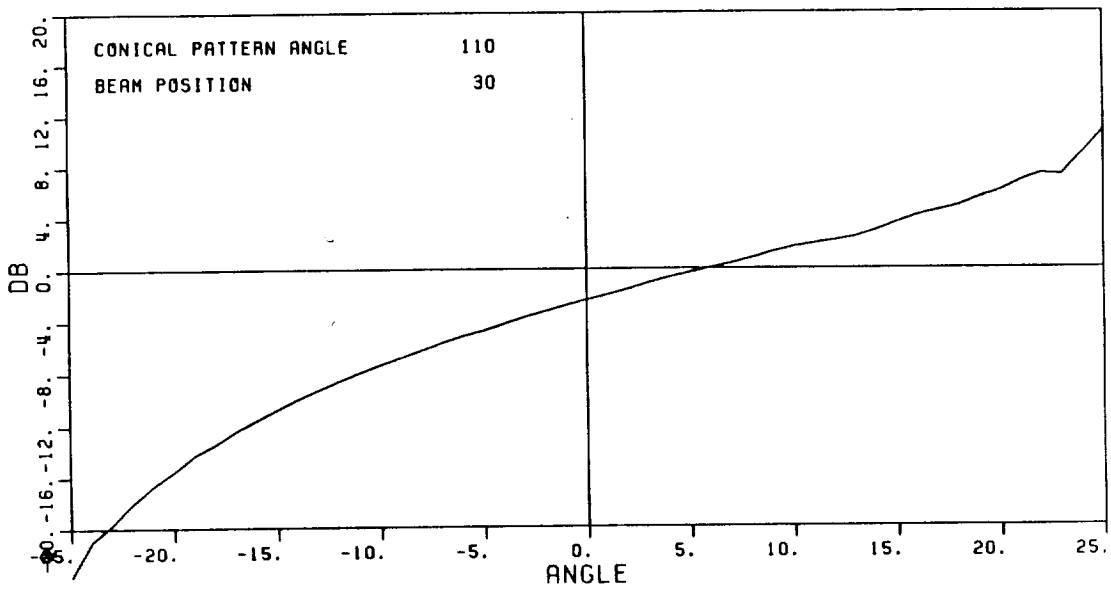

c) Corresponding monopulse characteristic

Figure 80. (Continued).

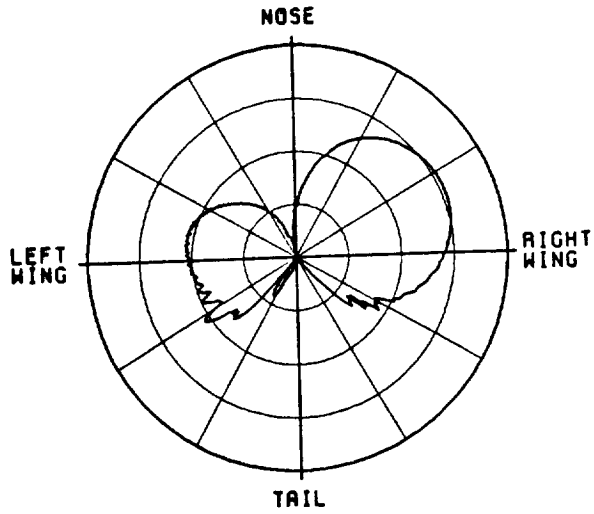

a) Σ beam

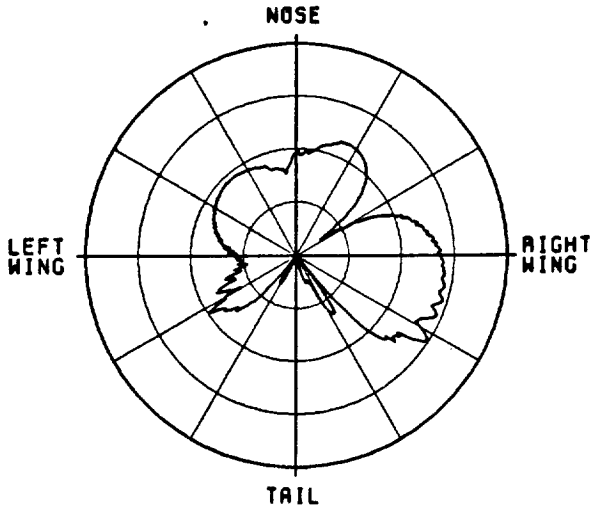

(SCALE: EACH DIVISION=10DB)

b) Δ beam

Figure 81. Azimuth pattern at an elevation angle 20° below the horizon for 60° azimuth beam position. Array at position D.

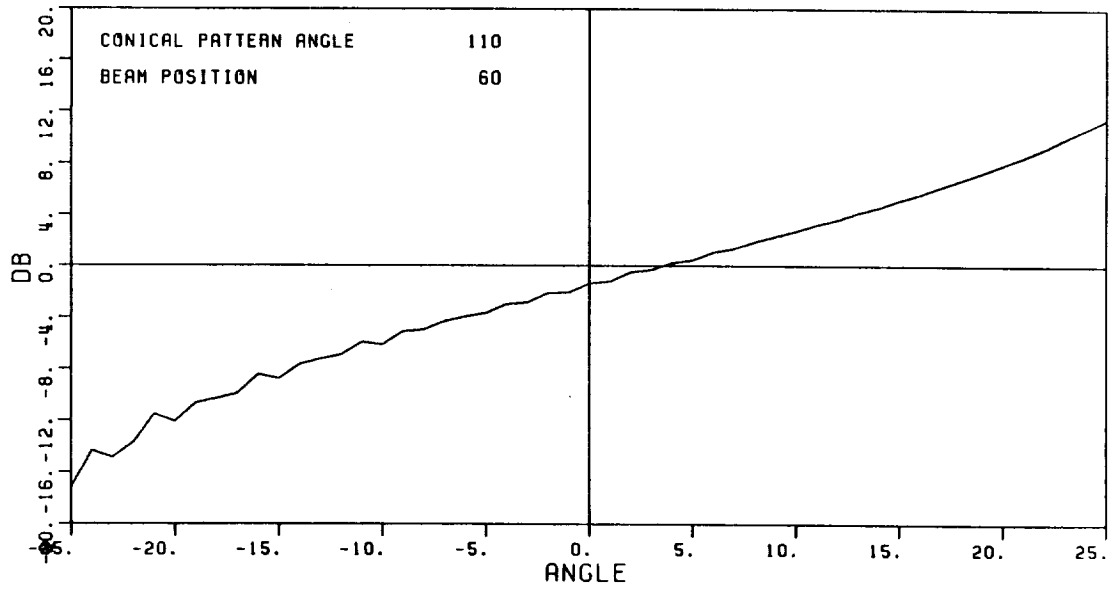

c) Corresponding monopulse characteristic

Figure 81. (Continued).

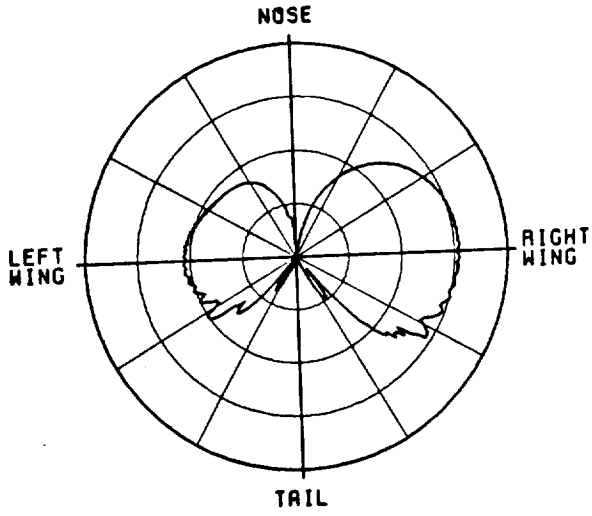

a) Σ beam

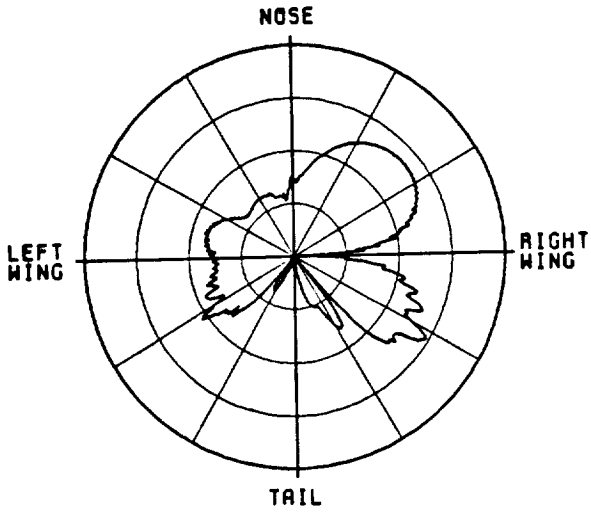

b) Δ beam

Figure 82. Azimuth pattern at an elevation angle 20° below the horizon for 90° azimuth beam position. Array at position D.

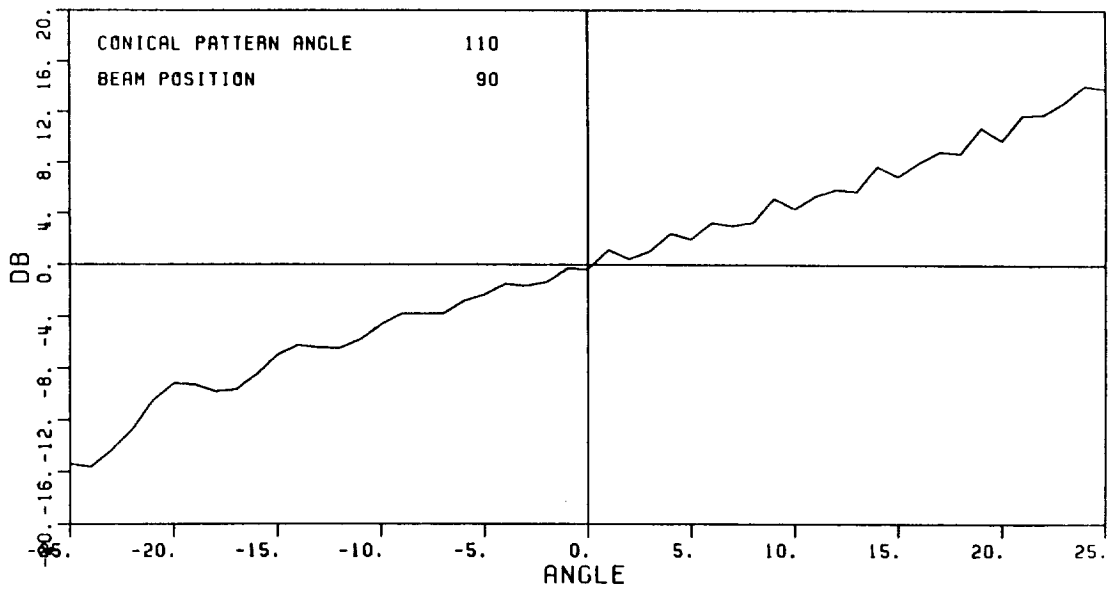

c) Corresponding monopulse characteristic

Figure 82. (Continued).

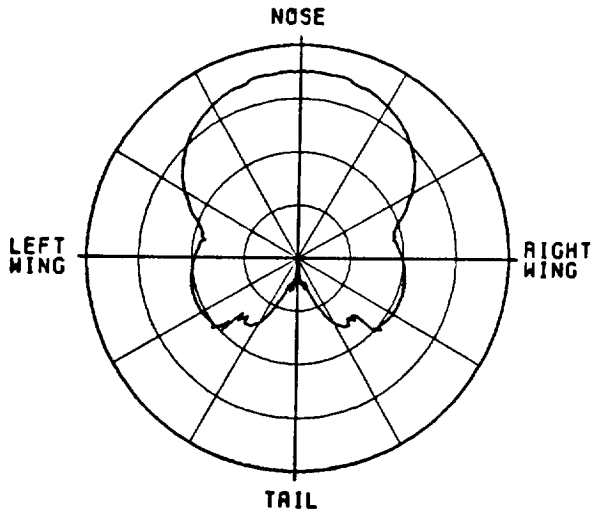

a) Σ beam

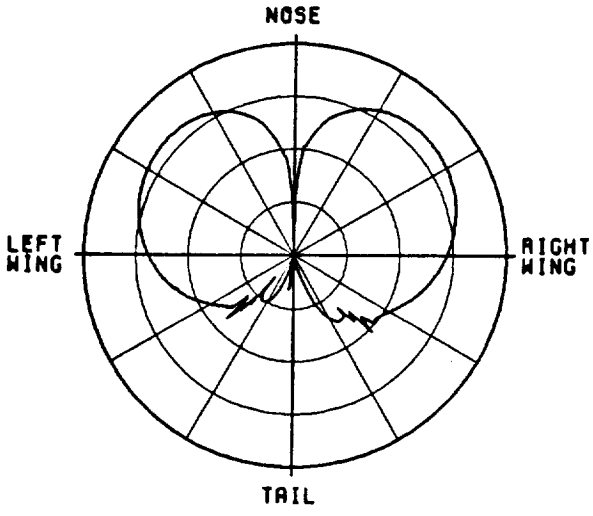

(SCALE: EACH DIVISION=10DB)

b) Δ beam

Figure 83. Azimuth pattern at an elevation angle 10° below the horizon for 0° azimuth beam position. Array at position E.

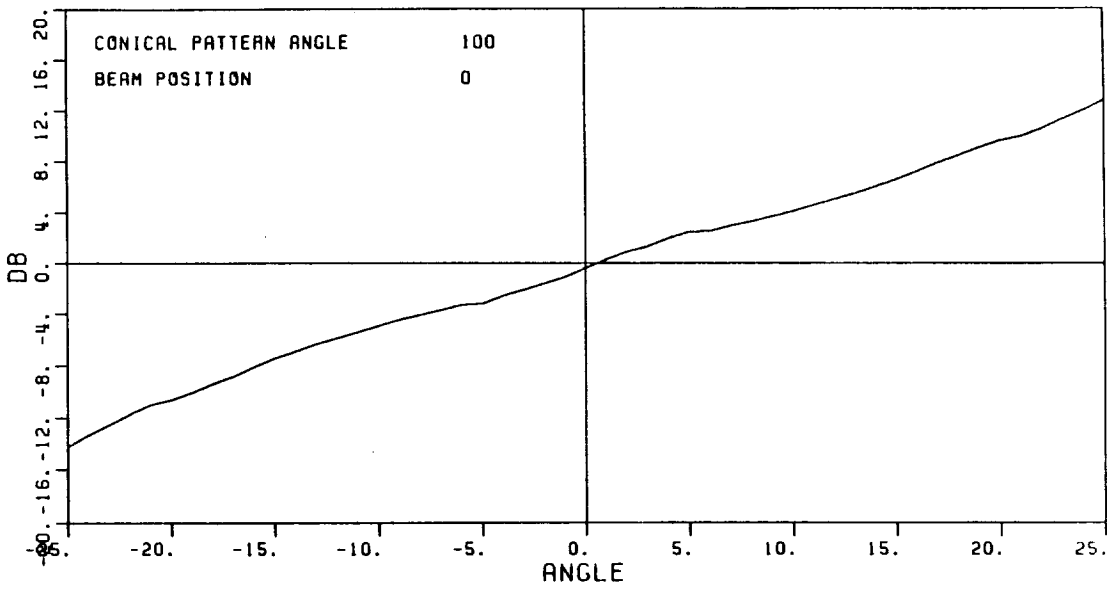

c) Corresponding monopulse characteristic

Figure 83. (Continued).

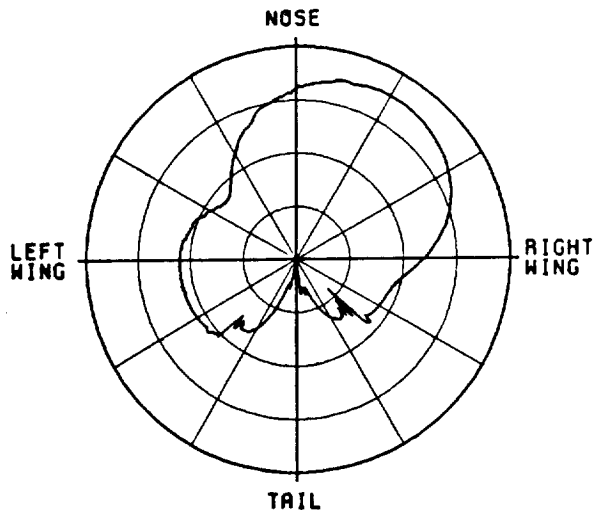

a) Σ beam

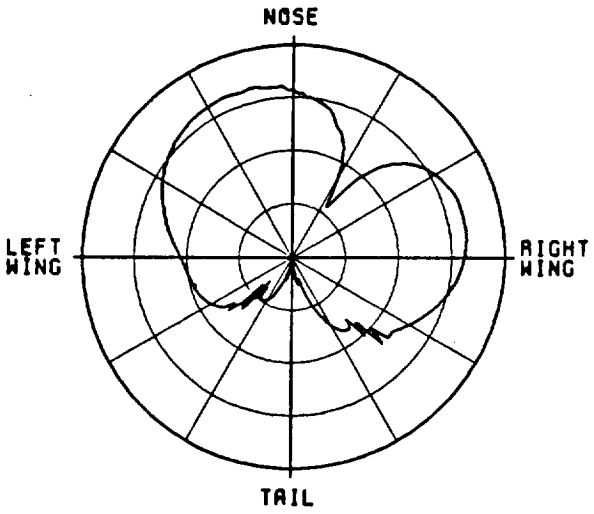

(SCALE: EACH DIVISION=10DB)

b) Δ beam

Figure 84. Azimuth pattern at an elevation angle 10° below the horizon for 30° azimuth beam position. Array at position E.

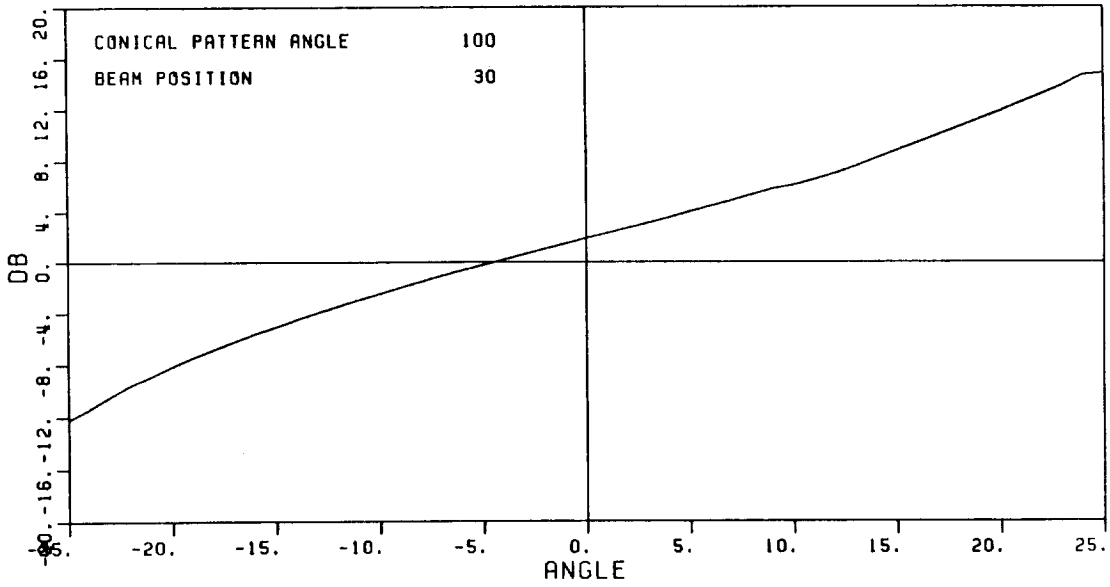

c) Corresponding monopulse characteristic

Figure 84. (Continued).

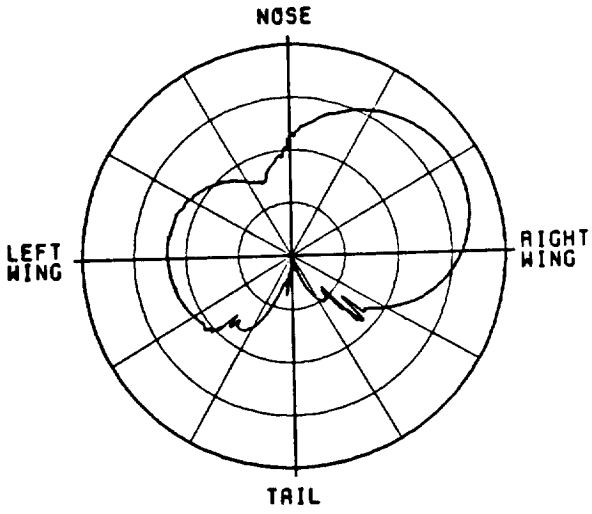

a) Σ beam

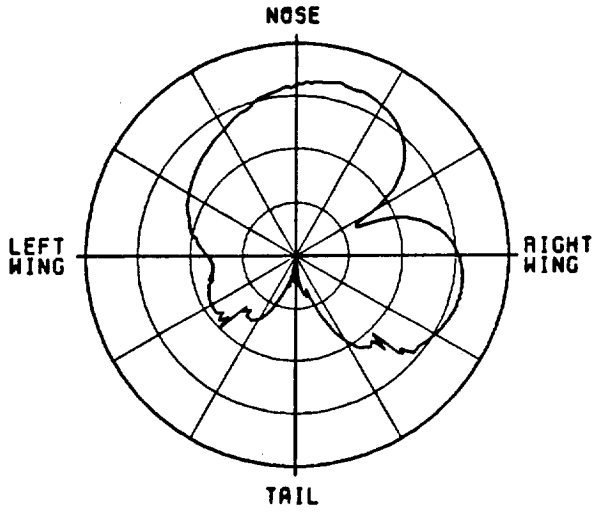

(SCALE: EACH DIVISION=10DB)

b) Δ beam

Figure 85. Azimuth pattern at an elevation angle 10° below the horizon for 60° azimuth beam position. Array at position E.

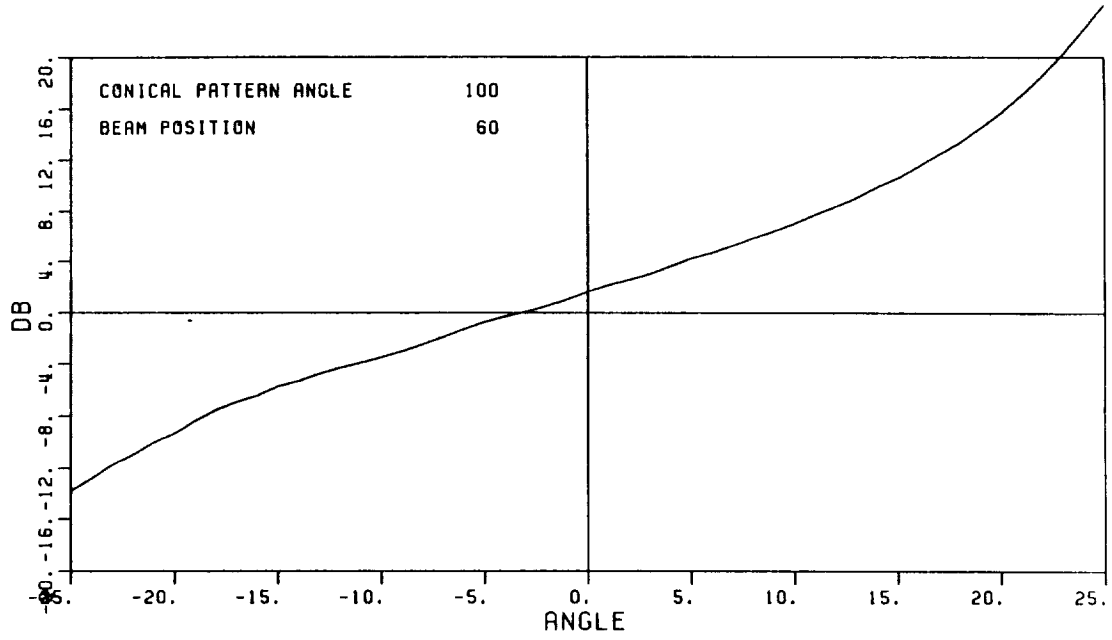

c) Corresponding monopulse characteristic

Figure 85. (Continued).

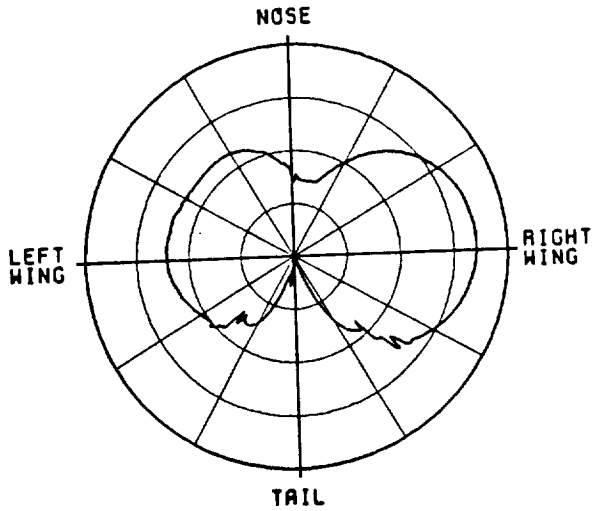

a) Σ beam

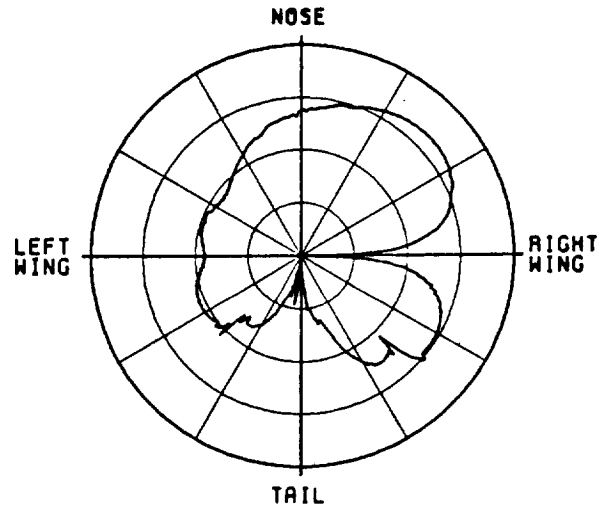

(SCALE: EACH DIVISION=10DB)

b) Δ beam

Figure 86. Azimuth pattern at an elevation angle 10° below the horizon for 90° azimuth beam position. Array at position E.

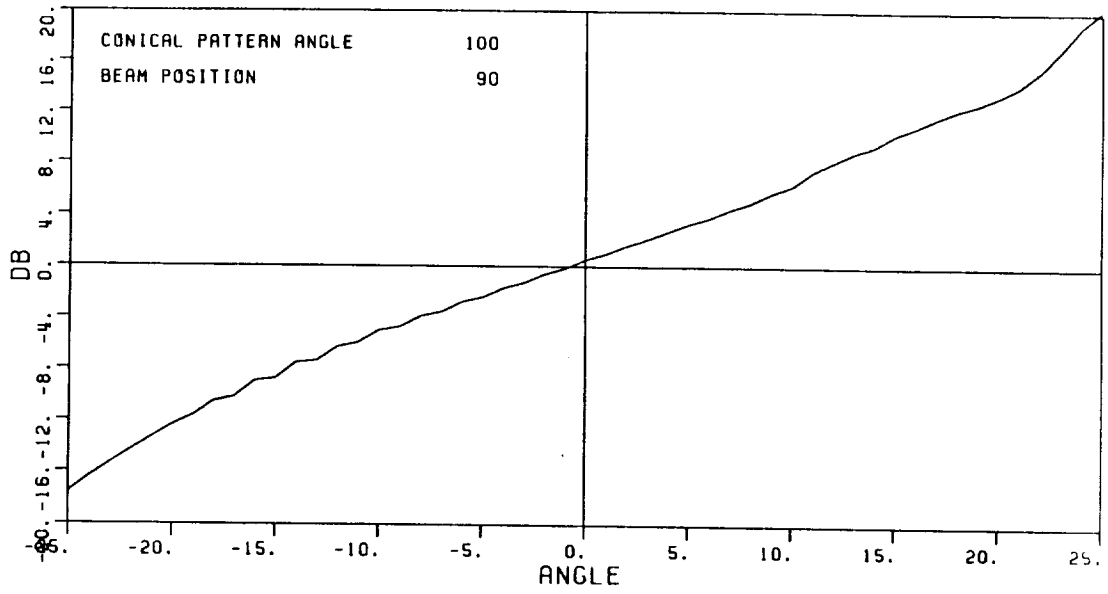

c) Corresponding monopulse characteristic

Figure 86. (Continued).

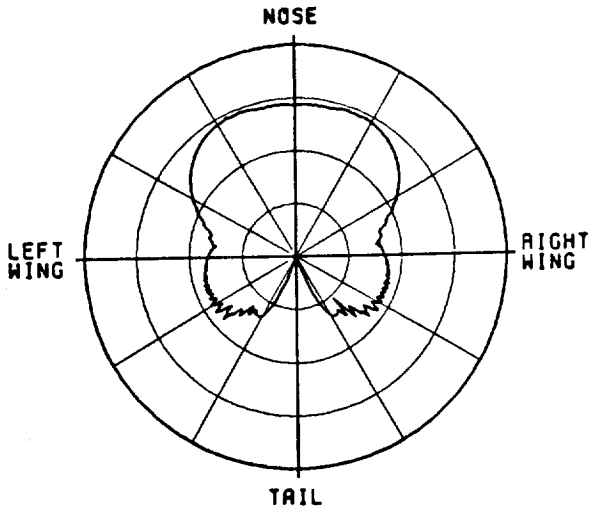

a) Σ beam

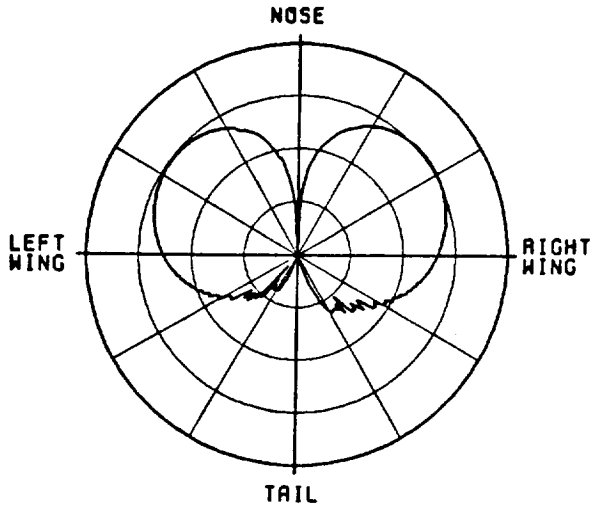

(SCALE: EACH DIVISION=10DB)

b) Δ beam

Figure 87. Azimuth pattern at an elevation angle 20° below the horizon for 0° azimuth beam position. Array at position E.

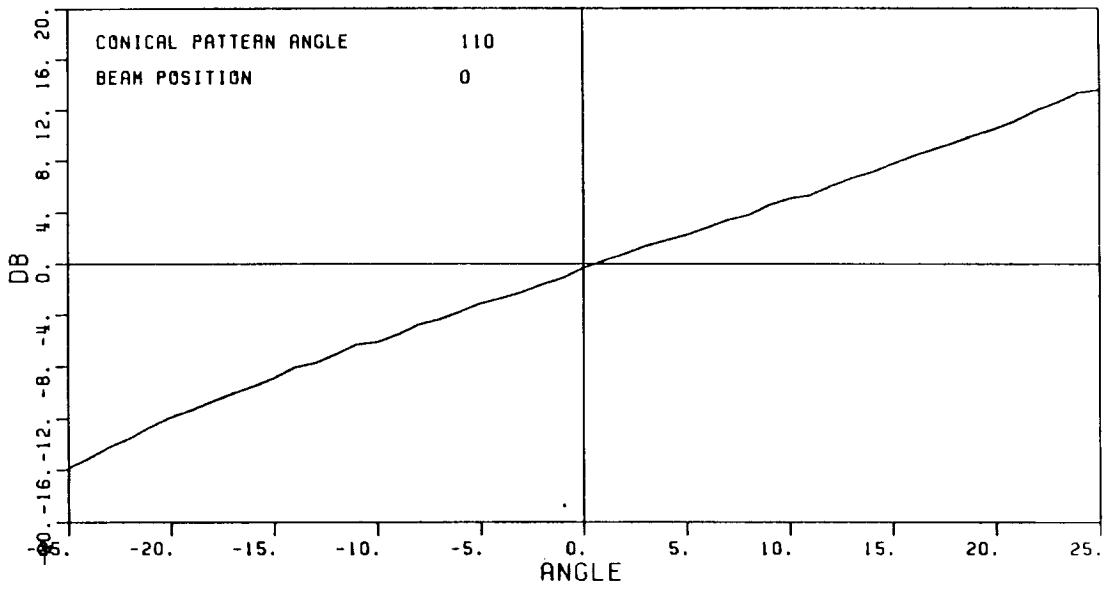

c) Corresponding monopulse characteristic

Figure 87. (Continued).

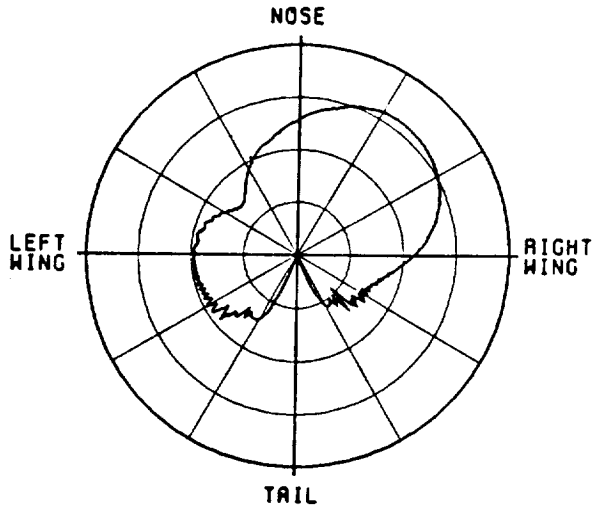

a) Σ beam

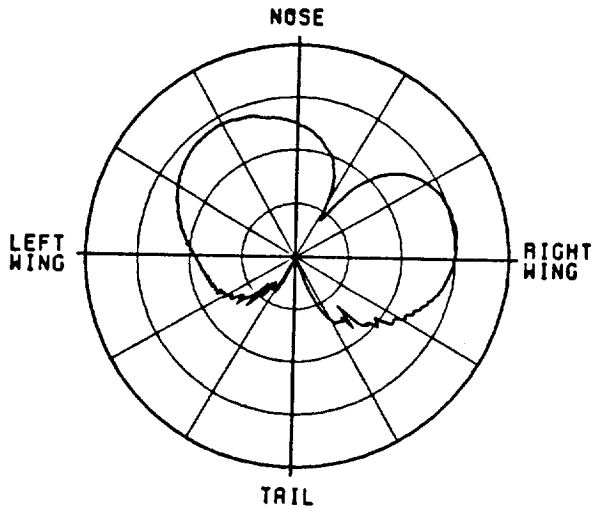

(SCALE: EACH DIVISION=10DB)

b) Δ beam

Figure 88. Azimuth pattern at an elevation angle 20° below the horizon for 30° azimuth beam position. Array at position E.

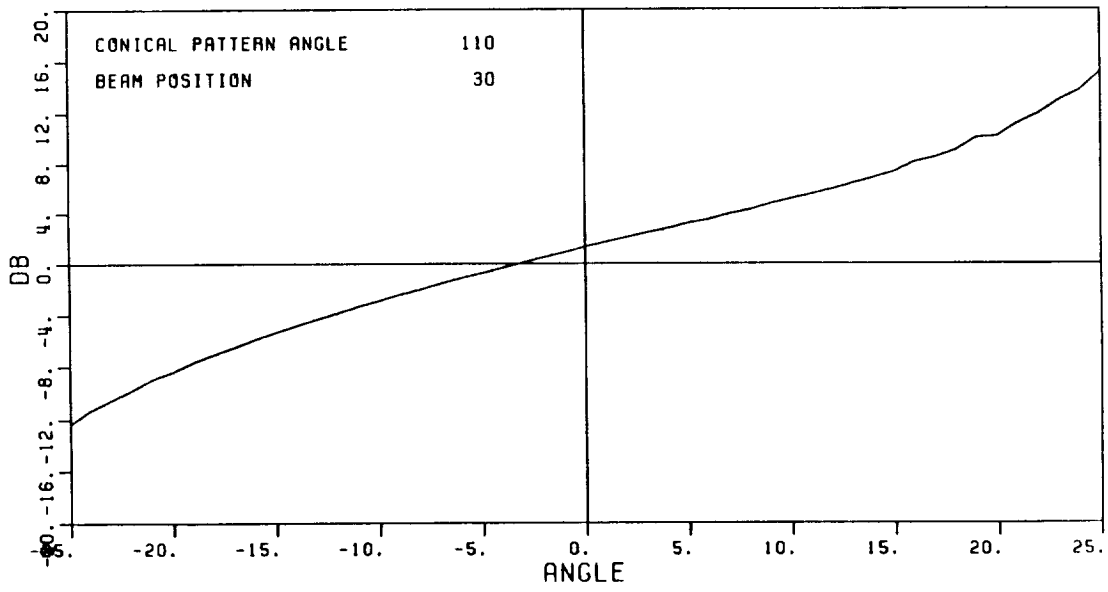

c) Corresponding monopulse characteristic

Figure 88. (Continued).

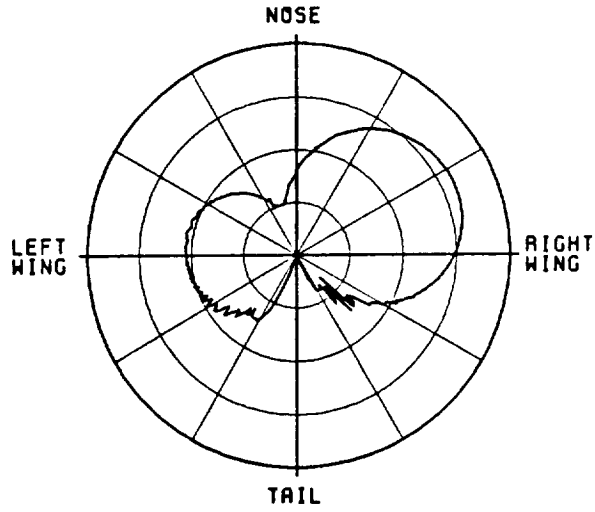

a) Σ beam

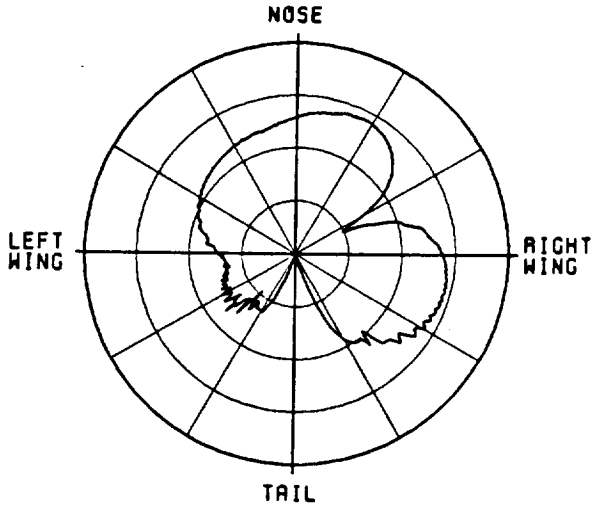

b) Δ beam

Figure 89. Azimuth pattern at an elevation angle 20° below the horizon for 60° azimuth beam position. Array at position E.

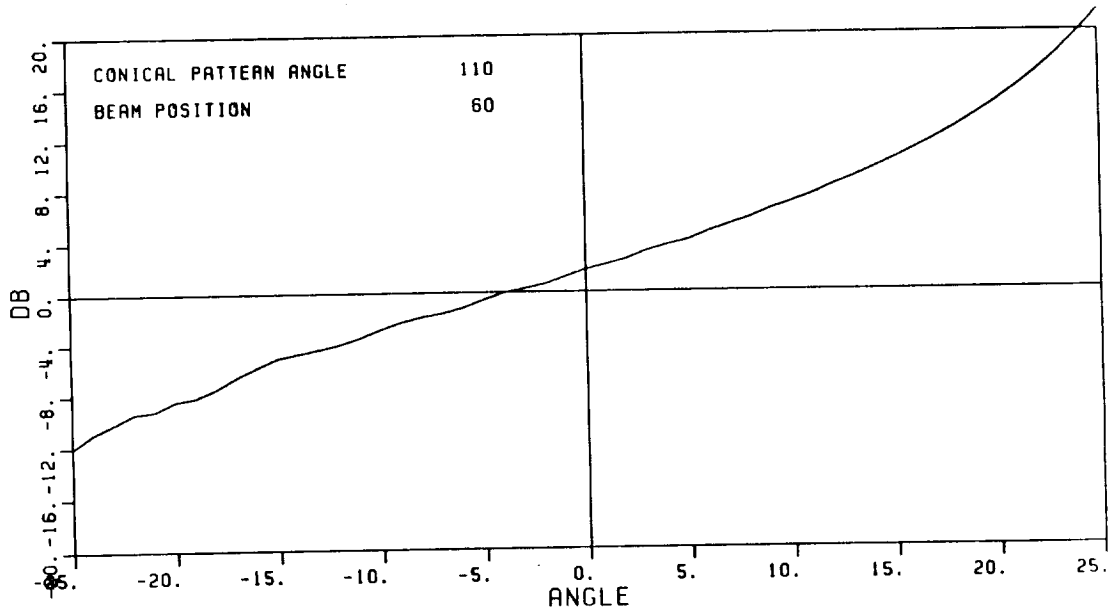

c) Corresponding monopulse characteristic

Figure 89. (Continued).

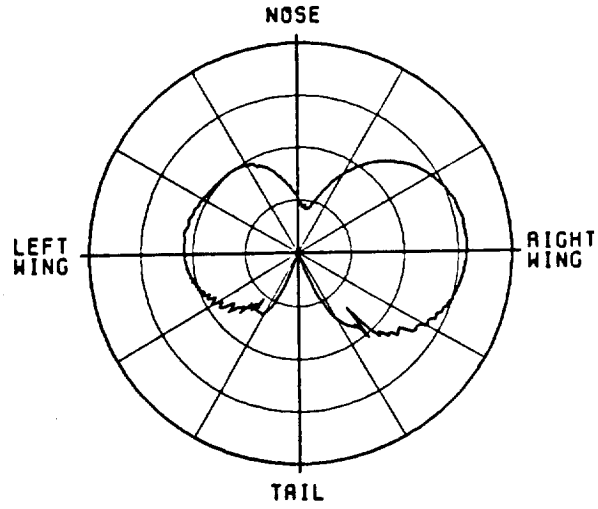

a) Σ beam

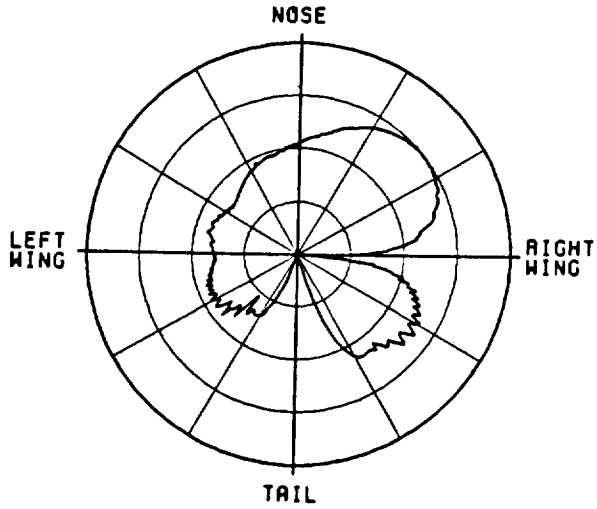

(SCALE: EACH DIVISION=10DB)

b) Δ beam

Figure 90. Azimuth pattern at an elevation angle 20° below the horizon for 90° azimuth beam position. Array at position E.

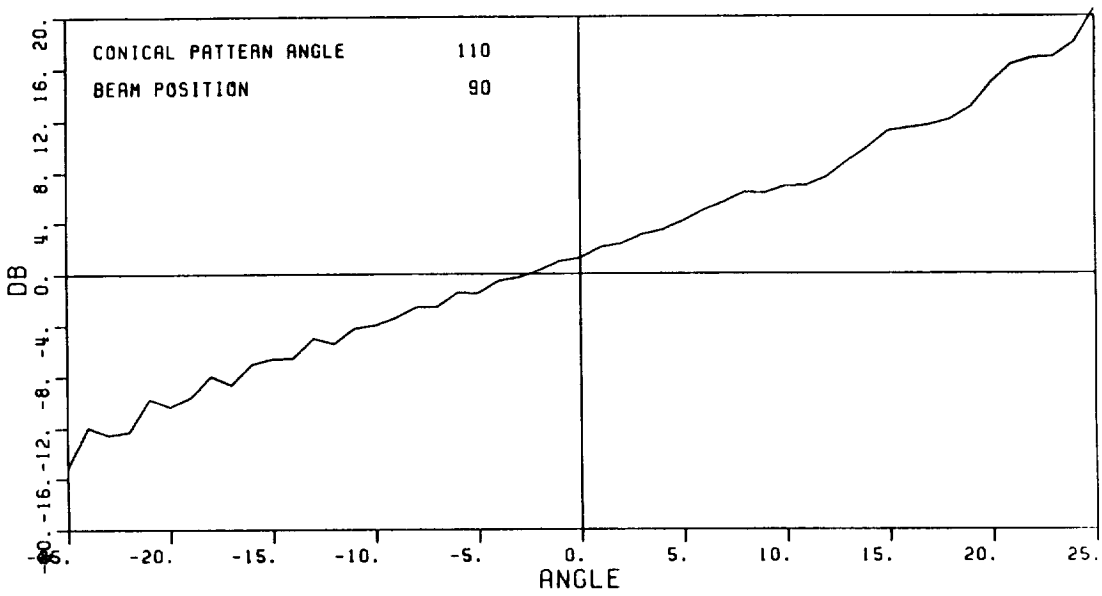

c) Corresponding monopulse characteristic

Figure 90. (Continued).

VI. SUMMARY AND CONCLUSIONS

Although reflection and diffraction from both the wings and vertical stabilizer have a detrimental effect on the Σ and Δ beam field patterns of the TCAS II antenna system, it is obvious that diffraction from the vertical stabilizer causes the most serious problem.This scattering is most serious when the beams are directed toward or near the tail of the aircraft. The best way to combat this seems to be to mount the TCAS II array as far from the vertical stabilizer as possible.

At present the TCAS II system compares the output of the receiver with a look up table in order to determine the azimuth angle of an approaching aircraft in order to signal a potential collision. Although a look up table has been produced for each of the 64 separate beam positions, no provision has been made to address the fact that for each beam position the monopulse characteristic will be different due to the change in the Σ and Δ beams according to the elevation angle of the target. This is especially important when the beams are directed toward the tail of the aircraft due to the dramatic difference in the Σ and Δ beams depending on whether the elevation angle of the target is above or below the top of the vertical stabilizer. The best way to overcome this problem is to locate the the array near the nose of the aircraft as indicated earlier.

An added benefit from mounting the array close to the nose of the aircraft is that the effects of fuselage blockage, for elevation angles below the horizon, are significantly reduced in the forward direction.

REFERENCES

[1] W.D. Burnside, J.J. Kim and B. Grandchamp, "Airborne Antenna Radiation Pattern Code User's Manual", to be published.

[2] J.J. Kim, "Simulation and Analysis of Airborne Antenna Radiation Patterns", Ph.D. Dissertation, The Ohio State University, Department of Electrical Engineering, 1984.

[3] A.I. Sinsky, J.E. Reed and J. Fee, "Enhanced TCAS II Tracking Accuracy", AIAA/IEEE Digital Avionics Systems Conference Paper 84-2738-CP, 1984.

[4] A.I. Sinsky and J. Acoraci, "Technical Notes on TCAS II", unpublished correspondence with The Ohio State University ElectroScience Laboratory, 1985.

[5] A.I. Sinsky, "Circular Array Design Equations", Allied Bendix Aerospace, Bendix Communications Div., Technical Report BCD-TN-85-001, 1985.

APPENDIX A

AIRCRAFT CODE INPUT DATA FOR THE TCAS II ANTENNA MOUNTED ON A BOEING 737

```
UN:INCHES
3
FQ: 1.06 GHZ
1,1.06,1.
FG: BOEING 737
77.,74.,830.,308.56
T
0.,0.,70.
SG: ELEMENT 1
2.64,66.464
2
1.39,-45.
0.,0.,0.,2.78,3
1.,-45.
1.39,135.
0.,0.,0.,2.78,3
.698,45.
PG: RIGHT WING
4,T
1.,75.,67.952
1.,536.93,316.14
1.,536.93,379.86
1.,75.,240.26
PG: LEFT WING
4,T
1.,-75.,240.26
1.,-536.93,379.86
1.,-536.93,316.14
1.,-75.,67.952
PG: TAIL
4,T
77.,8.25,618.55
284.147,8.25,819.056
284.147,0.,683.696
77.,0.,483.19
PG: TAIL
4,T
77.,0.,483.19
284.147,0.,683.696
284.147,-8.25,819.056
77.,-8.25,618.55
PP: POLAR PLOT IN DB
T
1,1.5,3
PD: AZIMUTH PLANE
90.,0.,90.
0,360,1
T,1000000.
EX:
SG: ELEMENT 2
3.73,70.
2
1.39,0.
0.,0.,0.,2.78,3
1.,-45.
1.39,180.
0.,0.,0.,2.78,3
.698,45.
EX:
SG: ELEMENT 3
2.64,73.536
2
1.39,45.
0.,0.,0.,2.78,3
1.,-45.
1.39,225.
0.,0.,0.,2.78,3
.698,45.
EX:
SG: ELEMENT 4
0.,75.
2
1.39,90.
0.,0.,0.,2.78,3
1.,-45.
1.39,270.
0.,0.,0.,2.78,3
.698,45.
EX:
SG: ELEMENT 5
-2.64,73.536
2
1.39,135.
0.,0.,0.,2.78,3
1.,-45.
1.39,-45.
0.,0.,0.,2.78,3
.698,45.
EX:
SG: ELEMENT 6
-3.73,70.
2
1.39,180.
0.,0.,0.,2.78,3
1.,-45.
1.39,0.
0.,0.,0.,2.78,3
.698,45.
```

```
EX:
SG: ELEMENT 7
-2.64,66.464
2
1.39,225.
0.,0.,0.,2.78,3
1.,-45.
1.39,45.
0.,0.,0.,2.78,3
.698,45.
EX:
SG: ELEMENT 8
0.,65.
2
1.39,270.
0.,0.,0.,2.78,3
1.,-45.
1.39,90.
0.,0.,0.,2.78,3
.698,45.
EX:
```

APPENDIX B

AIRCRAFT CODE INPUT DATA
FOR TWO PLATES
SIMULATING THE BOEING 737 NOSE SECTION

```
PG: NOSE
4.T
5.5.-10.,-308.56
-.1,-10.,-321.6
-.1,0.,-321.6
5.5.0.,-308.56
PG: NOSE
4.T
5.5.0.,-308.6
-.1,0.,-321.6
-.1,10.,-321.6
5.5.10.,-308.56
```